PIV APPLICATIONS IN VORTEX RINGS AND OSCILLATORY BOUNDARY LAYERS

by

Anna Mujal-Colilles

Supervised by:

Prof. Dr. Allen Bateman Pinzón

GRUP D'INVESTIGACIÓ EN MODELITZACIÓ DE CONQUES I TRANSPORT DE SEDIMENTS

UNIVERSITAT POLITÈCNICA DE CATALUNYA

Barcelona

March 2013

Funded by:

Als meus pares

Abstract

Particle Image Velocimetry (PIV) is one of the most used experimental techniques in fluid mechanics to obtain the velocity field of a flow. One of its most celebrated characteristics is that it does not have interference on the phenomenon of study which makes it suitable to describe qualitatively and quantitatively many phenomena either micro or macroscopic.

This thesis presents the PIV technique applied to two different fluid mechanic problems: vortex rings impinging permeable boundaries and oscillatory boundary layers in the laminar-to-turbulent regime.

The first part of this thesis focuses on the impingement of vortex rings towards permeable boundaries and compares the results with the interaction of a vortex ring with a solid boundary. Assuming that a vortex ring is an axisymmetric structure, 2D PIV experiments are performed over boundaries on 4 different permeabilities and a solid boundary. When a vortex approaches a solid boundary, three different phenomena are clearly visible: the vortex ring decelerates when the distance between the core and the wall is in the order of the initial diameter of the ring. At the same time, the diameter starts increasing producing a stretching effect and, finally, secondary vorticity appears after the ring has reached the minimum distance from the wall. Experimental results lead to some interesting conclusions when the permeability of the boundary increases: the deceleration of the vortex ring starts later, the diameter does not increase as much and, finally, secondary vorticity is weaker and has shorter life.

The second and third part of this thesis, focus on the study of oscillatory boundary layers over smooth and rough walls. Experimental measurements were conducted over smooth and two different rough beds for $Re_w = 0.4 \cdot 10^4 \sim 2 \cdot 10^4$ spanning the laminar, transitional and turbulent flow regimes. A multi-camera 2D-PIV system was used in an experimental oscillatory-flow tunnel. Characteristic variables like boundary layer thickness and friction factor were computed using different methods. Results obtained experimentally in smooth wall experiments are consistent with theoretical work. For the rough wall cases different formulations have been compared. Finally, results show how the phase lead between wall velocity and free-stream velocity is better defined when the integral of momentum equation is used to estimate the friction velocity, instead of the sum of viscous and Reynolds stresses. The observed differences in maximum friction velocity and phase lag between friction and free-stream velocities are highly sensitive to the zero level definition. Regardless of the flow regime, boundary-layer thickness reached its maximum value at a phase near the flow reversal.

Finally, a detailed analysis of the structures present in such oscillatory boundary layers yield to a description of four different features: vortex tubes present in oscillatory flows over smooth beds, and vortices, turbulent spots and shear layers present in oscillatory flows over rough beds. The inception of vortex tubes is consistent with the state-of-art predictors as a result of the Kelvin-Helmholtz instability. Experiments described in this thesis confirm these characteristics and can detect the existence of the vortex tubes during a longer period of time. Furthermore, structures present in rough wall experiments are a little bit more complicated because their inception and evolution are clearly influenced by the position of the sediment grains forming the bed. Vortices are created behind a kink in the bed sediment profile during the wall flow reversal and are shed from the wall when flow starts its acceleration cycle. Both the vertical and horizontal evolutions of the vortex position depend on the ratio between the amplitude of oscillation and roughness of the sediment bed. Turbulent spots are defined as structures which are born vortices but lose their shape in an early stage. In fact, turbulent spots are small vortices appearing one close to the other in the instantaneous field which show up as non-shape structures on the phase-averaged velocity field. They follow the same trajectories as vortices but reach lower heights before dissipating. Finally, shear layers were only detected in the larger bed roughness and are described as a sum of vortices that are shed consecutively from the same sediment. These shear layers are linked to vortices during the wall flow reversal when a big vortex is formed in the same place as the shear layer.

The work presented in this thesis is based in two fluid mechanics problems. The PIV technique has been proved to be a suitable tool for these studies.

Resum

La tècnica experimental del Particle Image Velocimetry (PIV) és una de les més utilitzades en el món de la mecànica de fluids per obtenir el camp de velocitats en un flux. La seva no interferència en el desenvolupament del fenomen que s'estudia la fa aplicable a tot tipus de fenòmens, ja sigui micro com macroscòpics i permet estudiar qualitativa i quantitativament la dinàmica de fluids d'un fenomen particular.

Aquesta tesis presenta l'aplicació del PIV a dos problemes de mecànica de fluids diferents: anells de vorticitat impactant contorns permeables i capes límit oscil·latòries dins del règim transitori.

La primera part d'aquesta tesis es centra en l'estudi dels anells de vorticitat impactant contorns permeables i la seva comparació amb l'impacte del mateix anell amb una paret sòlida. Assumint que un anell de vorticitat és una estructura axisimètrica, s'han realitzat experiments PIV en 2D, en quatre contorns permeables diferents i un contorn sòlid. Quan un anell de vorticitat es mou cap a una superfície sòlida es fan presents tres fenòmens principals: la desacceleració de l'anell de vorticitat quan assoleix una distància amb la paret de l'ordre del diàmetre inicial de l'anell. Al mateix temps un augment del diàmetre produint un efecte estirament i finalment l'aparició d'un segon anell de vorticitat quan el primer anell ha assolit la distància mínima de la paret. El treball experimental aporta algunes conclusions interessants sobre l'evolució d'aquestes característiques principals a mesura que la permeabilitat del contorn d'impacte augmenta: la distància de la paret a la qual comença la desacceleració disminueix, el diàmetre de l'anell de vorticitat primari creix amb menys intensitat i finalment el segon anell de vorticitat és més dèbil i té una vida més curta.

La segona i tercera part de la tesis es centren en descriure el fenomen de capa límit oscil·latòria en fluxos sobre llits llisos i rugosos. En aquesta tesis es descriuen els experiments centrats en l'estudi de la capa límit oscil·latòria sobre fons llis i dos tipus diferents de fons rugós per a un rang de $Re_w = 0.4 \cdot 10^4 \sim 2 \cdot 10^4$; els experiments es centren en la transició de règim laminar a règim laminar a turbulent i utilitzen la tècnica de 2D PIV amb multicàmera aplicada a un túnel de flux oscil·latori. Algunes variables característiques com el gruix de la capa límit o el factor de fricció s'analitzen des de diferents perspectives. Els resultats obtinguts en els experiments de llit rugós coincideixen amb les prediccions realitzades per a teoria existent. Per als experiments en llit rugós diferents formulacions es comparen. Finalment els resultats mostren com la diferència de fase entre la velocitat de paret i a la velocitat del pistó que activa

l'oscil·lació es defineix més bé quan es calcula a través de la integral de la quantitat de moviment. Les diferències observades amb els resultats obtinguts quan es calcula a través de la suma de tensions de Reynolds i tensions viscoses són degudes principalment a la sensibilitat d'ambdues equacions a la definició del zero d'ordenades. Per altra banda, el gruix màxim observat per la capa límit es produeix just abans de que es produeixi l'instant de velocitat zero, també anomenat fase del revers, independentment del règim del flux.

Finalment es realitza un anàlisi detallat de les estructures presents en les capes límit oscil·latòries definint fins a quatre tipus diferents: tubs de vorticitat presents en fluxos oscil·latoris sobre llits llisos, vòrtexs, bursts i capes de tensió detectades en els fluxos sobre llits rugosos. L'evolució dels tubs de vorticitat coincideix amb la teoria ja publicada i són el resultat de l'aparició de la inestabilitat de Kelvin-Helmholtz. Els experiments descrits en aquesta tesis confirmen les mateixes característiques i permeten definir la vida d'aquests tubs de vorticitat. Les estructures presents en llits rugosos són una mica més complicades degut a que la seva formació i evolució està clarament influenciada per la posició dels grans de sediment que formen el fons. Els vòrtexs es creen darrere una punta en el perfil del llit de sediment durant la fase del revers prop de la paret i es separen d'aquesta quan comença el cicle d'acceleració. L'evolució tant de la posició vertical com horitzontal d'aquests vòrtexs depenen del quocient entre l'amplitud de l'oscil·lació i la rugositat del sediment. Els bursts es defineixen com a aquelles estructures que neixen sent un vòrtex però perden la forma de seguida. De fet, aquests bursts són vòrtexs de mida més petita i que apareixen en localitzacions properes en el camp de velocitats instantani. No obstant quan es realitza la mitjana en fase, la seva forma desapareix, mostrant-se com a bursts. La seva trajectòria és semblant a la dels vòrtexs prèviament descrits, però assoleixen una alçada inferior. Finalment les capes de tensió es visualitzaren només en els experiments portats a terme amb la màxima rugositat i es defineixen com una successió de vòrtexs creats en el mateix gra. Aquestes últimes estructures estan relacionades amb els vòrtexs inicialment descrits ja que aquests es formen amb les estructures romanents de la capa de tensió just quan es produeix el revers del flux.

El treball presentat en aquesta tesis es basa en dos problemes de mecànica de fluids. No obstant confirma que la tècnica del PIV és aplicable a fenòmens totalment diferents.

Preface

The research reported in this dissertation was carried out at different universities in collaboration with other cientifics:

(i) Department of Applied Mathematics and Theoretical Physics at the University of Cambridge between February 2011 and May 2011. Supervised by Prof. Stuart Dalziel.

(ii) Department of Civil and Environmental Engineering at the Ven Te Chow Hydrosystems Laboratory in the Department of Civil and Environmental Engineering at the University of Illinois at Urbana Champaign. Supervised by Prof. Marcelo H. Garcia and Prof. Keneth T. Christensen in collaboration with Jose Mier.

Experiments described in Chapter 2 were conducted by myself and supervised by Prof. Dalziel. Experiments included in Chapter 3 and 4 were carried out initially in collaboration with Jose Mier and supervised by Prof. Garcia and Prof. Christensen. This thesis does not contain experiments carried out by anyone else.

The contents described in Chapter 3 were presented at the 16th International Symposium on Applications of Laser Techniques to Fluid Mechanics in Lisbon, July. This research was selected to be published in the special issue publication that Experiments in Fluids is going to publish. Then Chapter 3 is the paper sent to the journal which is now under revision and waiting for the comments from journal's reviewers.

Any part of this thesis is being submitted for any other degree at any other university.

Table of Contents

List of Tables

List of Figures

List of Symbols

Variable	Description	Chapter
A	amplitude of oscillation	3-4
A_c	area of the core	2
a_k	time dependen coefficient of the POD decomposition	3-4
D	dimensionless diameter of the primary vortex ring	2
D_{50}	median diameter size of the sediment bed	3-4
d_p	diameter of the particle in the object space	1
D_p	diamteer of the pores	2
d_I	Size of the interrogation area	1
d_s	diffracted diameter of the particle	1
D_s	internal diameter of the pump	2
D_t	diameter of the tube	2
d_τ	diameter of the particle in the image space	1
E_n	energy contribution of each mode	3-4
f_w	friction factor	3-4
g	Gravity	2
h	thickness of the foam	2
$\underline{k}$	permeability tensor	2
$\underline{K}$	hydraulic conductivity tensor	2
k_{bn}	callibration coefficient for Vbn	1
K_r	radial component of the hydraulic conductivity	2
k_s	relative roughness of the sediment bed	3-4
k_t	callibration coefficient for Vt	1
K_θ	azimutal component of the hydraulic conductivity	2

K_y	vertical component of the hydraulic conductivity	2
L_s	stroke length	2
M	magnification factor	1
N	formation number of the vortex	2
n	POD mode	3-4
P	non-hydrostatic pressure (Pa)	2
p	non-hydrostatic pressure (m)	2
q	vertical flux exchange between the ambient fluid and the foam	2
$\vec{q}$	flow of a fluid through a porous media	2
q^-	flux exchange entering the foam	2
q^+	flux exchange coming out of the foam	2
q_Ω	flux of vorticity along the interface	2
r	radial dimension	2
Re_β	Stokes length Reynolds number	3-4
Re_p	ground water flow Reynolds number	2
Re_w	wave Reynolds number	3-4
t	time	2
T	period of oscillation	3-4
$\vec{u}$	velocity of the flow	1-3
u	horizontal component of the velocity	2
U	instantaneous horizontal velocity	3-4
u'	fluctuation of the horizontal velocity	3-4
u_*	friction velocity	3-4
u_{*m}	maximum friction velocity	3-4
U_0	mean horizontal velocity	3-4
U_{0m}	amplitude velocity of oscillation	3-4

$\vec{u}_H$	high-pass filtered velocity field	3-4
$\vec{u}_L$	low-pass filtered velocity field	3-4
$\tilde{u}_m$	dimensionless form of the maximum u over time	2
v	vertical component of the velocity	2
$\hat{v}$	maximum overt time of the mean vertical velocity along the radius	2
V	instantaneous vertical velocity	3-4
v'	fluctuation of the vertical velocity	3-4
$\vec{V}_{bn}$	Normal component of the velocity	1
$\vec{V}_{eff}$	Component of the velocity measured by the hot wire anemometer	1
$\hat{v}_i$	correction of the positive velocity	2
$\vec{V}_n$	Normal component of the velocity	1
V_r	vertical propagation of the vortex ring	2
$\vec{V}_t$	Parallel component of the velocity	1
x	streamwise dimension	3-4
y	vertical dimension	
$\tilde{Y}$	Dimensionless vertical position of the core of the primary vortex ring	2
y_r	maximum rebound vertical position	2
y_t	vertical position where the core starts decelerating	2

α	angle of anysotropy	2
β	Stokes Length	3-4
β_i	correction factor for positive velocities	2
δ	boundary layer thickness	
δ_1	inverse of the stokes length	3-4

Δz	Thickness of the light sheet	1
φ	phase shift between u_{*m} and U_{0m}	3-4
φ_k	spatial functions of the POD decomposition	3-4
Γ	circulation	2
λ	Wave length of the laser	1
λ_{ci}	swirling strength	3-4
μ	dynamic viscosity	
υ	cinematic viscosity	
ρ	density	
τ	total shear stresses	3-4
τ_υ	viscous stresses	3-4
τ_{Re}	turbulent stresses	3-4
ω	angular velocity of oscillation	3-4
Ω	vorticity	
Ω_{max}	maximum vorticity value from the primary vortex ring	2

List of Abbreviations

ADV	Acoustic Doppler Velocimeter
DAMTP	Department of Applied Mathematics and Theoretical Physics at the University of Cambridge, UK.
DEHMA	Departament d
GITS	Grup d'Investigació en Modelització de Conques i Transport de Sediments.
LDV	Laser Doppler Velocimeter.
LSV	Laser Speckle Velocimetry.
LIM	Laboratori d'Enginyeria Marítima.
MRI	Magnetic Resonance Imaging.
PIV	Particle Image Velocimetry.
POD	Proper Orthogonal Decomposition.
PTV	Particle Tracking Velocimetry.
UIUC	University of Illinois at Urbana Champaign.
UPC	Universitat Politècnica de Catalunya.

Acknowledgements

The research presented in this dissertation was carried out at three different universities all over the world. Therefore many professors and colleagues have left their footprint in it.

First of all I would like to thank my supervisor Prof. Allen Bateman for his work and direction. Also for being open-minded, giving me the opportunity to move abroad to work in different laboratories with some of his colleagues, which made possible the conclusion of this thesis. Regardless of the distance and the time zones he was able to skype-meet every week to be updated with my work abroad and moreover direct me under these conditions.

I also would really like to give special thanks to the professors I've been working with. Prof. Stuart Dalziel from University of Cambridge for being patient during my stay in the U.K, teaching me how to work with the PIV and being comprehensive after two years. Prof. Garcia to open me the doors of the Ven Te Chow Hydrosystems Laboratory at the UIUC giving me the opportunity to work and meet all the nice scientists working in it. To let me assist in his classes and solve my questions. Also to introduce me to Prof. Christensen who's been a very important support through his course and the endless questioning e-mails.

Thank you to Jose Mier for his patience with the Oscillatory flow and all the initial knowledge he gave me when I arrived at the Ven Te Chow Hydrosystems Laboratory. Any of the work presented in Chapter 3 and 4 would not have been possible without his help. Julio Barrios and Gianluca Blois, from the Department of Mechanical Enginyering: the patience of the latter teaching me how to use the Insight and ND-Yag Geminis laser and the generosity of Julio along all the postprocess of the experiments. The code I have used to obtain the variables printed in Chapter 3 and 4 was developed by him.

I would like to express my special thanks to all the laboratory technicians I've worked with. Their good and enormous job is a key to let science move forward, and they were always nice and decidisve to all the experimental set up problems I had: Quim Sospedra from Universitat Politècnica de Catalunya, David Page-Croft from the DAMTP in Cambridge University and Andrew Waratuke from the Ven The Chow Hydrosystems lab.

A special thank goes to my "male" office colleagues from the GITS group to stand me: Francesco Bregoli, Andres Diaz, Alberto Herrero and Vicente Medina. They have also helped me solving any type of questions. Cristina Fernandez and Khaled have been the last recruit of the GITS "patera" office and they will be a very good relieve.

I cannot name all the friends I got from my two stays abroad who made my daily life easier in a different country. They all know who they are. A big thank you. Science was easier with their support out of the laboratories. I will name specially my personal English correctors and dear friends: Alex Bryk and Eric Prokocki.

My mentor Prof. Mariàngels Puigví who always believed in me, encouraged and transmitted me all her happiness. Thank you for being flexible, understand me at any moment and advise me.

Dr. Gerber van der Graaf, thank you for the interesting meetings about PIV and science.

My partner in life, Manel, thanks for knowing how to calm me down and put a lot of humor anytime anywhere.

Finally, and specially, my family (the blood one and the in-law one) deserves the biggest thank you. They have been a true support during all these years no matter the place I was. They had the patience to encourage and advise me at any time.

Chapter 1: Introduction

This chapter explains the motivation of this thesis and the research aims proposed in each chapter. It also summarizes some of the measurement techniques used in fluid mechanics with an especial attention to PIV.

1.1 Motivation

Natural processes involving fluid mechanics tend to be complex in time and space. Quite often the research community tries to simplify some of the phenomena to understand their basis and further add more complexity once the simple process is known. This is the case of unsteady flows, sometimes simplified using pure oscillatory motion, and the fluxes generated when landing a helicopter, similar to a vortex ring.

Oscillatory flows can help on learning about some processes involving unsteady flows but have also a big importance by themselves. They are present in all sea and coastal interactions, animal heart processes and pumping of nutrients in the flora, among others. In the engineering field, oscillatory flows have been studied theoretically, experimentally and also directly in the ocean. However, the knowledge on the processes occurring at the boundary layer has not been perfectly described yet. A theoretical model is available for laminar flows over smooth walls, but further studies are needed towards other scenarios, for example, when sediment beds are used and also when the flow is not completely turbulent during an entire cycle.

On the other hand, vortex rings are present in volcanic eruptions, swimming squid, starting jets and some biological processes. Moreover, some industrial applications use vortex rings to resuspend particles trapped in a surface or other jet applications. Vortex rings have been widely studied during the last two centuries. From its mathematical expression to the first experiments looking at vortex ring formation characteristics, some of the latter experiments published are focused on the interaction of vortex rings with several types of boundaries such as thin grids or sediment layers. Some of these studies are pointing at the lack of knowledge on vortex rings impinging thicker permeable boundaries, and the implications of underground flows on the vortex ring evolution.

This thesis is aiming to improve the understanding of both phenomena: vortex rings and oscillatory flows. In particular, vortex rings are studied focusing on their interactions with porous boundaries (perpendicular to the symmetry axis of the ring) aiming to describe how the permeability affects the evolution of the ring. The research done in oscillatory flow focuses on the behavior of the boundary layer and the coherent structures forming in it. Specifically the flow regime covered in the experiments is in the laminar-to-turbulent transition. In this thesis, the PIV will be used to define the characteristics of each process, along with some numerical and theoretical models already known.

1.1.1 Background

The initial idea of this thesis was to combine PIV and PTV to study the mechanism of sediment entrainment in bed rivers. I started working on a PIV system, using the facilities generously lend by the LIM-UPC group together with the high speed camera of the GITS group. Meanwhile I started the design of a new facility to be built at the Laboratori de Morfodinàmica Fluvial from GITS-DEHMA, to be used to study sediment entrainment. However the complexity of the PIV devices and some difficulties during the experimental periods made us arrange a short stay in a place with more experience with this experimental technique in order to learn in situ how to work with the PIV. From this decision we got the opportunity to visit the DAMTP in Cambridge University. At the same time, the option which required building a new channel to carry out the experiments of sediment entrainment failed, thus requiring the search of another laboratory to perform the experiments.

During the three months stay in Cambridge I learned how to work with PIV system by studying the effect of different permeable boundaries in a vortex ring impingement. The software used to process the recorded PIV images was developed by Prof. Stuart Dalziel who was conducting the work. This research led to Chapter 2 of this dissertation by means of being published by a journal. In parallel to my stay in Cambridge, the possibility to work at another laboratory with sediment entrainment yielded to the collaboration with the Ven The Chow Hydrosystems Laboratory at the UIUC.

The collaboration with the UIUC was designed aiming the study of sediment entrainment along a river. However due to the daily life at a laboratory, after two months it was considered better to change the target and focus on the pure oscillatory flow using a PIV system. This system was completely different from the one used and learned in Cambridge mainly because the use of a powerful laser was required. With this system I played around with the collimator (cylindrical and spherical lenses), to adjust the position of the focal distance and the thickness of the laser sheet. Moreover the software used to record the images and process them was absolutely different as well. The research carried out at the UIUC has generated the publications added in this dissertation as described in Chapter 3 and Chapter 4.

All these experiences allowed me to learn about how to carry out a PIV experiment, but also the internal knowledge of the PIV post-processing and to work with two different softwares. Moreover, it opened my mind in terms of PIV applications in different scientific fields.

1.2 Flow velocity measurements

Experimental fluid mechanics have required over time an enormous effort on the development of the techniques used to acquire data. There are several measurable properties of a fluid, like temperature, viscosity, pressure, velocity among others. In this section we focus only in velocity measurements which can broadly be divided into tools that measure the velocity present in one point –point wise measurements- and the second group of techniques which measure an entire field of view –flow visualization techniques-. Some of these systems can be used either in a small laboratory or in the field; nevertheless the range of velocity being measured has to be in the range of the instrument.

All the techniques, the ones described below and the other techniques used nowadays, require at least an initial level of knowledge of the fluid and the phenomenon that will be further studied. Moreover they also demand an elevate experience in mathematics, particularly statistics. This is because each technique and instrument has its own limitations and therefore a single result of the property measured may be biased either due to the phenomenon in research or internal errors of the tool used.

When the focus of the research is the turbulence of a stationary flow –i.e. shear layer in flumes- the user must do an extensive preliminary analysis on the amount of the data required to get a representative mean. In this case, any measurement technique requires a minimum amount of time the researcher must be recording in order to get the representative mean of the point being measured.

Tavoularis (2005) is considered to be reference book for experimental fluid mechanists as it describes most of the techniques available when his book was first printed in 2005. It also gives the main statistical keys when analyzing the acquired data. However, a minimum knowledge of the fluid and the phenomenon being studied is required to determine correctly its characteristic parameters.

1.2.1 Point wise measurement techniques

ADV: Acoustic Doppler Velocimetry

This is one of the oldest techniques but still very present nowadays in laboratory and in the field. Based on Doppler phenomenon the shifting of the frequency of the signal emitted by the instrument, the ADV can measure up to three components of the velocity at a single point.

Figure 1.1. Example of a down-looking ADV manufactured by SonTek.

Figure 1.1 illustrates an example of the typical ADV used in the laboratory (ADV used in the field are normally larger in diameter) in its down-looking version. The transmitter is located at the center of the three legs, also called beams, and acting as receivers, Figure 1.2. The beams are typically between two to four, depending on the number of components of the velocity that will be measured. In the case of the four beam type, the fourth receiver is used to improve the measurement and reduce the error.

The basis of the ADV is the well-known Doppler phenomenon. However ADV uses a volume of fluid where the signal is repelled to the receivers, thus the result is representative of the volume of fluid. In fact each beam measures a component of the velocity.

Regardless of their manufacturer most of the instruments require, in general, five different input variables before starting using the ADV: i) the temperature of the water; ii) the salinity of the fluid; iii) the length of the control volume, represented as a cylinder, Figure 1.2; iv) the maximum velocity measured and v) the frequency of the emitted signal. Each one of these variables has an error associated that has to be taken into account when choosing the value: i-ii) the velocity of the signal is conditioned to these variables; iii)larger volumes imply larger errors;

ii) lower values of the maximum velocity than the real ones will underestimate the real instantaneous velocity v) the frequency of measurement will be linked to the Kolmogorov scale through the transformation from time frequencies to spatial scales (Taylor's hypothesis) thus the spectral analysis will be conditioned to this choice.

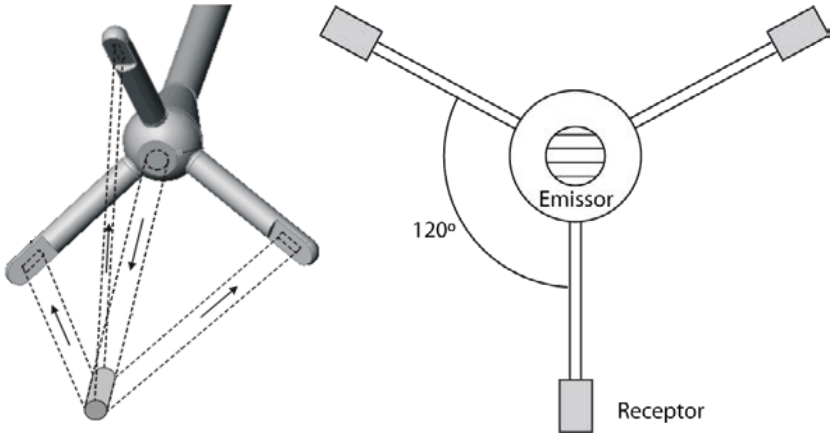

Figure 1.2. Details of a 3 beam down-looking ADV.

The system subjecting the ADV has to be completely quiet otherwise noise due to this motion will be transmitted to the receivers. When ADV's are used in the field and they are subjected to a boat and the motion of the boat has to be inserted in the analysis.

ADV can be used in any fluid that does not affect the material of the instrument. However when water is used, some dirt must be added to the water in order to reduce the noise of the received signal. In this case small particles ($\sim 10\mu m$) like glass beads can be used. In the field no particles are required because the cloudiness already present is useful.

LDV: Laser Doppler Velocimetry

The LDV technique, developed in the 1970s, is also based on the Doppler phenomenon like the ADV. However instead of using a sound signal the LDV uses a collimated laser beam, Tavoularis (2005). Therefore a photodetector is needed to receive the signal reemitted by the particle and transform the signal into the real velocity of the control volume.

A dual-beam LDV is the typical technique developed to reduce the errors in the final signal The laser beam is splitted into two parallel light beams which are collimated by a spherical lens. The function of this lens is to reduce the diameter of the beam at a distance equal to the focal length thus reducing the noise of the tales present in the Gaussian signal of the beam. The signal of each beam is shifted according to the Doppler effect in a small particle crossing the

measuring volume. Due to the dispersion each reflected beam is collected through a lens that drives the light straight to the photo detector.

The characteristic variables defining an LDV system are: i) the wavelength of the emitted laser; ii) the frequency of the emitted laser; iii) the temperature of the fluid and iv) the angle formed by the laser transmitter and the photo detector. The photodetector measures the voltage of the reflected beams which is related to both light frequencies and the Doppler frequency difference.

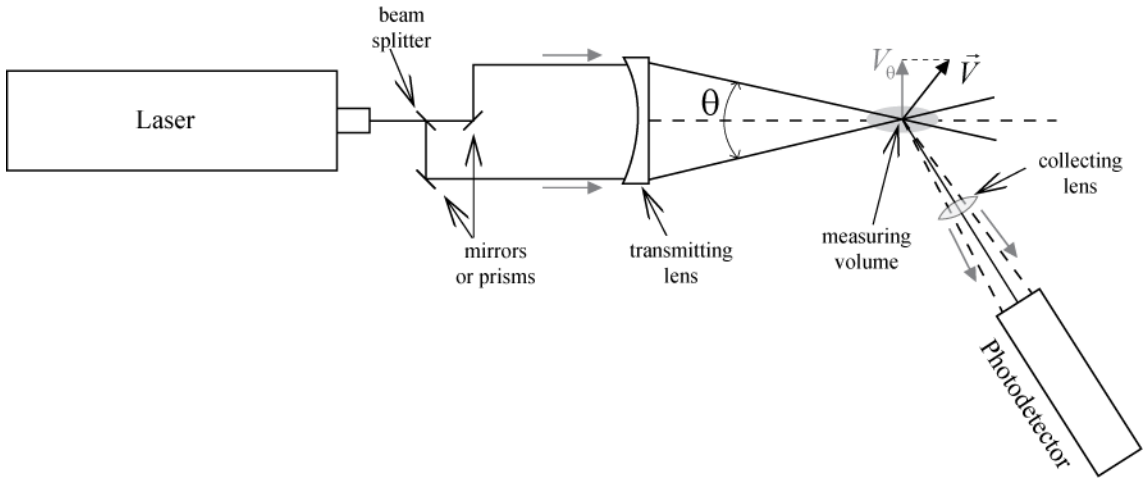

Figure 1.3. Sketch of an LDV from Tavoularis (2005)

The use of tracer particles is also required for LDV, like in the ADV case. However, LDV is a more complicated technique in terms of the user since it requires an elevate level of safety due to the laser.

Hot-Wire/ Hot-Film Anemometer

Hot-wire and hot-film probes are techniques based on heat transfer. They were used prior to the LDV being the only method having a resolution high enough to measure turbulence. Wires are usable in gases whereas films are usable either in gases or fluids.

Thermal anemometers are heated with a uniform temperature. When the flow passes the wire it cools it down, changing its resistance by changing the temperature. Different velocity magnitudes cause a single cooling effect. The measured value is the voltage emitted by the wire/film which is directly related to the velocity of the flow. Therefore an intense individual process of calibration is required in this technique.

The main problem of the hot-film probes is that they require isothermal environments otherwise a small change in the temperature of the flow will be read as a change in velocity. A

single probe is used only to capture one direction, however fluctuations in other directions are always present. Therefore some cooling effect may be related to other components of the velocity and the effect of supports, as shown in Figure 1.4. $\vec{V}_{eff}$ is the component of the velocity that it is really affecting the probe following

$$V_{eff} = \sqrt{V_N^2 + k_T^2 V_T^2 + k_{BN}^2 V_{BN}^2}\,, \tag{1.1}$$

where V_T is the magnitude of the component parallel to the sensor –and to the vertical axis in the case shown in Figure 1.4-, V_{BN} is the magnitude of the component normal to the sensor –and parallel to the cross-spanwise axis in the case shown in Figure 1.4-. k_T^2 has to be calibrated individually but it moves between 0.05 and 0.2 and k_T^2 has typical values between 1.1 and 1.2 Tavoularis (2005).

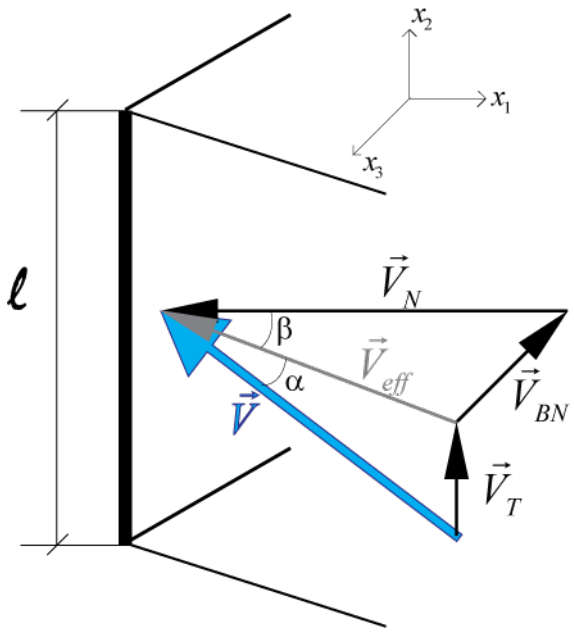

Figure 1.4. Sketch of a hot-wire/hot-film anemometer.

Ideally during the calibration process wires/films are oriented in order to minimize α and align the probe perpendicular to the main flow direction.

Another problem when using wire/films is the downstream wake produced by the interference of the wire itself to the flow. However this is minimized by using very thin probes and the remaining effect is considered in the V_{BN} component.

If a 2D mean flow is to be measured a cross-wire anemometer is used. This is two single wires oriented differently but avoiding the contact between them. Moreover they have to be aligned in a way that the wake of one wire does not affect the downstream wire.

1.2.2 Spatial measurement techniques

This group of techniques requires image recording in any case. The tracer may vary according to the technique but the set-up common in all the methods is at least a camera, and a good illumination system.

There are several tracers can be used in order to visualize the evolution of a magnitude along an entire experiment. Air bubbles were the first tracer to be used either in air flow experiments and liquid. In the case of hydrogen bubbles used in water experiments the differences in density make them be useless for some phenomenon. This is one of the principle characteristics that a tracer must have: it cannot interact with the flow and has to be neutrally buoyant to follow the flow. The size of the particles is also important since they have to follow instantaneous velocities. There are some tracers that satisfy this attributes, for example fluorescence and the MRI. The latter is one of the most recent developed technique, Bonn et al. (2008), which uses the spin properties of atomic nuclei as the tracer. However the typical tracers used in some of the most popular spatial measurement techniques are small particles with particular optical properties. Particles should not interact with the flow and will have to be also neutrally buoyant depending on the material of the particles.

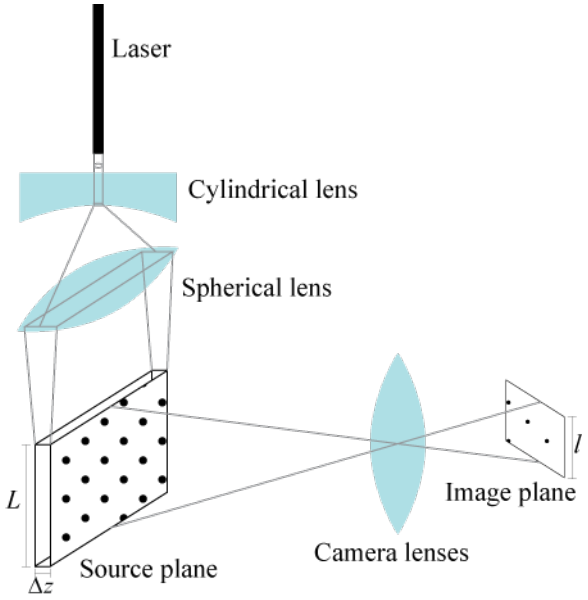

Figure 1.5. Sketch of the optics needed to perform PIV.

This section describes only techniques using particle displacement methods. These methods are based on the simple idea of tracing a single particle during different instants in a fixed field of view. Then, between two instants the eulerian velocity of the particle is defined by

$$\vec{u} = \frac{\Delta \vec{x}}{\Delta t}. \tag{1.2}$$

The main difference between the three methods described below is the number of particles present in the source and image planes. Two common variables are defined: N_s is the density of particles present inside an interrogation area in the source plane and N_I is the density of particles inside an interrogation area in the image (Westerweel (1993)) see Figure 1.5. Therefore the mathematical hypothesis and the statistics will vary from one technique to the other in order to keep the original idea still valid.

Also only 2D set ups will be characterized since this is the technique used for the experiments in this dissertation, Figure 1.5. However the reader must know that there have been many improvements in 3D set ups and processing using the same principles as in the 2D cases.

In terms of the light sheet, the three techniques described below assume an infinitesimal. In reality this is not true and the light sheet has a finite thickness Δz as shown in Figure 1.5. Typically it is assumed that the light sheet is created with a laser light. However experiments carried out in Chapter 2 use a 300 W xenon arc lamp fitted with a parabolic dichroic reflector.

When a laser is used, optics to transform the initial circular section laser into a planar sheet are important. Figure 1.5 shows how a cylindrical lens is used to transform the circular section of the laser into a planar section, followed by a spherical lens to adjust the thickness of the planar section. It is optimal to have the focal length of the spherical lens located at the center of the source plane, since it concentrates the higher intensity of light. If the focus of the study is a boundary layer and the phenomenon occurs in the vicinity of a boundary, then the focus of the spherical lens should be located slightly above the boundary to avoid reflections. This is the point with higher intensity and thus less noise on the PIV results.

The optics of the camera will define the resolution of px/mm through the magnification factor, M

$$M = \frac{image}{real} = \frac{L}{l}, \tag{1.3}$$

where L is the image size and l is the real size. In order to ensure the highest number of particles present in the light sheet to be in focus, the depth of focus from the camera

$$\delta_z = 4\left(1 + M^{-1}\right)^2 f_{\#}^2 \lambda, \tag{1.4}$$

has to be higher than the thickness of the source plane

$$\delta_z > \Delta z\,. \tag{1.5}$$

In Eq. (1.4) $f_\#$ is the inverse of the f number of the camera lens and λ is the wavelength of the laser light.

PTV

This is the method with lower source and image density, $N_s \ll 1$ and $N_I \ll 1$. This means that there is no overlap between particles both in the source and in the image planes. In this case particles are traced individually thus yielding velocity vectors only at the position of the particles.

PIV

Very good guides have been published about the entire process of PIV. Some of them are: Westerweel (1993), Adrian (1991), Prasad (2000) and Adrian (2005)

This is the case when: $N_s \ll 1$ and $N_I \gg 1$. However a number between 8 to 10 particles in an interrogation area is considered optimal for the image processing.

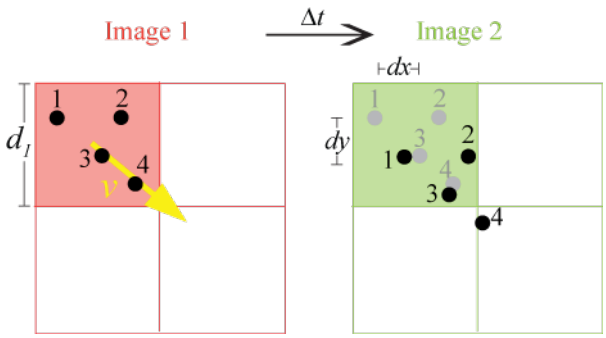

Figure 1.6. Sketch of the PIV processing.

From Eq. (1.2) a shorter Δt yields better approximation results to the real $\vec{u}$ vector. Yet an infinitesimally small Δt is impossible. Prasad (2000) suggests

$$\Delta t \leq 0.25\frac{d_I}{MU}, \tag{1.6}$$

with d_I the size of the interrogation area (Figure 1.6) and U the expected flow velocity in the source plane. Nevertheless an average of 10 px particle displacement between one frame and the following is needed to get a 95% of probability that 4 particles will remain in the interrogation area, following Poisson statistics, and is another rule of thumb applied by PIV

users. Figure 1.6 shows a sketch summarizing the simple mathematics behind PIV. However internal process requires higher levels of mathematics that will be described below.

Figure 1.7 shows an example of a raw PIV image and the final result obtained after PIV processing.

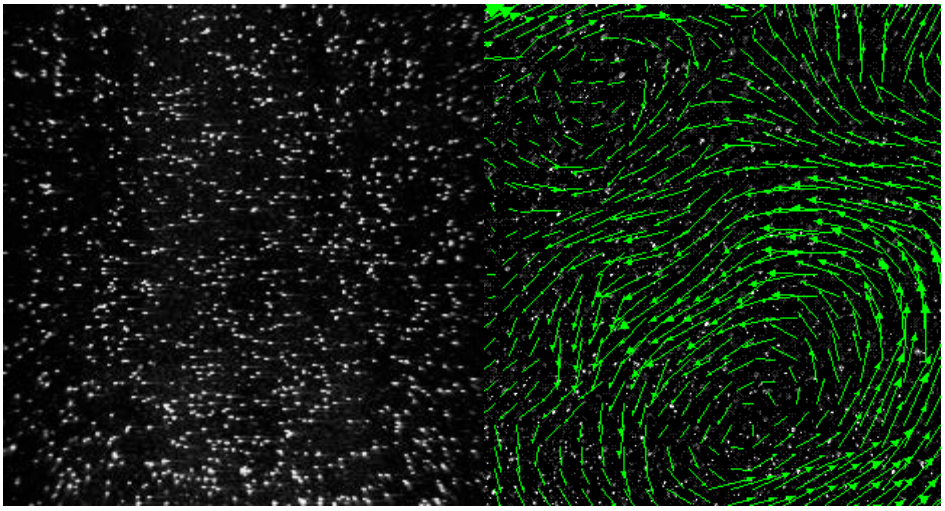

Figure 1.7. Left: original image. Right: flow field obtained from the PIV analysis.

Particles in the source space are not represented as a single point in the image space, and its representation depends on geometrical factors and the behavior of light scattering:

$$d_s = 2.44\left(1+M\right) f^{\#}\lambda\,, \tag{1.7}$$

where d_s is the diffracted point source diameter in the image space. If this is combined with the geometric considerations the effective diameter of a particle in the image space is

$$d_\tau = \sqrt{\left(Md_p\right)^2 + d_s^2}\,, \tag{1.8}$$

which is has to be between 2 and 3 px. Not too big because PIV uncertainty is proportional to d_τ but not too small to be less than the resolution of the image space. It is found that small particles may cause peak-locking, which consists on a biased error due to the lock of the interrogation results onto integer pixel values. At this stage it is worthwhile to recall that the light sheet is not infinitesimally small and some particles may be out of focus. This adds more noise on the vector field.

The processing consists on choosing the best pattern matching technique. Firstly, a cluster is defined from *Image 1* by dividing it into subdomains called interrogation spots (also named interrogation areas) which define the particle population –recalling that at least 8 particles

have to be inside each window-, see Figure 1.6. Secondly, the first spot in *Image 1* is correlated to all the spots forming *Image 2* using a correlation analysis. The maximum in the resulting correlation matrix defines the average displacement of particles present in the first spot in *Image 1*. The spatial resolution is defined by the size of the spot. However, due to the Nyquist criteria the sampling frequency has to be twice the frequency with the resolution wanted. Therefore, the spots are adjacently overlapped by a 50% of the window size, d_I; thus the final grid of vectors will be linspaced $d_I/2$. Most of the softwares used nowadays permit different percentages of overlapping; however the user has to be aware of its influences on the final resolution of the vector grid. Moreover, in order to reduce the computational effort some codes permit the user to introduce a first guess of the motion called offset.

The correlation algorithm also depends on the software used. Typically the original process carried out to obtain the average displacement is the convolution between the spot in *Image 1* and *Image 2*. Nevertheless other softwares like *Digiflow*, Dalziel (2006), allow other algorithms such as the absolute difference, its square or other powers of this difference. Weak correlation peaks may be related to noise and the SNR has to be controlled too, Adrian (1999). Also high Δt imply particles getting out of the spot which can cause the "ghost" correlation effect, by perfectly matching different particles. In order to reduce some of these problems, a recursive interrogation process with grid refinement may be carried out. However this increases the computational effort and time.

The maximum accuracy reached by the initial guess is the pixel size, however subpixel accuracy can be reached by fitting the curve of the discrete correlation results. For instance fitting the results obtained after the interrogation to a quadratic or centroid curve to minimize peak-locking effects.

Final results after the interrogation and subpixel fitting are always validated by comparing each vector to its immediate neighbours. When an invalid vector is found, it can be replaced by the second or third maximum found in the interrogation matrix. Sometimes when this two maximums are also invalid the vector is replaced by the mean of median of the neighbour vectors.

LSV

Opposite to the PTV the Laser Speckle method has overlapping in the source and image planes: $N_s \gg 1$ and $N_I \gg 1$. Westerweel (1993) suggests that the mathematics to obtain the velocity vectors in LSV are the same for PIV and therefore it seems that they can be described as a single measurement technique.

1.3 Research Aims and Structure of Thesis

The research summarized in this dissertation is aiming to apply the PIV technique to two different fluid mechanics phenomena: i) the evolution of a vortex ring towards different permeable beds and ii) the pure oscillatory flow in the laminar-to-turbulent transition regime over smooth and rough beds and the characterization of coherent structures formed during the oscillation.

The structure of the thesis is coherent with the aims presented:

- Chapter 2: analyses the impingement of a vortex ring towards four different permable boundaries and compares it to the behavior of the vortex with a solid boundary.
- Chapter 3: characterizes the experiments of a pure oscillatory flow over two rough and a smooth bed. It compares the results obtained with the PIV technique with other authors using point-wise measurement techniques.
- Chapter 4: describes the coherent structures detected in the pure oscillatory flow experiments. Structures are described from its formation until they completely disappear. This chapter also analyzes the snapshots using the POD technique.
- Chapter 5: summarizes the main results obtained in this thesis in both topics and future work that can be done in each direction.

Chapter 2: Vortex Ring Interactions In Permeable Boundaries

This chapter describes the experimental work carried out to study the behavior of vortex rings moving towards different permeable boundaries. It compares the results obtained with four permeable boundaries with the vortex ring impinging a solid boundary.

2.1 Introduction

Vortex rings occur in many unsteady processes found in nature. Volcanic eruptions, swimming squid, starting jets and some dolphin games all involve structures taking the form of vortex rings. Some industrial processes use the impingement of a vortex ring to a solid surface to dislodge the particles that can be trapped in it, (see Staymates & Settles (2005)), and vortex rings are a serious issue when landing a helicopter (e.g. Stewart (1951), Newman et al. (2001)).

The first analysis of a vortex ring structure was described by Kelvin (1867) for vortex rings with a very thin core compared to the ring diameter. At the opposite limit, Hill (1894) detailed the characteristics of a vortex ring with the core diameter equal to the diameter of a vortex ring, a structure now known as the Hill's spherical vortex. Batchelor (1967) described vortex rings as a single circular line vortex for inviscid fluids where the core was infinitesimally small and the propagation velocity was inifinite. Subsequently, Norbury (1973) proposed an expression for vortex rings with a thin size of the core and a finite velocity of propagation. His work also analysed theoretically the entire range of vortex rings with different core sizes. Maxworthy (1977), carried out a series of experiments with different vortex ring formation characteristics to study its influence on the velocity of propagation, the core size and the existence of instabilities. Although vortex rings have been the focus of many studies since the last 150 years, they are still being an active area of research.

A model for the canonical case of a vortex ring impinging a perpendicular solid wall was proposed by Saffman (1979), using the mirroring of a vortex pair moving towards a symmetric vortex pair (with the axis of symmetry perpendicular to the direction of the motion). Cerra & Smith (1983) and Walker et al. (1987) pioneered the experimental study of the vortex ring impacting on a solid boundary with Orlandi & Verzicco (1993) and Swearingen et al. (1995) undertaking some of the earliest simulations. They all found a stretching of the core when approaching the wall, an increase in the diameter of the vortex ring and the existence of a rebound of the core due to the formation of a secondary vortex with opposite sign, confirmed by a study of colliding vortex rings by Lim et al. (1991).

More recently, Staymates & Settles (2005), Munro & Dalziel (2005), Bethke (2008), Munro et al. (2009) and Masuda et al. (2012) among others have turned attention to the possibility of resuspension due to a vortex ring impacting a bed of particles. Of particular interest here is the suggestion by Bethke & Dalziel (2012) that the permeability/porosity of the sediment bed may influence the dynamics of the interaction.

So far, the introduction of porous boundaries interacting with vortex rings has been related mainly to thin permeable screens with different porosity and wire diameter –also known as mesh, grids and screens in this document-. Adhikari & Lim (2009) and Naaktgeboren et al. (2012) first compared the impact of a thin porous screen on the vortex ring propagation with the interaction with a solid wall, varying mainly the Reynolds number and the screen porosity, defined as the ratio between the void spaces and the total area of the grid. They found that porosity influenced the extension of the vortex ring diameter: rings impinging higher porosity screens did not increase their diameter while approaching the grid. Moreover, the existence of the secondary vorticity cores disappeared and the vortex ring was transmitted through the screen. Hrynuk et al. (2012) showed how the scales of the grid also influenced the vortex/mesh interaction. In particular, they studied constant porosity grids with variable wire diameter using constant Reynolds number vortex rings, and showed how the propagation of the ring beyond the grid was influenced by the length scales of the mesh.

The work presented herein focuses on the interaction of vortex rings with thicker permeable boundaries. This research aims to explore the influence of such boundaries not only on the vortex ring propagation through water but also through the porous medium itself. The first goal is reached experimentally whereas the ring propagation inside the foam is studied numerically.

This section is organized as follows. The experimental methods and basic configuration are introduced in section 2.2, while section 2.3 presents the main experimental results. These results are discussed in section 2.4 where a simple numerical model for the flow within the porous boundary is introduced. .

2.2 Materials and Methods

The experiments were carried out using a 36 litre acrylic tank, essentially the same as that described by De Rooij et al. (1999), Munro et al. (2009) and Bethke & Dalziel (2012). The tank has a square base (300×300 mm), and a 400 mm height. The front face was left completely transparent, while the bottom and two lateral faces were covered with matt black plastic film to avoid the influence of ambient light; the third vertical face was covered with the same film except for a narrow vertical slot to allow illumination by a thin light sheet (see Figure 2.1). The lower boundary was either solid (using the base of the tank), or porous (using blocks of reticulated foam cut to fit within the tank; see below). In either case, the tank was always filled to a depth of 300 mm above the top of the porous/permeable boundary: this is the bottom of the

tank in the solid boundary experiments and the top of the porous layer in permeable boundary cases. The tank was filled with a column of salty water (ρ= 1.02 kg/l).

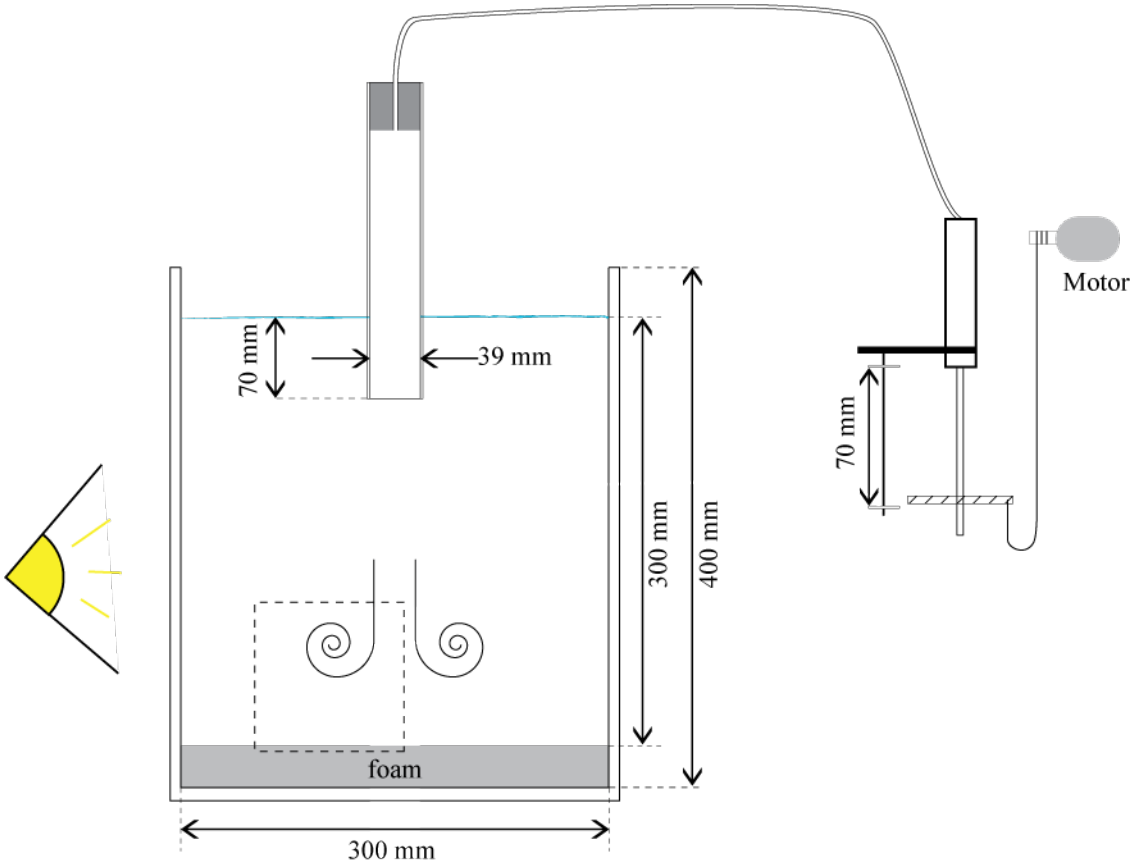

Figure 2.1. Sketch of the experiment setup. Dashed square marks the field of view recorded.

The vortex ring was created in the same manner as used by Munro et al. (2009) and Bethke & Dalziel (2012). In particular, a PVC tube of internal diameter D_t = 39 mm was submerged to a depth of 70 mm beneath the surface of the water. A slug of water was driven out the end of the tube by introducing air from a bicycle 'track pump'. This pump, with internal diameter D_s = 29 mm was actuated by an electric motor connected to its handle via a piece of nylon cord wound onto a capstan. For the experiments presented here, the stroke length for the pump was set to L_s = 70 mm and the stroke time held constant at T_s = 141.9±1.1 ms. Assuming there was no air compression from the pump to the hose, the formation number for the vortex rings,

$$N = \frac{L}{D_t} = \frac{L_s D_s^2}{D_t^3}, \qquad (2.1)$$

is around one. Here, L is the length of the slug of water expelled from the tube.

Table 2.1: Characteristics of the foams used. Ppi Range and height (*h*) values are given by the manufacturers. Vertical hydraulic conductivity (K_y) values are obtained experimentally and vertical permeabilityies are obtained using viscosity at 20°C. Pore diameter (D_p) and angle of anisotropy (α) are obtained from visual observations. Re_p is obtained from Eq. (2.16).

Foam name	*Ppi Range*	D_p (mm)	h (mm)	K_y (m/s)	k_y (m^2)	α	Re_p
K24	60	0.5	25	0.24	$2.6\cdot10^{-8}$	45°	5.5
K48	30	1	25	0.48	$5.1\cdot10^{-8}$	45°	17.6
K65	20	2	25	0.65	$7.0\cdot10^{-8}$	60°	57.9
K79	10	3	50	0.79	$8.5\cdot10^{-8}$	60°	173.7

Table 2.1 describes the main characteristics of the four different reticulated polyether foams used to form the porous boundary. Each had an internal structure that was geometrically similar but differed in scale (pore diameter).The hydraulic conductivity tensor of each foam,

$$\underline{k} = \underline{K}\frac{\nu}{g} \tag{2.2}$$

was determined by ensemble averaging the results obtained from 20 different Darcy's tests for each foam with an estimate error of ±0.25m/s. It was found that the two coarsest foams were not isotropic (*i.e.* the conductivity normal to the foam, K_y was found to differ from that in the plane of the foam, $K_r = K_\theta$) and so the angle of anisotropy α is given by the relation

$$K_r = \frac{K_y}{\tan(\alpha)}, \tag{2.3}$$

where α was determined visually and then used to obtain the corresponding radial permeability, K_r. This data is given in Table 2.1. For convenience, we identify the foam blocks based on the hydraulic conductivity values shown in Table 2.1 . Foam blocks K24, K48 and K65 all had a thickness of h = 25 mm, while K79, the coarsest (most permeable) foam, was thicker with h = 50 mm. In all cases, we define our coordinate system so that y = 0 is the top of the block of foam. We shall discuss in section 4 the influence this thickness may have had. Before each experiment, care was taken to ensure that no air bubbles were caught in the foam (a small quantity of wetting agent was used to assist this process and the foam blocks were kept submerged between experiments).

In addition to the four porous foams, we studied the impact of the ring on a solid boundary. We could treat this data as either the limit of zero permeability (placing our coordinate

origin $y = 0$ at the solid boundary) or the infinite permeability limit for a foam block of thickness h by considering the bottom of the tank as $y = -h$.

The experiments presented here were illuminated by a light sheet from a 300 W xenon arc lamp fitted with a parabolic dichroic reflector. Nearly columnated light from the lamp passed between adjustable aluminium strips on the side of the tank to generate a sheet with a thickness of about 3 mm. The experiments were recorded using a high-speed 1 MPixel camera (Photron SA1.1) at 1000 frames per second. The camera was fitted with a 60mm AF micro NIKKOR lens with a f = 2.8 aperture. For some experiments, the field of view covered the whole diameter of the vortex ring, although for others, only one side of the ring was visualised in order to improve spatial resolution. For such experiments, the camera was located around 360 mm from the light sheet.

Our main experimental results were obtained using Particle Image Velocimetry (PIV) on one half of the vortex ring (see sketch in Figure 2.1). As discussed in the next section, our field of view was sufficient to ensure it captured the majority of the interaction between the ring and the porous boundary. We used Pliolite VTAC particles with nominal diameter between 70 and 110 μm and specific gravity around 1.02. These particles were rendered neutrally buoyant through the addition of around 35 g/l of salt (NaCl) to the water in the tank. The PIV analysis was performed using the software Digiflow Dalziel (2006) with interrogation regions 21×21 px^2 at a spacing of 15 pixels giving an effective spatial resolution of 1.4 mm. A cubic spline algorithm was used to interpolate between PIV results and acquire feasible results at every pixel, with a final resolution of 0.63 mm/px.

We also present experiments visualised using a precipitation technique driven by the electrolysis of electrical solder. In particular, thin solder-covered (‘tinned’) copper foil was stuck to the inside of the open end of the PVC tube. A brief pulse of current was passed through this foil (attached to the positive side of a DC power supply; hydrogen bubbles were produced at the second electrode that was placed in a remote corner of the tank) to produce a cloud of white precipitate just prior to ejecting the vortex ring. This precipitate was largely confined to the boundary layer exiting the tube and so was wrapped up into the core of the vortex ring. With general illumination, the vortex rings were seen to remain essentially axisymmetric during their propagation and interaction.

2.3 Experimental Results

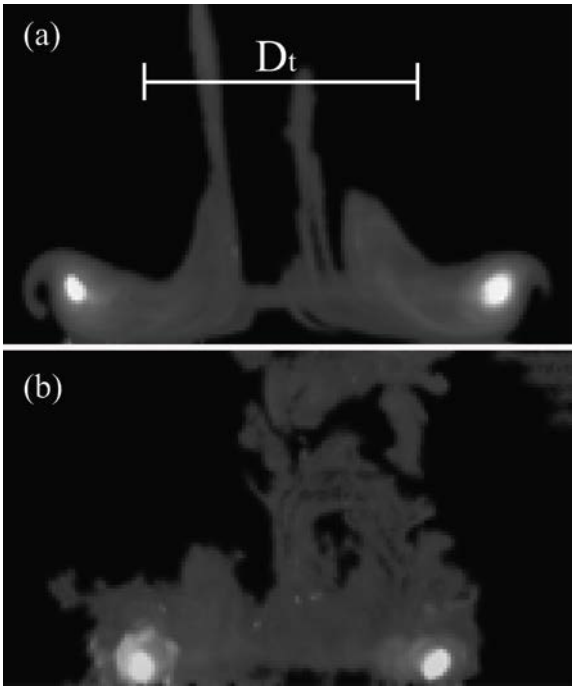

Figure 2.2. Comparison of the vortex ring interaction between solid boundary –upper- and a coarse foam – lower- visualized using the electrolytic precipitation of tin chloride.

We begin with some qualitative visualisations of the interaction between the vortex ring and the various boundaries using the precipitation technique described in the previous section. Using a sheet of light passing through the axis of the ring, Figure 2.2a shows the interaction with a solid boundary, K0, while Figure 2.2b shows the interaction with the K79 (coarsest) foam. Both images are for the same time after exiting the PVC tube. In the absence of the boundaries, the two rings would be indistinguishable and their cores would be located at $y = 0$, the position of the boundary. However, Figure 2.2a illustrates clearly the radial stretching and vertical deceleration of the ring as it begins to interact with its 'image' in the boundary. In contrast, the concept of an image vortex ring to impose no normal flow across the boundary is not applicable to the porous boundary in Figure 2.2b. Although there has been some stretching and deceleration of the ring, this is nowhere near as pronounced as was seen for the solid boundary. As we shall see, this behaviour is typical for the permeable interactions. The ring's interaction with the solid boundary also deposits secondary vorticity of the opposite sign on the wall as a result of the no-slip boundary condition. The presence of a small amount of precipitate outside the core of the ring makes this visible in Figure 2.2a where separation of this secondary vorticity is leading to the emergence of a coherent secondary vortex that is beginning to wrap some of the precipitate around it. While this is happening around the entire circumference of the vortex ring, the

illumination makes this clearest just to the left (and below) the left-hand core in the figure. In contrast, there is no clear evidence from Figure 2.2b of such a structure existing in the interaction with the porous boundary.

Figure 2.3 offers the same form of visualisation across our entire range of porous and solid boundaries. These images are arranged so that the boundary permeability increases from left to right. The upper row of the figure (Figure 2.3a-e) shows the similarity of the rings at a height $z = D_t$ above the wall (henceforth we label this height as our time origin $t = 0$). The cores of the rings are at the same height and of the same size; any small variations are due to imprecisions in the way the precipitate is introduced. The images in the lower row of Figure 2.3 (panels f to j) are from the same five experiments as the upper row but show the position of the cores with $\tilde{t} = \dfrac{t}{D_t/V_r} = 1.05$ (V_r is the vertical velocity propagation of the ring before the deceleration starts). Clearly, increasing the permeability allows the rings to approach the boundary more closely while reducing the stretching of the diameter of the ring.

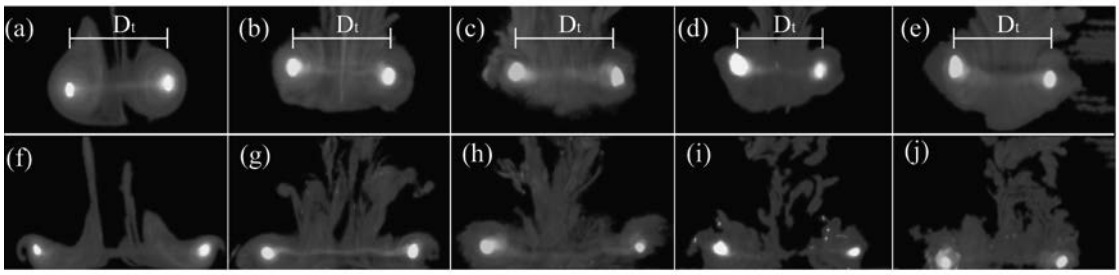

Figure 2.3. Upper row $\tilde{t} = 0$; lower row $\tilde{t} = 1.05$. Column-wise, from left to right with increasing permeability K0 (a,f), K24 (b,g), K48 (c,h), K65 (d,i), K79 (e,j)

Following Munro et al. (2004) and Bethke & Dalziel (2012), we turn now to our measurements based on PIV. Figure 2.4 shows velocity and vorticity fields at different dimensionless instants. Figure 2.4a-c shows the flow above the solid boundary (the symmetry axis of the vortex ring is located on the left-hand side of the field of view). As seen by previous authors and noted above, the no-slip boundary condition has deposited secondary vorticity on the boundary that has begun to separate to form a secondary vortex ring. This secondary vortex ring interacts with the primary ring to further retard and indeed temporarily reverse the primary ring's direction of vertical propagation. Secondary vorticity continues to be deposited on the boundary and is wrapped around the primary ring as the stronger circulation in the primary ring sweeps the secondary ring out and around it before compressing it back towards the axis. As discussed by others, e.g. Maxworthy (1977), Widnall et al. (1974), the compression of this secondary ring

plays an important role in the development of instabilities on and the eventual break up of the primary vortex ring.

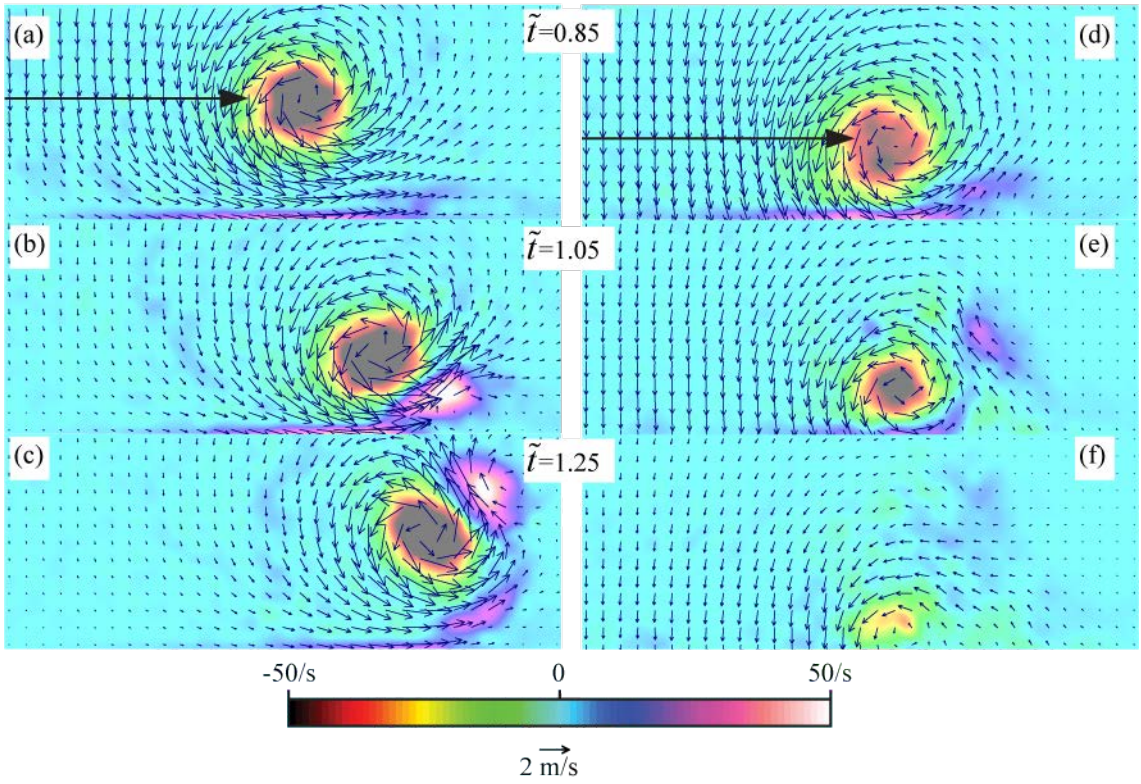

Figure 2.4. PIV results of a vortex ring approaching two different boundaries. (a) to (c) solid boundary (K0); (d) to (f) coarsest foam K79. Background variable: vorticity.

Figure 2.4d-f shows how the coarsest foam (K79) fundamentally changes the nature of the interaction. First, the K79 boundary lets the vortex ring get closer to the boundary and probably penetrate it. Second, the changes in diameter are not as significant when a permable boundary is used since the secondary vortex does not have the same intensity as in the case of the solid boundary interaction. Finally secondary vorticity is perceptible in Figure 2.4 (d) and (e) but is comparably weaker than the solid boundary case indicating it can also affect the apparent no slip boundary condition assumed in the K0 scenario.

In Figure 2.5 we summarise the behaviour of the core of the primary vortex ring with the ensemble of 10 PIV experiments for each of the different boundary permeabilities. In particular, we use the vorticity criterion of Bethke & Dalziel (2012) to locate the cores of the vortex rings from the PIV measurements. The trajectory of the cores is shown in Figure 2.5a. Here we plot, $\tilde{Y} = \frac{y}{D_t}$ against $\tilde{D} = \frac{2R}{D_t}$, where R is the distance from the symmetry axis to the centre of the core and Z represents the vertical position of the centre of the core. In the absence of a lower

boundary, the trajectory would be a vertical line with constant $\tilde{D}$. The solid line shows the behaviour of the core above the solid boundary, the diameter increasing as the ring approaches the boundary. Note the characteristic rebound of the core at $\tilde{D} \approx 1.7$. This is due to the coupling between the primary ring and the secondary ring following separation of the boundary layer. Figure 2.5b and c show the same trajectory data plotted as a function of dimensionless time. For the K0 boundary, the rebound is clearly visible after the ring's closest approach at $\tilde{t} \approx 1$ with $\tilde{Y}$ increasing then $\tilde{D}$ decreasing from $\tilde{t} \approx 1.1$.

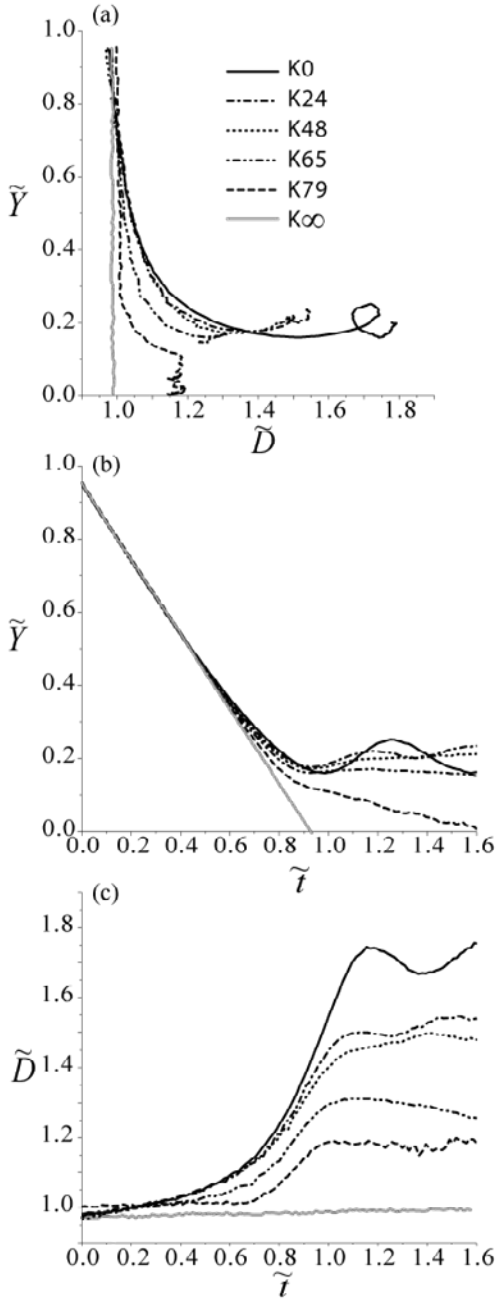

Figure 2.5. Comparison between scenarios with porous boundaries and solid boundary. a)Trajectory; b) vertical position evolution; c) diameter evolution.

As the permeability of the boundary increases (K24, dot-dashed lines), the radius of the ring grows slightly more slowly, Figure 2.5c, and the vertical velocity is reduced by less as it approaches the boundary, Figure 2.5b, resulting in the trajectory lying below that of the solid boundary until around $\tilde{t} = 1$ when the ring decelerates relatively quickly. A small rebound is evident, although compared with the rebound from the solid boundary, the rebound from K24 is smaller, earlier and at smaller radius. The trajectory above the K48 porous boundary (dot line) shows a slightly closer initial approach, more sudden and slightly later deceleration, and a smaller spread than either the solid boundary or K24. Although the approach of the core still changes direction (with the core moving away from the boundary for $\tilde{t} > 1.0$), the radius grows monotonically until much later.

The trajectories above the two coarsest foams (K65 dot-dot-dash lines and K79 long dashes) continue the trend of not expanding as much as they approach the boundary. Their approach velocity remains constant until about $\tilde{t} = 0.8$ after which they decelerate and begin to grow in radius more dramatically. There is some suggestion of a weak rebound for the K65 boundary (although the distance from the boundary remains nearly constant after $\tilde{t} \approx 1$ the radius decreases slightly), but none for the most permeable boundary, K79.

One open question is whether the thickness of the porous layer plays a role. It is obvious that for a very thin porous layer the thickness will be important (with the importance increasing with increased permeability), but it is less clear whether our current porous layers are sufficiently thick for their thickness to be unimportant. To this end, the grey line in Figure 2.5 replots the trajectory for the solid boundary case but offset downwards by h = 50 mm, the thickness of the most permeable (K79) foam. We can view this as representing the limit of high permeability where the porous boundary ceases to play a significant role and only the solid boundary of the tank is important. As can be seen in Figure 2.5a, the trajectory above this virtual K∞ foam by the time the ring reaches $\tilde{Y} = 0$ is nearly uninfluenced by the presence of a boundary and is clearly different from the ring approaching the K79 foam.

According to Bethke & Dalziel (2012) a vortex ring impinging a solid boundary starts stretching its diameter while reducing the velocity of propagation at a height equivalent to D_t. Figure 2.6(a) quantifies the height at which the ring notices the existence of a boundary, y_t, as a function of permeability by starting a decelerating process and an increase in diameter. As seen in Figure 2.6(a), the vortex ring velocity remains constant for longer (to a lower height) with more permeable boundaries. The extreme case is the, K79, when the ring starts decreasing the

velocity at a height equal to a 20% of the diameter of the tube. On the other hand, Figure 2.6(b) plots the maximum rebound height, y_r, the maximum height of the primary core after $\tilde{t} > 1$ in Figure 2.5 (c). In the most permeable case, K79, no rebound has been observed; we flag this by setting $y_r = 0$. Smaller permeabilities allow the vortex ring to slightly rebound increasing $y_r = 0$ up until its maximum in the solid boundary case when it is around a quarter of the tube diameter, D_t.

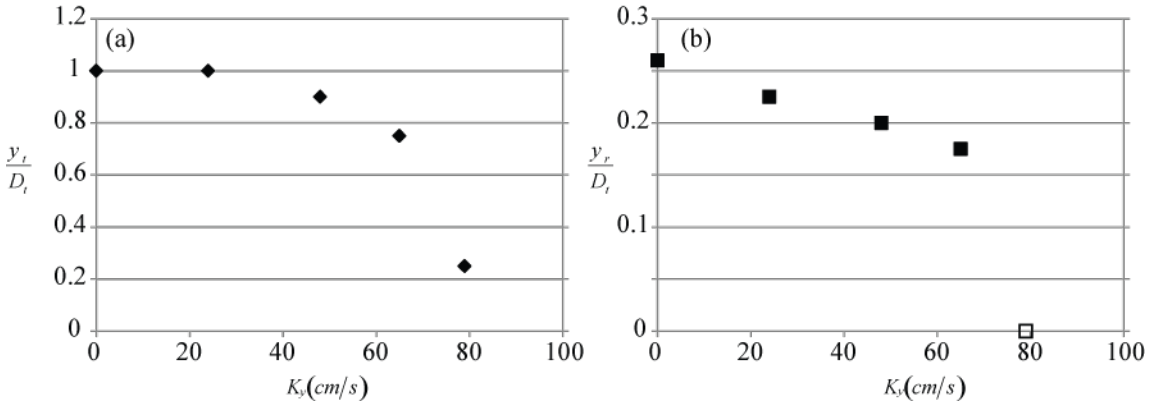

Figure 2.6. Characteristic heights related to (a) the height at which the diameter of the initial ring started stretching and (b) the maximum height reached during the primary vortex rebound.

In order to reconcile the differences in behaviour of the vortex ring-boundary interaction, we examine the velocity and vorticity fields for each case in Figure 2.7. Time frames used to compare all scenarios are defined at particular instants during the interaction process: at $\tilde{t}_1 \approx 0.90$ the ring is at its closest initial approach to the boundary in K24, K48 and K65 boundaries, $\tilde{t}_2 \approx 1.15$ marks the time at which the diameter is maxmium for the K0 scenario, and $\tilde{t}_3 \approx 1.25$ is the maximum rebound height in the K0 case. This figure shows how the secondary vortex ring is clearly formed when the primary vortex ring interacts with a solid boundary. As has already been described, the secondary ring is formed with the detachment of the boundary layer and causes the decrease on the diameter of the primary vortex ring. From Figure 2.5 (c) all scenarios except K79 presented a decrease in diameter and thus a formation of the secondary vortex ring. However, Figure 2.7 (e) shows a weak presence of secondary vorticity in the K79 scenario, which may indicate why the primary ring in this case increases its diameter up to a certain point when a secondary vortex ring is formed (around $\tilde{t} \approx 1$). Lower permeable boundaries show a secondary ring more coherent in the shape and with longer life. As described before, the formation of this secondary ring is due to the development of the boundary layer. Beavers & Joseph (1967), Taylor (1971) and Richardson (1971) suggest that the boundary layer penetrates

into the porous media. Hence the weak formation of the secondary vortex ring is clearly explained by increment in the extension onto the foam material with porosity, affecting the boundary layer. This makes more difficult the detachment of the boundary layer and consequently the formation of this secondary vortex ring.

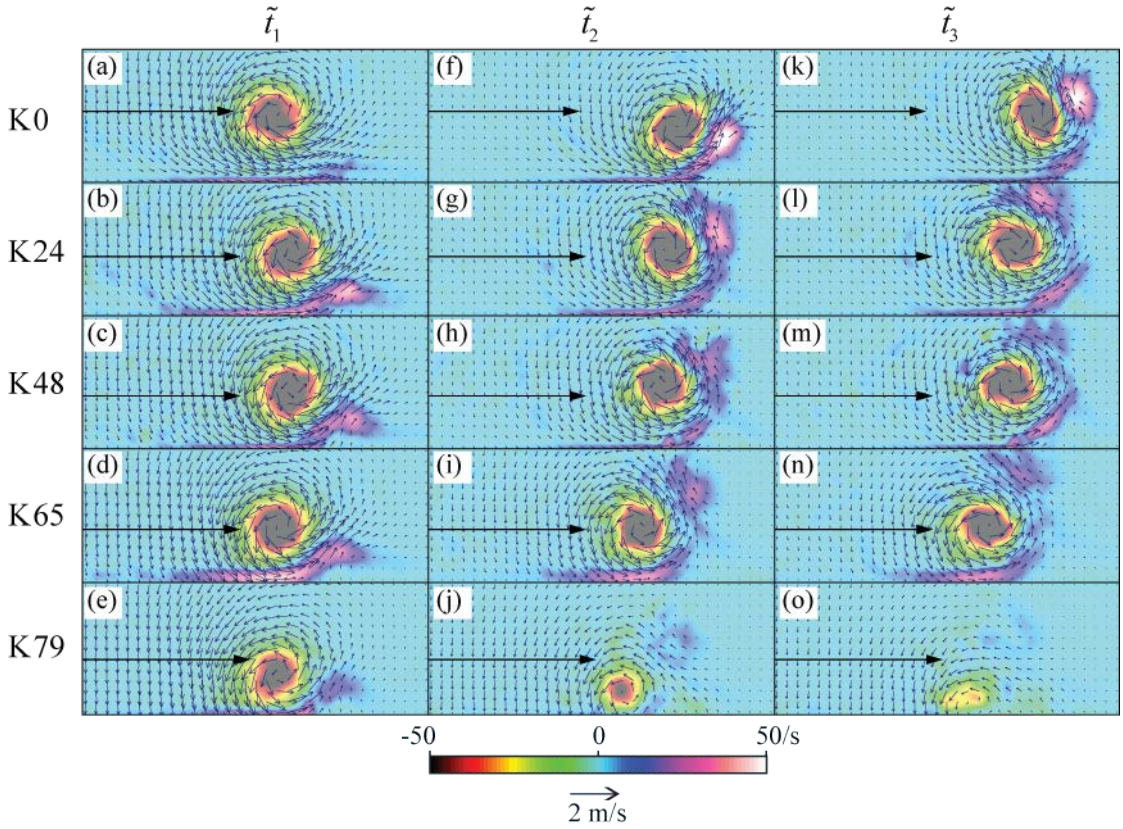

Figure 2.7. PIV results of half vortex ring at the time steps $\tilde{t}_1 = 0.92, \tilde{t}_2 = 1.12, \tilde{t}_3 = 1.24$ Background variable vorticity.

Figure 2.7 (f) is useful to see how the maximum diameter of the primary ring is reached when the secondary vortex ring is at the same elevation as the primary vortex; Figure 2.7 g-i may confirm this since $\tilde{t}_2$ in the K24, K48 and K65 cases is right after the maximum diameter instant (see Figure 2.5 (c)) and the secondary vortex ring is located slightly above the primary ring. The maximum rebound height, defined as $\tilde{t}_3$ in the K0 scenario presents the location of the secondary vortex ring at an angle ~45º. This instant, $\tilde{t}_3$, in the solid boundary scenario coincides with $\tilde{t}_2$ in the K24 porous boundary, shown in Figure 2.7 (g), however this affirmation demands further research. The coarsest scenario, K79, does not show the complete evolution of the secondary vorticity because the ring seems to penetrate into the foam. Finally a third vortex ring is formed in al scenarios, Naaktgeboren et al. (2012), except the K79 case which can be observed in Figure 2.7 k-n.

One variable of interest to emphasize the changes on the vortex ring interaction with different permeable boundaries is the evolution of the vortex ring circulation,

$$\Gamma = \int_{A_c} \omega dA, \tag{2.4}$$

where A_c is the area of the core. As detailed in Bethke (2008), the definition of the core is somewhat controversial. Here, vorticity lying below 3% of the vorticity peak is considered noise and not used in the computation. Maximum vorticity peak is reached at the centre of the ring's core, and turns out to be a negative value. Therefore primary circulation is computed as sum of the negative values below the defined threshold and the secondary vorticity as the sum of positive values above the absolute value of the same threshold. This is accurate for the primary vortex ring but may underestimate the circulation of secondary and boundary layer vorticity. However it will be considered sufficient enough to reveal the real evolution of the circulation of the secondary vortex once the ring has started its rebound. During the approach to the wall the secondary circulation comes from the boundary layer; after it has reached the wall and at the early stages of the secondary vortex formation, secondary circulation from the boundary layer still represents the majority of the secondary vorticity. However after $t > 1$ circulation of the secondary vorticity comes from the secondary vortex.

Figure 2.8 plots the results of the non-dimensional circulation, $\tilde{\Gamma} = \Gamma / (V_r D_t)$ for both the primary and secondary vorticity. Primary circulation decreases with permeability particularly at higher time steps; lower results in the K79 case are mainly due to small errors accumulated on the computation of V_r. No pattern is followed between secondary circulation and the permeability, and the curves are strongly influenced by the computation of the interface level, $\tilde{Y} = 0$, which is affected by the light reflections on the foams at the interface,. When the ring is impinging a solid boundary, secondary vorticity appears due to the viscosity and the no slip boundary condition. Hence secondary vorticity starts increasing while the primary vortex ring approaches the wall because the boundary layer at the wall starts developing; this is why the secondary vorticity starts increasing before the decrease in primary circulation. However, when the ring gets to its closer position to the wall, both the primary and secondary vorticity interact. From this point, primary circulation decreases while the secondary ring is being formed by the detachment of the secondary vorticity present in the boundary layer. In the K0 scenario, circulation of the secondary vorticity has its peak coinciding with the peak on diameter evolution of the ring. As shown in Figure 2.7 the formation of this secondary vortex ring is directly related

to permeability: it is formed previously in the K79 scenario, which is the first curve to reach the peak in Figure 2.8 (b). The two coarser foams, K79 and K65, present a maximum in the secondary circulation whereas the other three cases, K48, K24 and K0 show an inflectional point beyond which secondary circulation is maintained almost constant. This is explained by the life of the secondary vortex ring: it increases as permeability decreases. Finally Figure 2.8 (b) confirms that there is a formation of the secondary vortex ring in the K79 scenario which was detected in Figure 2.7.

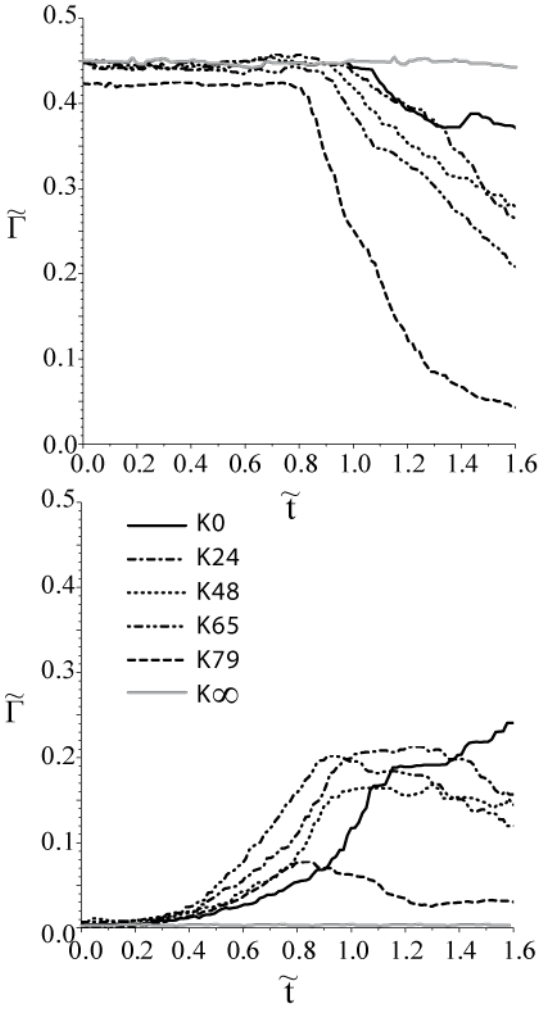

Figure 2.8. Evolution of the primary (a) and secondary (b) vorticity of the interaction of a vortex ring with different boundaries.

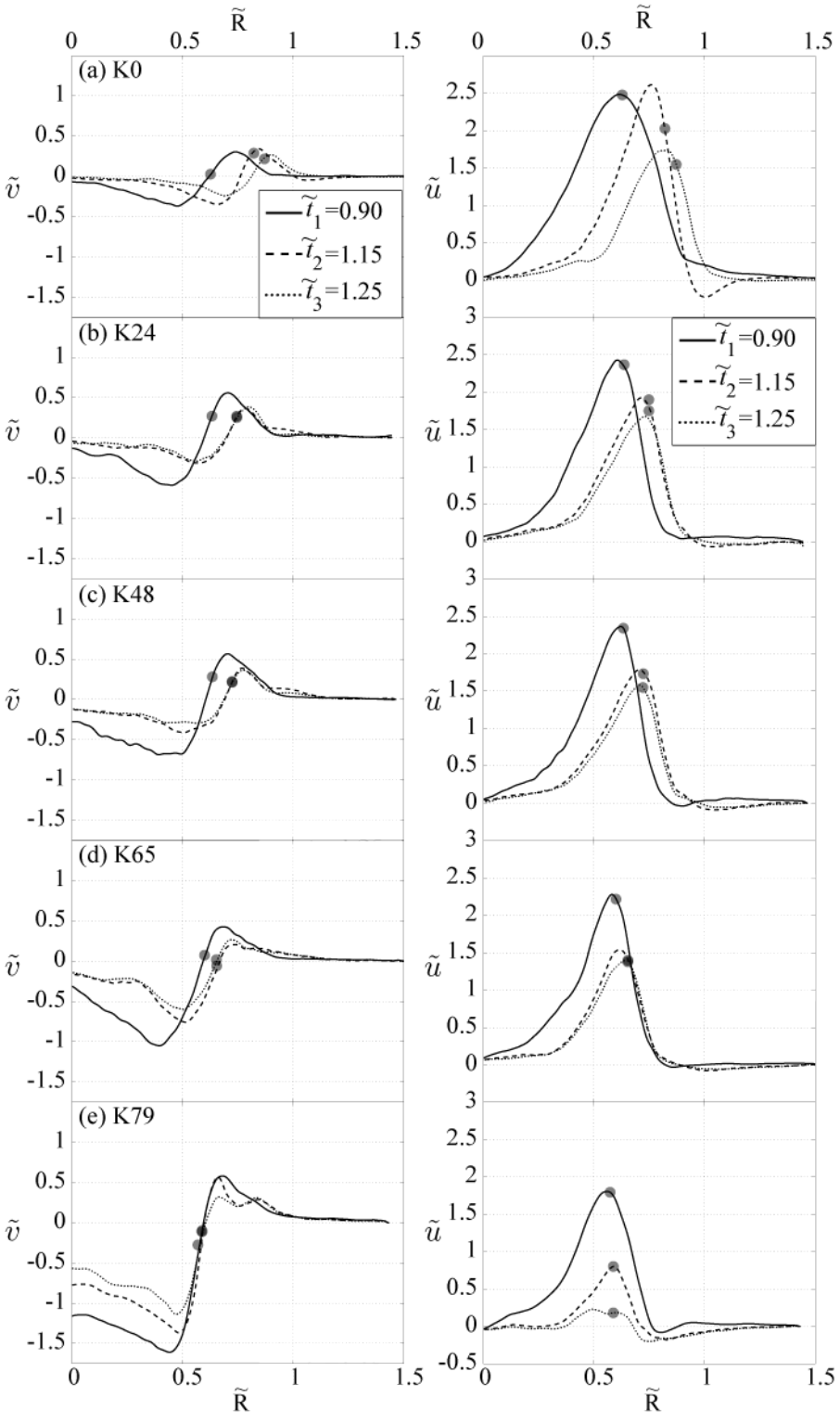

Figure 2.9. Left column: vertical velocity profiles; right column: horizontal velocity profiles. Results obtained from the PIV velocity fields 1mm above the boundary limit at the same instants as Figure 2.7. Marks define the position of the centre of the core at each time.

Figure 2.9 shows the vertical, left panel, and the horizontal, right panel, dimensionless velocity profiles ($\tilde{v} = v/V_r$) measured 1 mm above the permeable or solid boundary. The radius

has been made dimensionless by $\tilde{R} = {}^{R}/_{D_t}$. The marks represent the position of the core at each time and the time profiles coincide with the frames plotted in Figure 2.7. In absolute terms vertical velocities close to the boundary increase with permeability whereas horizontal velocities decrease with *k*. Both maximum horizontal and vertical velocities are reached at t_1 except for the K0 and the K79 case. In the first scenario, K0, this is because the ring has not get to its closest position from the boundary whereas in the most permeable foam, K79, maximum velocities are obtained at the inflectional point in the curve showed at Figure 2.5(b). Regarding the position of the core with respect to velocity peaks two behaviours are observed in Figure 2.9. The first one is that the core is located between positive and negative vertical velocity peaks but always closer to the positive peak. Besides de vertical velocities below the core are generally positive having an influence on slowing down the core, with the exception of the most permeable foam, K79, where the velocity in the bed located right below the core is negative. The second behaviour detected in the right panel of Figure 2.9 is that opposite to the vertical velocity profiles, the bed horizontal velocity peak is located slightly closer to the axisymmetric axis than the core of the primary ring, particularly in the solid boundary scenario, K0. This is caused by the no-slip boundary condition present in the solid boundary case but may be further discussed for the permeable cases by comparing the evolution of the horizontal velocity peaks.

Figure 2.10 plots this maximum as a function of time, following Bethke & Dalziel (2012), specifically

$$\tilde{u}_m(t) = \max_r \tilde{u}(y, r, t), \qquad (2.5)$$

where the same criteria of bed velocity defined at a height $z = 1mm$. Bethke & Dalziel (2012) found a clear diversion of the solid boundary curve from the inviscid theoretical curve. Moreover they reported that the same curve for a sediment bed layer did match perfectly with the inviscid plot showing that this latter scenario presented a free-slip boundary condition. However in Figure 2.10 permeable boundaries do not differ from the solid boundary curve mainly because the measurements are made 1 mm above the bed whereas Bethke & Dalziel (2012) measured at 0.5mm. Assuming the diffusion of vorticity over a time as D/V_r then a good approximation to the boundary layer thickness in the K0 case is $\delta \approx (\nu D_t / V_r)^{1/2}$ which yields to a 0.5mm value. This explains the apparent phenomenon of the no-slip boundary condition in our permeable experiments. The use of $y = 0.5mm$ was not feasible due to the nature of the foam.

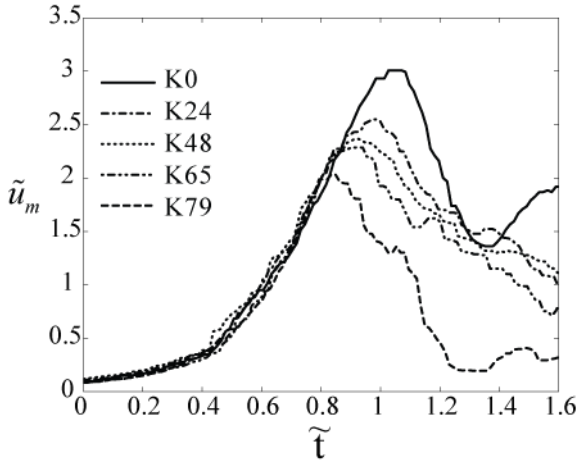

Figure 2.10. Non dimensional maximum horizontal bed velocity evolution on dimensionless time

Table 2.2. Time occurrence when maximum horizontal bed velocity reaches its peak, Figure 2.10.

	K0	**K24**	**K48**	**K65**	**K79**
$\tilde{t}, \tilde{u}_m(max)$	1.07	0.96	0.91	0.89	0.85

In Figure 2.10 time evolution of this maximum horizontal bed velocity is the same for all experiments at early stages of the vortex ring motion. However, when the coarsest scenario, K79, reaches its maximum $\tilde{u}_m$ at $\tilde{t} \approx 0.85$ it decreases and diverges from the general trend of the curve. Subsequently, lower permeable boundaries suffer the same phenomenon at the time frames detailed in Table 2.2. This peak takes place later when permeability decreases and at higher horizontal velocities and coincides approximately with the frame at which the ring reaches its minimum height and secondary vorticity starts detaching from the boundary. In the K79 case, however, since there is no minimum height the peak coincides in time with the inflectional point shown in Figure 2.5 (b).The important role played by the permeability differences can also be accounted with the existence of fluid exchange between the ambient and the porous boundary. Since the measurements are 2D, the total flux exchanged is computed in the observed area, being representative of all the volume due to the axisymmetry of the experiment. The positive flux, q^+, is defined as the flow coming out of the foam- $v^+ = v > 0$ -,

$$q^+(t) = \Delta r \sum_{R_i} v(y, r_i, t) r_i \quad \forall r_i, v > 0 . \tag{2.6}$$

Similarly, the negative flux –ambient fluid getting inside the porous boundary- is defined using the same terms for negative velocity points - $v^- = v > 0$ -,

$$q^{-}(t) = \Delta r \sum_{r_i} v(y, r_i, t) r_i \quad \forall r_i, v < 0 . \tag{2.7}$$

Therefore the total flux exchanged is the sum of Eq. (2.6) and Eq. (2.7),

$$q(t) = q^{+}(t) + q^{-}(t) . \tag{2.8}$$

Both positive and negative velocities should be determined at $\tilde{Y} = 0$. However, due to limitations inherent in the PIV measurements, we employ velocities measured at $\tilde{Y} = 0.02$ as a reasonable estimate of that at the boundary when calculating the fluxes. This height is equivalent to 1mm above each boundary. A similar calculation was performed by Bethke & Dalziel (2012), but there it proved possible to base measurements on the velocity 0.5mm above the boundary. The nature of the foam boundaries in the present case precluded such a low height in the current investigation.

Assuming there is no flux exchange beyond the limits of the field of view, and that the foam may be considered rigid, we expect no net exchange between the foam and ambient fluid, and thus anticipate $q(t) = 0$.

Figure 2.11(a) shows the flux calculated using Eq. (2.6) and Figure 2.11(b) plots the total flux exchanged between the ambient fluid and the boundary computed using Eq.(2.8), both in dimensionless form, $\tilde{q} = q \big/ \left(\pi D_t^2 V_r \right)$. The net exchange for the solid boundary K0 was also computed to determine an order of magnitude estimate of the inherent error in the PIV interrogation process. In general, the total flux computed for the K0 case, Figure 2.11(a), is negative when the ring is approaching the boundary and starts oscillating reaching to a maximum value when the positive velocity peaks as well, Figure 2.11(b). The dimensionless mean estimative error during the whole experiment is in the order of 10^{-4}. The maximum positive flux in all scenarios coincides with the primary vortex ring at its closest height from the boundary (except for K79 that it occurs when the ring clearly decelerates). However the maximum total flux is slightly retarded with the maximum positive error, taking place at the highest diameter instant. In Figure 2.11 (b) two different behaviors are detected: i) for the coarsest foams, K79 and K65, the total flux exchanged is mostly negative whereas ii) for the finest foams K48 and K24 is smaller and positive particularly in K24. Predominantly, in Figure 2.11 conservation of mass appears not to be satisfied in any experiment at any time and is always higher than the K0 case.

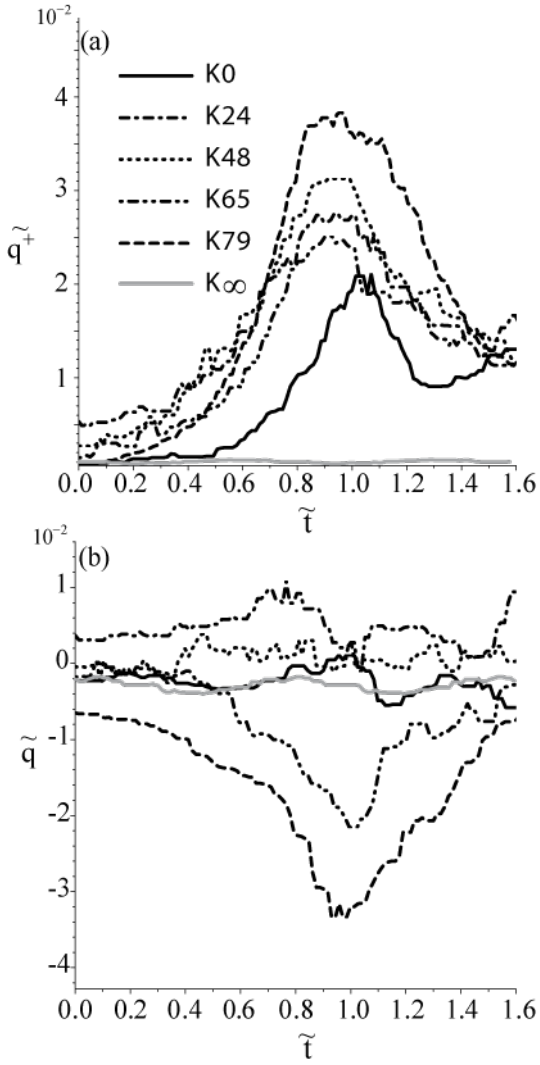

Figure 2.11. Temporal evolution of the dimensionless flux exchange between the ambient fluid and the boundary.

There are four possible causes for the errors found in the instantaneous conservation of mass: i) the flow exiting the foam is three-dimensional with azimuthal variations not captured by the current methods; ii) slower particles create brighter images near the bottom and the PIV may be biased towards them; iii) the foam filters some of the particles from the flow so that there are many fewer particles in the upward flow (contributing to q^+) creating a bias in the measurements, iv) the limited resolution of the PIV processing that effectively smooths any localised fast-moving jets issuing from the individual pores. The first of these possibilities affects mainly the coarser foams due to higher velocities and larger pore diameter, introducing a larger 3D effect; on the other hand, the second reason might explain the effects found on the solid boundary, and the finer foams. The third reason is related to higher velocities present in coarser foams therefore, incoming velocities (which are higher in the most permeable boundaries) make the

particles lying at the surface of the foam be exhausted sooner. Regardless of the higher positive velocities present in coarser foams as well, this flux may have been in the foam for a while and so is likely to have deposited its particles. Assuming the third error type is the dominant effect, positive net flux is corrected by modifying positive velocities coming out of the foam at a height $z = 1mm$.

In order to satisfy continuity and assuming the measurements of flow out of the foam have been underestimated, we introduce a correction to positive velocities. This is done by considering equal the corrected positive flux and the negative flux obtained previously,

$$\hat{q}^{+}(t) + q^{-}(t) = 0 \tag{2.9}$$

And will be performed using two different corrections:

1) A linear correction for all positive velocities

$$\hat{v}_1^{+}(y, r_i, t) = \beta_1(t) v^{+}(y, r_i, t), \tag{2.10}$$

where $\beta_1(t)$ is the correction factor defined by

$$\beta_1(t) = \frac{-q^{-}(t)}{q^{+}(t)} \tag{2.11}$$

2) A correction inversely proportional to the radius

$$\hat{v}_2^{+}(y, r_i, t) = \frac{\beta_2(t)}{r_i} v^{+}(y, r_i, t), \tag{2.12}$$

being $\beta_2(t)$ is the correction factor for this option and found after imposing the mass balance from Eq. (2.9),

$$\beta_2(t) = \frac{-q^{-}(t)}{\Delta r \sum_{r_i} v^{+}(y, r_i, t)} \tag{2.13}$$

The second option is interesting since it ensures $v \to 0$ as $r \to \infty$, but it also enlarges velocities closer to the symmetry axis more than positive velocities far from it. The first option distributes equally the correction along the positive velocity radius locations. Figure 2.12 shows the results obtained with both correction options. Differences are more visible in the K79 case since it is the scenario with larger flux exchange and where errors can be higher due to the

structure of the pores. The uniform correction shows smaller kinks in the peak velocities than the second correction inversely proportional to the radius. This is extensible to all scenarios but less visible. On the other hand, small differences are seen at the queue of the vertical velocity profiles regardless of the correction used, which invalidates, somehow, the second option to correct positive velocities.

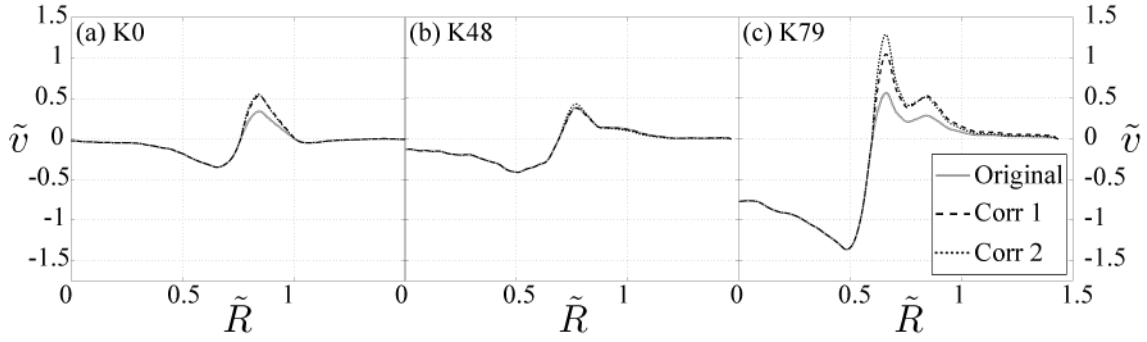

Figure 2.12. Corrections applied to positive velocity results in the K0, K48 and K79 scenarios. Grey continuous line represents the original velocity profiles, dashed lines are positive velocities after applying Eq. (10) and dotted lines represent the second correction option to positive velocities, Eq. (12).

2.4 Discussion

2.4.1 Experimental results

The experiments reported in the last section confirm what has already been published by other authors for a ring impacting on a solid boundary, namely: i) the ring starts stretching after it reaches a height comparable to its initial diameter (Figure 2.5 (a) and (c)); ii) once the ring gets close to the solid wall, the secondary vorticity induced in the boundary layer separates from the wall to create a secondary vortex with opposite vorticity sign that leads to the primary vortex rebounding from the wall; and iii) the motion induced by the secondary vortex causes a decrease in diameter of the primary ring causing its trajectory to loop, as shown in Figure 2.5 (a). When permeable boundaries are used, all three of these phenomena are reduced as permeability increases. In particular, in the largest permeable foam, K79, the ring does not rebound but dissipate or enter inside the foam. This is confirmed by looking at the flux of primary vorticity across $z = 1mm$ computed as

$$q_\Omega = \Delta r \sum_{R_i} \Omega\left(y, r_i, t\right) r_i \quad \Omega > 0.03\Omega_{\max}\,, \tag{2.14}$$

and made dimensionless $\tilde{q}_\Omega = q_\Omega D_t / V_r$. The results obtained for the K79 case are shown in Figure 2.13 where a clear change is visible after $\tilde{t} > 0.8$ which coincides with the frame after

which the primary vorticity starts decreasing in Figure 2.8(a). It also explains why the primary vorticity in the K79 permeable boundary decreases faster than the other scenarios: because the primary ring seems to enter inside the foam. This does not occur with the other cases as seen in Figure 2.7.

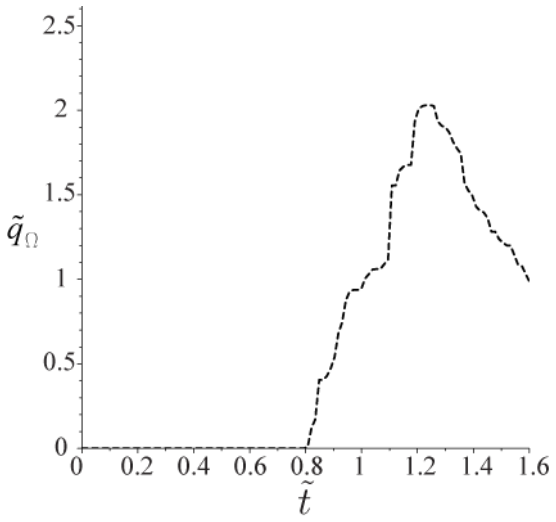

Figure 2.13. Flux of primary vorticity through the K79 porous media, measured at *z=1mm*.

The permeable boundary results shown in this study are contrasted with two similar situations: bed sediments and thin porous grids. When comparing two different sediment bed layers (with different particle diameter and permeability), Bethke & Dalziel (2012) found that the trajectory followed by the vortex ring core was not affected by the bed permeability, although they report a weak exchange with the bed and an enhancement in the velocity immediately above the bed. The first of these observations contrasts with what we see here in Figure 2.5. The principal reason behind this difference is that the permeability of their porous media ($k < 9.4\times10^{-10}$ m^2) was between two and four orders of magnitude smaller than for the foams presented here, and consequently the flow into and out of the porous media was very much smaller and so had no measureable impact on the propagation of the ring. Also the difference in approach distance would not have been measurable for such low permeabilities. To a good approximation, their porous boundaries were indistinguishable from solid boundaries except for the dynamics of the boundary layer that formed on it. However, with the substantially larger permeabilities used here we see that the permeability has a clear influence on the vortex ring diameter expansion, the rebound and the minimum height reached close to the boundary.

The evolution of the ring towards permeable boundaries is very similar to that of a vortex ring impinging a thin porous grid (e.g. Adhikari & Lim (2009), Hrynuk et al. (2012), and Naaktgeboren et al. (2012)). Experimental setups differ with the research presented herein

essentially at the position of the boundary and its thicnkess: they used very thin grids located far from the solid boundary, and the grid did not cover the entire plan form of the tank. Therefore the flux beyond the limit of the porous screen is substantially different from the flux inside thicker porous boundaries as the ones used in our experiments.

To a good approximation, all pores are connected and permeability is proportional to porosity. Therefore, the behavior of the vortex ring motion towards different permeable boundaries is comparable to the results obtained when a thin wire mesh is used. In the wire mesh experiments, the decrease in vortex stretching and the changes in secondary vorticity formation are explained to be due to the loss of circulation of the primary ring, a feature also seen in Figure 2.8. According to Adhikari & Lim (2009) this is caused by the self-induced flow around the axis of symmetry that forms a jet-like flow beyond the mesh. In Naaktgeboren et al. (2012) the decrease impulse with more porous grids, as a reflection of the drag force exerted on the flow by the screen, was said to cause the reduction of the secondary vorticity and subsequent rebound. However, neither of these investigations take into account the either the penetration of the boundary layer inside the porous media or the flux exchange between the downstream and upstream sides of the mesh.

Recalling that one of the main differences between our experiments and the thin grid research already published is that their screen does not cover the whole plan form of the tank, the flux exchange between both sides of the grid is clearly influenced by this. From Figure 2.9, peak velocities detected in the permeable boundaries increase with permeability. Therefore the velocity coming out of the foam is higher in the coarsest case, K78, constraining the diameter of the ring and preventing the stretching. Combining both results, the lack of stretching when porosity/permeability increases is due to the smaller decrease in the self-induced flow near the axis of symmetry and the subsequent increase in flux exiting of the foam. The flux of primary vorticity along the interface was only detected in the K79 case and so it may not be the primary cause of the primary vortex ring stretching.

The no slip condition, satisfied in the solid boundary scenario and linked to the formation of the secondary vorticity, is found to disappear as permeability increases. This is consistent with the results from Naaktgeboren et al. (2012) which relate the suppression of the secondary vorticity to the decrease in hydraulic impulse at higher permeable grids. Bethke & Dalziel (2012) suggested the explanation for the apparent slip condition at the surface of a 1000 μm bed sediment layer was the permeability of the layer itself. Although there is no pattern visible from the evolution of the secondary vorticity with permeability in Figure 2.8b, the decrease in primary

circulation as permeability increases shows how to no-slip boundary condition will also be affected by permeability.

Another phenomenon associated with different permeable beds is related to the boundary layer formed at the interface. As it has already been noticed in the previous section and according to Bethke & Dalziel (2012), the maximum bed velocity for ring impinging a sediment bed layer evolves in the same way as for an inviscid vortex ring. Nevertheless, the boundary layer is still present, as witnessed by the boundary layer separation that occurs even when the K79 foam is used. Yet they denote a thinning effect while the permeability increases that is slightly perceptible in Figure 2.7, though the small differences between scenarios might also be due to the errors induced by the PIV. However, the detachment of such boundary layer with the consequent formation of the secondary vortex ring differs from one scenario to the other. As suggested in Figure 2.10, the maximum of the peak velocity bed is reached earlier for higher K values and coincides with the detachment of the primary ring and the formation of the secondary vortex ring. The coherence of this secondary vortex formed right after the ring reaches its minimum height is lost due to two factors: the flux exchange and the extension of the boundary layer into the porous material found by Beavers & Joseph (1967). When a more permeable boundary is used, the boundary layer reaches deeper positions and so higher stresses are needed to permit the entire detachment. This, added to the fact that the K79 boundary has a lower maximum bed velocity peak compared to less permeable scenarios, explains the poor coherent second vortex ring formed while approaching a high permeable boundary, as shown in Figure 2.7.

2.4.2 Numerical model approach

Research published in vortex rings impinging thin porous grids focuses on the evolution of the ring downstream the mesh. In general terms, an increase in permeability allows the vortex to continue downwards with almost the same structure of a vortex ring. However, Hrynuk et al. (2012) also accounts for the influence on the diameter of the wire.

Naaktgeboren et al. (2012) concluded that the vortices would not survive in a thicker porous media. This section describes a simple model used to study the propagation of the ring inside the porous boundary.

The flow of an incompressible fluid through a porous media is governed by Darcy's law,

$$\vec{q} = \frac{-\underline{\underline{k}}}{\mu} \nabla P, \qquad (2.15)$$

being q the flow per unit area, $\underline{k}$ the permeability tensor, μμ the dynamic viscosity of the fluid and P the non-hydrostatic component of the pressure (measured in Pa). This equation assumes irrotational laminar flow, $\mathrm{Re}_p < 1$, however it is typically assumed that for $\mathrm{Re}_p < 40-80$ Darcy's equation is still applicable Chilton & Colburn (1931), Zeng & Grigg (2006). Re_p is defined as the Reynolds number for flows in porous media

$$\mathrm{Re}_p = \frac{D_p \hat{v}}{\nu}, \tag{2.16}$$

with D_p the pore diameter and $\hat{v}$ the mean flow velocity entering into the foam. The mean velocity flow is obtained using the first option of positive velocities correction and the variable used to compute the Reynolds number is the maximum in time of the mean velocity flow measured at *y=1mm*

$$\hat{v} = \max_t \left(\frac{1}{N} \sum_{i=0}^{N} \left(v^{-}\left(y, r_i, t\right) + v_1^{+}\left(y, r_i, t\right) \right) \right). \tag{2.17}$$

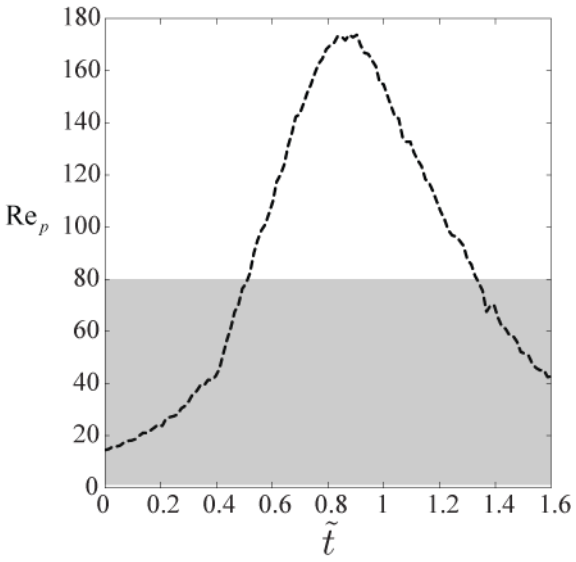

Figure 2.14. Evolution of the Reynolds number for the flow in the K79 permeable boundary. Shadow area shows the zone where Darcy's equation can be used.

Results shown in Table 2.1 indicate that K24 and K48 foams are in the range of flow considered Darcy's flows. The K65 permeable boundary is in the threshold of applicability but will be considered as a Darcy's flow as well. However the coarsest foam, K79, does not satisfy the condition for a laminar flow inside the porous boundary, henceforth Darcy's equation cannot be applied. Nevertheless, the first and last instants of the interaction between the vortex ring and

the K79 permeable boundary are in the range of Darcy's flow, shown in Figure 2.14, and Eq. (2.15) will be used to see the evolution of the flow inside the K79 permeable boundary always bearing in mind that some instants may not be comparable with other foams.

Introducing Darcy's law into the continuity equation for an incompressible fluid in an rigid porous medium, the result is the equation of steady flow through homogeneous porous media, using hydraulic conductivity $\underline{K} = \underline{k}\, g/\nu$ and the non-hyrdostatic component of the pressure (measured in m $P = p\rho g$):

$$-\nabla\cdot\left(\underline{K}\nabla p\right) = 0\,. \tag{2.18}$$

Given that not all our reticulated foams are isotropic, see Table 2.1 column α, then $K_z \neq K_r$. Also assuming that the axisymmetric behaviour of the vortex ring is maintained beyond the boundary limit we have to work on cylindrical coordinates. A centred finite differences discretization was applied to Eq.(2.18):

$$K_r\left(\frac{1}{r}\frac{\partial p}{\partial r} + \frac{\partial^2 p}{\partial r^2}\right) + K_y\frac{\partial^2 p}{\partial y^2} = 0\,. \tag{2.19}$$

For the isotropic foams, K24 and K48, $K_y = K_r$ and the hydraulic conductivity disappears from Eq. (2.19).

The domain modeled consists on 2D scheme representing a δθ fraction of the entire ring. Therefore, one lateral boundary condition coincides with the symmetry axes and zero radial flux is imposed. The same boundary condition is imposed at the opposite wall because, according to the initial hypotheses, no influence of the ring is seen beyond that point. The lower boundary condition is impermeable in the vertical direction due to the presence of the bottom of the Perspex box. The upper boundary condition is the vertical velocity obtained at a height of 1 mm above the boundary, Figure 2.9, under the assumption that this is close enough to represent the flow per unit area entering the porous foam using Eq. (2.10) and Eq. (2.11) to correct positive fluxes in order to satisfy continuity. Hence, the upper boundary condition is the one imposing the temporal variation and the scheme is considered quasi-steady.

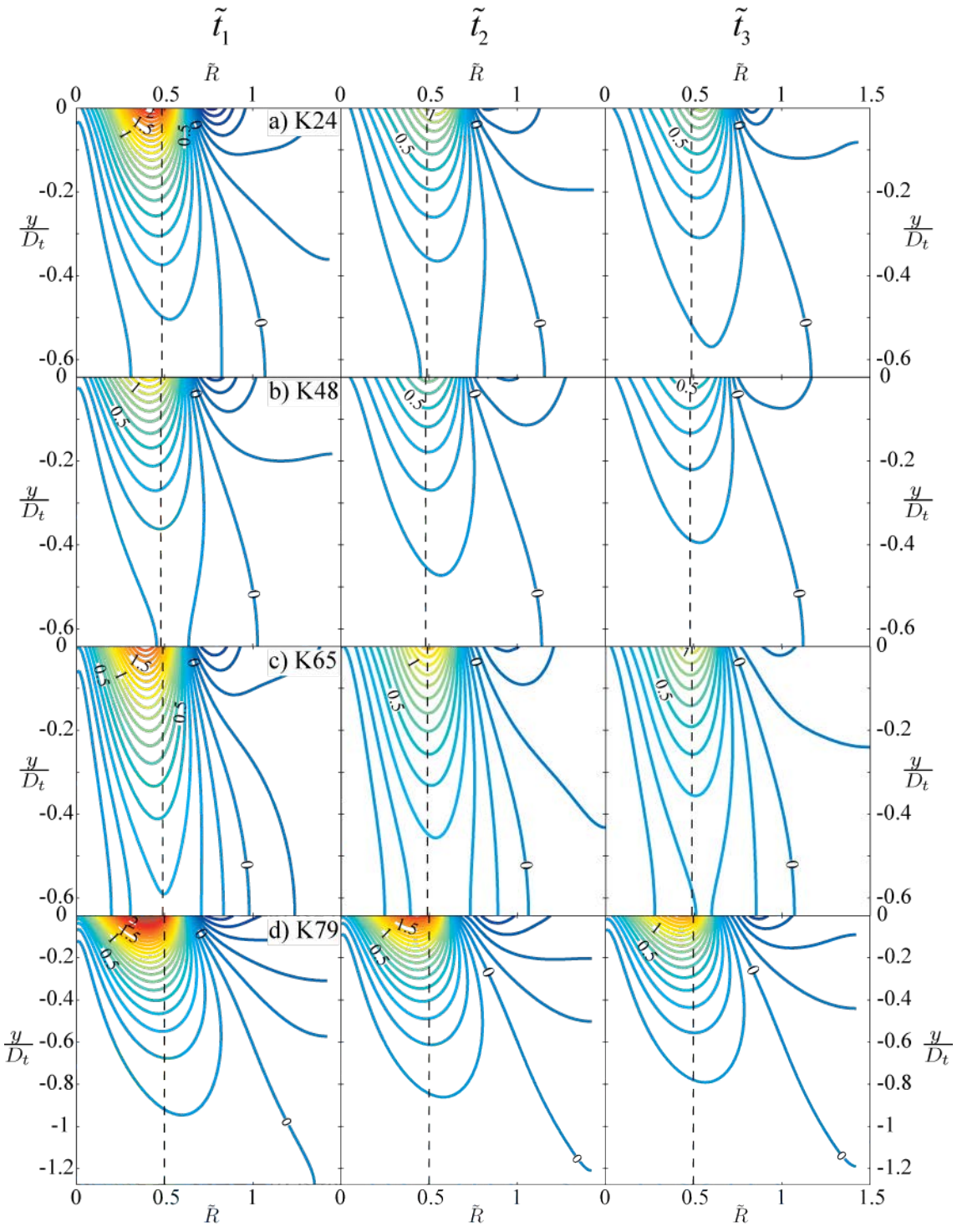

Figure 2.15. Pressure lines obtained from the finite difference model at four different instants –the same used in Figure 2.7-. Energy lines are plotted every 0.1 mm. Dashed lines mark the position of the core.

Figure 2.15 shows the pressure contours (mm) obtained with the finite differences model already described above, along with the position of the vortex ring's core (dashed vertical black lines). Zero of the vertical axis coincides with the interface between permeable material and water ambient and is made dimensionless using the diameter of the ring before starting

stretching; the aspect ratio in the K79 case changes because the foam used in the experiments is twice thicker than the other three permeable boundaries, K24, K48 and K65 (see Table 2.2). Times used to plot Figure 2.15 are the same used in Figure 2.7 and Figure 2.9 being $\tilde{t}_1 = 0.9$, left panel, the instant where the primary ring reaches the closest position from the boundary in the K24, K48 and K65 cases; $\tilde{t}_2 = 1.15$, middle panel, when the ring impinging a solid boundary gets to the maximum diameter, which coincides with the maximum rebound position for the K24 and K48 scenarios, Figure 2.5; and finally $\tilde{t}_3 = 1.25$, right panel, is the maximum rebound case in the K0 scenario. The influence of the option chosen to correct positive vertical velocities was considered negligible.

The primary vortex ring in the coarsest foam, K79, does not propagate beyond the interface between materials, as suggested by Naaktgeboren et al. (2012), and shown in Figure 2.15(d). This is controversial since the Re is too large for this scenario to let the flux inside the foam satisfy Darcy's equation and as shown before, primary vorticity flux in the K79 penetrates into the foam and motion becomes rotational. Nevertheless, it is easy to see that the vortex ring might survive beyond the interface for larger Re and higher diameter pores.

The largest pressure instants take place when the ring reaches its position closer to the boundary because of higher vertical velocities, Figure 2.9 (left column). However, although absolute vertical velocities increase with permeability, being lower for the K24 scenario and higher for the K79 foam, results shown in Figure 2.15 seem not to concord. The correction option for positive velocities, does not influence substantially the results obtained and so it is discarded as the cause of this anomaly. Therefore the significant differences seen in the K24 foam may be because the maximum pressure gradients are proportional to the ratio between maximum vertical velocities and hydraulic conductivity tensor, $\nabla p \approx v_{\max} / \underline{K}$. The indicated ratio decreases with permeability except for the K24 scenario where it has a larger value than the K79 foam. However results differing in the K24 foam from the rest of the permeable boundaries may also indicate that the coarsest foams (K48, K65 and K79) do not satisfy Darcy's equation having turbulent flow inside the porous foam.

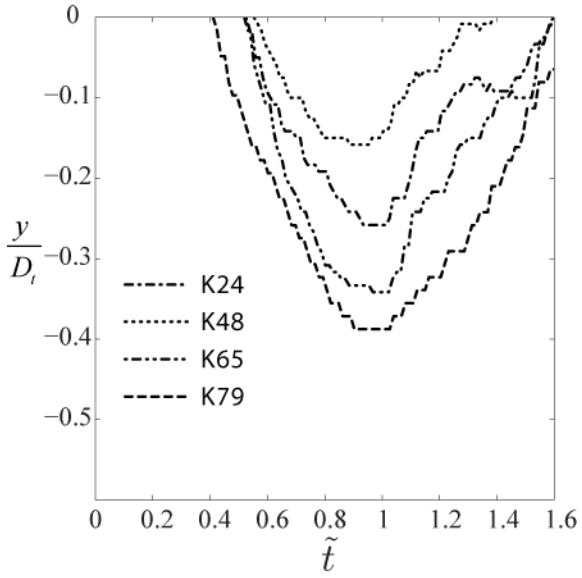

Figure 2.16. **Evolution of the maximum depth beyond which the energy is higher than 0.5mm.**

An interesting variable to look at from the numerical simulations is the depth influence of the ring over time at each case. Figure 2.16 shows the temporal evolution of the depth beyond which the energy is higher than 0.5mm. It is important to recall that the thickness of the foam used for the K79 case is twice the thickness of the rest of the foams and the figure shows how the thickness does not influence the results, since the line of K79 has the same order of magnitude as in the other foams.

2.5 Summary

This chapter has presented experimental measures of a vortex ring impinging four different permeable boundaries and a solid boundary.

Two different experimental techniques were used: tin chloride electrolysis and PIV. The first one was performed earlier in time than the last one to explore the main differences on the interaction of the vortex ring with different permeabilities. The second technique was used to study with higher detail the characteristics already detected.

Three main effects on the evolution of the vortex ring were found when the solid boundary was switched to a low permeable boundary. They also evolved when permeability was increased:

- Vortex stretching was proportional to the permeability. This means that the diameter of the primary ring increased later and with lower magnitudes when larger permeable boundaries were used.

- The deceleration of the ring started earlier and further from the interface when permeability values were smaller.
- Secondary vorticity was stronger and had a longer life with the solid and lower permeable boundaries.

Characteristics of the boundary layer formed at the interface were also studied to see whether the primary ring in the coarsest scenario, K79, penetrated the foam. However results did not show a clear correlation between the thickness of the boundary and the permeability of the foam. This was likely due to reflections at the interface, which changed with the colour of the foam and imprecisions when defining the exact interface level.

Finally a simple numerical model was run in order to see the influences of the foam thickness used. Although the coarsest case, K79, had a Reynolds number larger than the limit permitted to use Darcy's equation in most of the time of the experiment, the model was useful to see the foams were thick enough to consider the thickness had no influence on the results shown.

Chapter 3: PIV Experiments In Rough-wall, Laminar-to-turbulent, Oscillatory Boundary-layer Flows

In this chapter the initial characterization of experiments done with oscillatory boundary layers over smooth and rough beds is analyzed. Variables needed for the definition of the flow are studied comparing different formulations proposed by previous investigations.

3.1 Introduction

Oscillatory flows represent an important class of unsteady flows found in a variety of natural physical processes. The case of wave-induced oscillatory flows, with applications in the fields of coastal and offshore engineering, such as sediment transport, submarine outfalls, drilling platforms, off-shore wind turbines and other marine energy-generating devices, is of particular environmental importance. Experimental research on oscillatory flows began in the 1950's with the seminal work of Li (1954) who investigated the stability of laminar oscillatory flows. Kamphuis (1975) proposed an oscillatory flow regime distribution and a friction-factor relationship according to the wave Reynolds number (Re_w), the sediment roughness and the boundary layer thickness (δ). Jonsson (1980) proposed a new relationship between the friction factor (f_w) and the boundary layer thickness which differed from the Kamphuis (1975) definition for very low ratios of boundary layer thickness to sediment roughness size ($A/2.5D_{50}$). He also proposed the existence of a logarithmic layer in the mean velocity profile which yielded an expression for the defect velocity law. Sleath (1987) focused on measuring the turbulence near the wall, like "jets of fluid associated with vortex formation", which, he argued, explained the discrepancies between some methodologies used to compute the friction factor. Jensen et al. (1989) expanded the research in turbulent oscillatory boundary layers with experiments at higher Reynolds numbers for both smooth and rough walls. Carstensen et al. (2010) studied the existence of coherent flow structures in oscillatory flows defining two different types –vortex tubes and isolated turbulent spots.

The particular challenges found in oscillatory boundary layers arise from the temporal variation of flow regimes and bed roughness conditions along a given cycle which introduce a high degree of complexity in the analysis of these flows. The governing equations for oscillatory flows are derived from the general Reynolds-Averaged Navier–Stokes equations for fluid motion. In the particular case of laminar flows, an exact solution for the oscillatory boundary-layer flow is obtained, known as Stokes' second problem (Lamb, 1996; Batchelor, 1967). However, no exact solution exists for the turbulent regime nor the transition between laminar and turbulent flow, yet analogies to steady boundary-layer flows have been used with some success (Jonsson, 1980). The addition of roughness at the wall further enhances the turbulent phenomena inside the boundary layer.

The general definition of the flow regime is discerned using the wave Reynolds number ($Re_w = U_{om}A/\nu$) as the defining parameter (e.g, Kamphuis, 1975; Jonsson, 1980; Sleath, 1987; Pedocchi & Garcia, 2009) where U_{om} is the maximum free-stream velocity, A is the amplitude of the oscillation and ν is the kinematic viscosity of the fluid. The flow regime definition must also account for the possibility that the flow is transitioning between laminar, laminar-to-turbulent, and fully turbulent flow conditions during a single period of oscillation. Regardless of this important time dependence, many studies typically assume the flow regime to remain constant throughout an oscillatory cycle. Likewise, variables such as the friction factor and boundary-layer thickness may also be considered as time dependent variables (e.g. Jensen et al., 1989). Similar to flow regime, these bulk variables are typically assumed to be constant and are estimated based on the characteristics of the flow at the maximum free-stream velocity phase.

Previous experimental studies of such flows have employed a variety of different measuring techniques, such as: (*i*) micropropellers (Jonsson, 1980), (*ii*) laser Doppler velocimetry (LDV) (Hino et al. 1983; Sumer, 1987; Sleath, 1987; Jensen et al., 1989; Carstensen et al., 2010) and (*iii*) hot-film probes (Hino et al., 1983; Carstensen et al., 2010). Of interest, Admiraal et al. (2006) used particle-image velocimetry (PIV) to study oscillatory flow structures over a movable sediment bed, while Carstensen et al. (2010) used high-speed cameras to visualize coherent flow structures in such flows.

Recently, Pedocchi et al. (2011) used direct numerical simulations (DNS) to study the turbulent kinetic energy (*TKE*) balance of an oscillatory boundary layer in the transition to the fully turbulent regime. Simulations were performed at $Re_w = 1.41 \times 10^6$ in the turbulent regime.

The research presented herein employs PIV to study flows transitioning from the laminar to the turbulent regime under smooth- and rough-wall conditions (D_{50} = 1.5 and 7.0 mm, respectively) for a $Re_w = 0.4\times10^4 \sim 2 \times10^4$. The PIV field of view in the streamwise–wall-normal (x–y) plane is elongated in the streamwise direction to provide more accurate spatially averaged turbulence statistics, and to effectively visualize large-scale fluid motions.

3.2 Experimental Setup

Experiments were conducted in a small U-shaped oscillatory flow water tunnel located in the Ven Te Chow Hydrosystems Laboratory at the University of Illinois at Urbana-Champaign and described by Admiraal et al. (2006). The working section of the flume is approximately 0.25 m high by 0.20 m wide and 4 m long (Figure 3.1). The top and side walls are composed of smooth transparent Perspex, and the bed is composed of a bare PVC plate. The PVC plate

remained clean of sediment for the experimental runs in the smooth-wall scenarios, whereas sediment was glued to the surface of the PVC plate under rough bed conditions. The oscillatory flow was driven by an Exlar electrical actuator moving a piston located at the right end of the flume and controlled by a computer through a National Instruments card and a custom program devised with LabView, which generates a repeatable sinusoidal motion. Cycles were recorded without stopping the actuator, but not consecutively and so they are considered independent from one-another. The sinusoidal motion was set by controlling the amplitude with an accuracy of 0.1 mm and the period with 1 μs accuracy. At the left end, a honeycomb structure was placed across the entire cross-section to avoid the influence of vortices created at the junction of the flume and the equilibrium chimney. The laser sheet measurement section was located far enough from the transition between Perspex and PVC to ensure uniform flow characteristics at each phase.

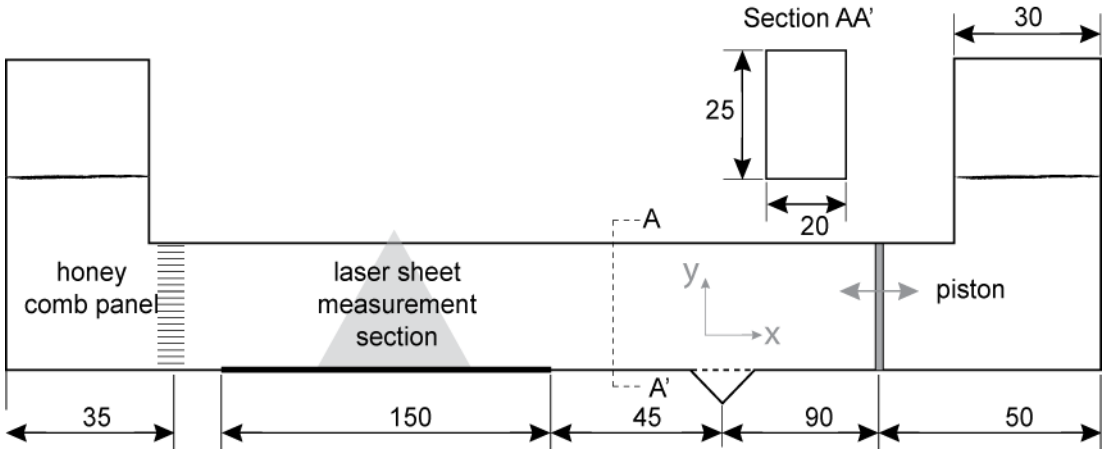

Figure 3.1. Sketch of the oscillatory tunnel, lateral view. Dimensions in cm.

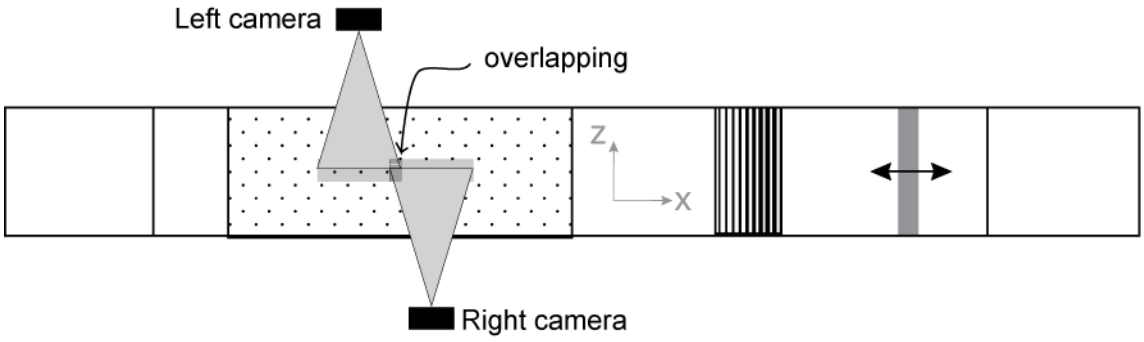

Figure 3.2. Top view sketch of the set up highlighting cameras location.

Velocity fields in the boundary layer were measured under four different Re_w conditions (Table 3.1) and three different bed configurations: smooth wall and two rough walls with different grain size distributions. The condition with the smaller bed roughness consisted of three

layers of gravel with a median diameter of D_{50} = 1.5 mm and σ = 1.3 mm, glued uniformly on a PVC plate and placed on the tunnel as a false bottom. The condition with the larger bed roughness consisted of two layers of sediment with D_{50} = 7.0 mm and σ = 1.2 mm placed on the tunnel without glue (the sediment was found to remain stationary during oscillatory flow conditions).

Table 3.1. Test conditions for the smooth and rough cases.

	Test no.	T (s)	A (mm)	U_{0m} (mm/s)	Re_w (10^4)	Δ(ωt)	δ (mm)	$A/2.D_{50}$
Smooth	1	3.3	100	188	1.86	15º	2.2	-
	2	5	100	125	1.27	10º	2.8	-
	3	1.7	45.5	171	0.77	30º	1.6	-
	4	3.3	45.5	86	0.38	15º	2.2	-
Rough (D_{50}=1.5mm)	5	3.3	100	188	1.86	15º	3.6	33
	6	5	100	125	1.27	10º	3.0	33
	7	1.7	45.5	171	0.77	30º	2.0	15
	8	3.3	45.5	86	0.38	15º	1.8	15
Rough (D_{50}=7.0mm)	9	3.3	100	188	1.86	15º	8.0	7
	10	5	100	125	1.27	10º	8.6	7
	11	1.7	45.5	171	0.77	30º	2.0	3
	12	3.3	45.5	86	0.38	15º	2.8	3

Velocities were measured at the centerline of the tunnel using a PIV system, consisting of a Gemini PIV Nd:YAG pulse laser from New Wave Research, and two 2k × 2k pixel, 12-bit frame-straddle CCD cameras from TSI Inc. The cameras were mounted to an aluminum frame and were set at a distance 55 cm from the laser light sheet measurement plane. In order to achieve a wide streamwise field of view, the two cameras were set on opposite sides of the flume and offset so that the fields of view overlapped by 6.3 mm (Figure 3.2). Camera lenses used in all experiments were AF Micro Nikon 105 mm 1:2.8D that generated a combined field of view of up to 4 cm high and 8 cm long [wall-normal (y) by streamwise (x)]. The light sheet was

conveyed to the working section through a mirror arm. Lenses used to optimize light sheet characteristics included a cylindrical lens with a focus number of 15 mm and a spherical lens of 500 mm, which obtained a laser thickness at the channel bottom of approximately 0.5 mm.

Measurements were made at a sampling rate of 7.25 Hz, which is the maximum frequency allowed by the PIV system. Thus, in every scenario, the number of phases recorded was the maximum permitted by the laser, but was proportional to one another in order to facilitate comparison. Initially, three different periods of oscillation were considered (T = 5 sec, 3 sec, 2 sec), but due to sampling frequency restrictions and to ensure at least 30º phase between samples in every experiment, the periods were adjusted accordingly to 5.007 sec, 3.338 sec and 1.669 sec. The time delay between each frame within a pair was chosen to allow a 10-pixel displacement at the maximum free-stream velocity phase. Sphericel® hollow glass spheres of 11 μm mean diameter and a density of 1.1 g/cm^3 from Potter Industries Inc. were used as tracer particles for all experiments. Also, for each experiment, 60 cycles were sampled to ensure adequate convergence of statistics (see Sleath, 1987). All test conditions analyzed for both the smooth and rough cases are summarized in Table 3.1.

After all measurements were recorded throughout all cycles for each experimental run, PIV analysis was conducted using the Insight 8 software from TSI Inc. The final interrogation window size for all experimental runs was 16 × 16 px^2 overlapped by 50% with a two-frame cross-correlation methodology, whereby local window offsets were employed based upon a first-pass interrogation with windows of 64 × 64 px^2. This protocol yielded a final vector grid spacing of 0.4 mm × 0.4 mm in each vector field. A local validation was performed between the recursive passes in order to clean initial bad vectors. Final validation was performed using 3 local median validations of different sizes, and two replacement steps for bad vectors, the last of which was performed using a smoothing window size of 3 × 3 px^2.

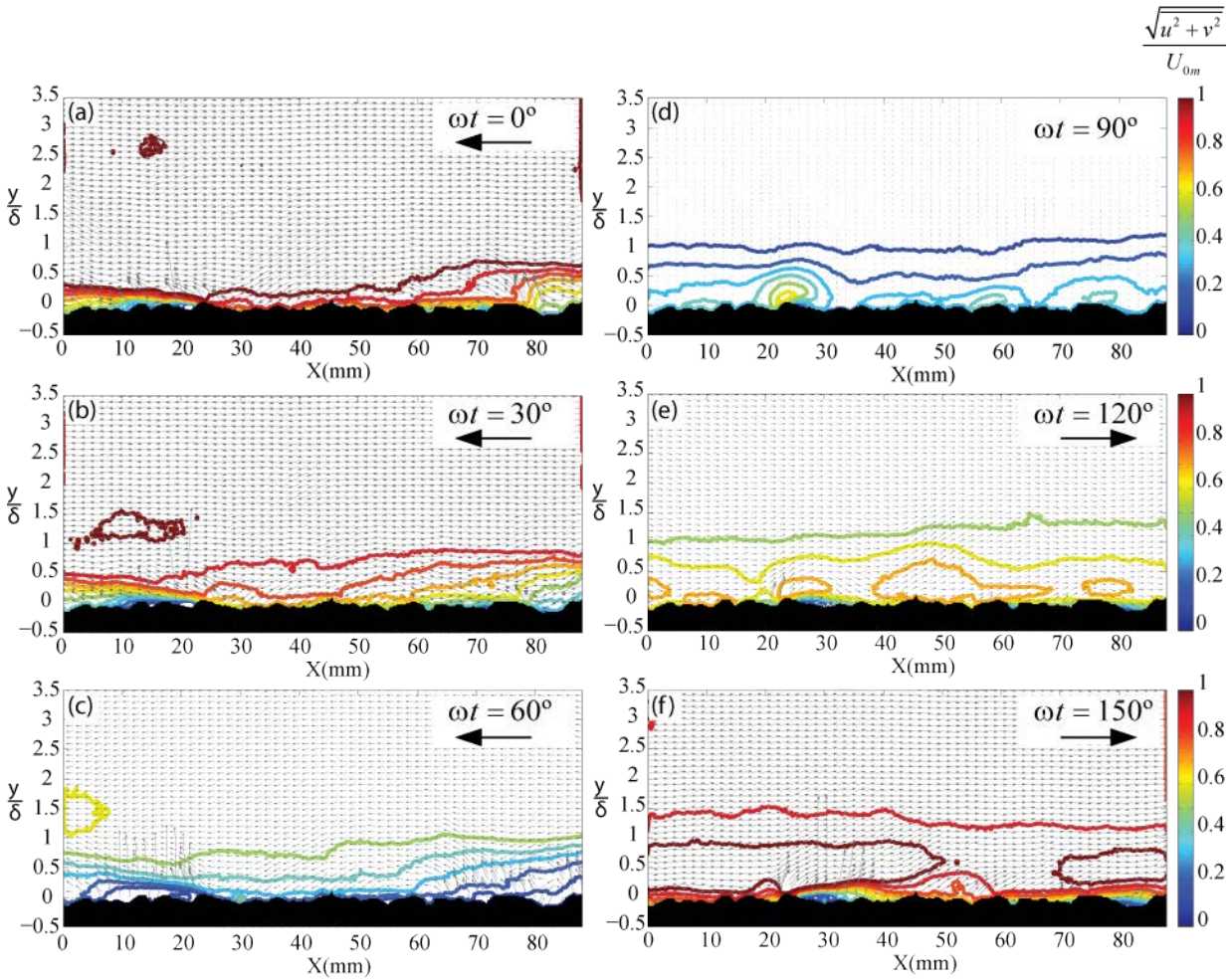

Figure 3.3. Phase-averaged velocity fields in the streamwise–wall-normal (*x*–*y*) measurement plane (contours represent velocity magnitude) over a half cycle of the larger roughness case (Test no. 9). Velocity normalized by U_{0m}. Arrows represent the direction of the free stream flow.

Images from each camera were interrogated separately, and the final merging of frames into elongated streamwise fields of view was performed at the instantaneous vector-field level. Before merging each camera frame, a simple matching code minimizing the differences between the right and left vector fields in the overlapping region was run in order to obtain the true vector field offsets. The final merged zone was taken as a smooth transition between the two fields thus avoiding any transition region in the middle of the composite field of view. As an example, Figure 3.3 presents the phase-averaged velocity fields over half an oscillatory cycle for the case of the larger roughness (Test no. 9) with color contours of velocity magnitude presented in the background. These fields highlight the degree of consistency maintained between the two fields as no clear transition is noted near the center of the streamwise domain where to two separate fields of view were stitched together.

3.3 Results and Discussion

3.3.1 Boundary Layer Thicnkess

A primary variable of interest in oscillatory flows is the boundary-layer thickness. According to Batchelor (1967), the Stokes length is only a function of the period and fluid viscosity for laminar oscillatory flows, and is given as

$$\beta = \left(\frac{\nu T}{\pi} \right)^{1/2} \tag{3.1}$$

However, the boundary-layer thickness can also be considered a time-dependent variable (e.g. Jonsson, 1980; Sleath, 1987). Jonsson (1980) defined the boundary-layer thickness as the minimum wall-normal position where the vertical profile of U equals the free-stream velocity, whereas Sleath (1987) used the defect velocity to define the boundary-layer thickness as the wall-normal position at which its amplitude was 5% of the free-stream velocity. Sumer (1987) defined the boundary-layer thickness as the wall-normal position at which the velocity profile reaches its maximum value, which coincides with the point of vanishing shear stress.

Figure 3.4 shows the temporal variation of the boundary-layer thickness calculated with the definition given by Sumer (1987), and Table 3.1 presents the results at $\omega t = 0$. This latter definition is used throughout and is related to the Stokes length [Eq. (3.1)] by

$$\delta = \frac{3\pi}{4} \beta \, . \tag{3.2}$$

The wall-normal origin in the rough-wall cases was taken as the mean height of the grain crests.

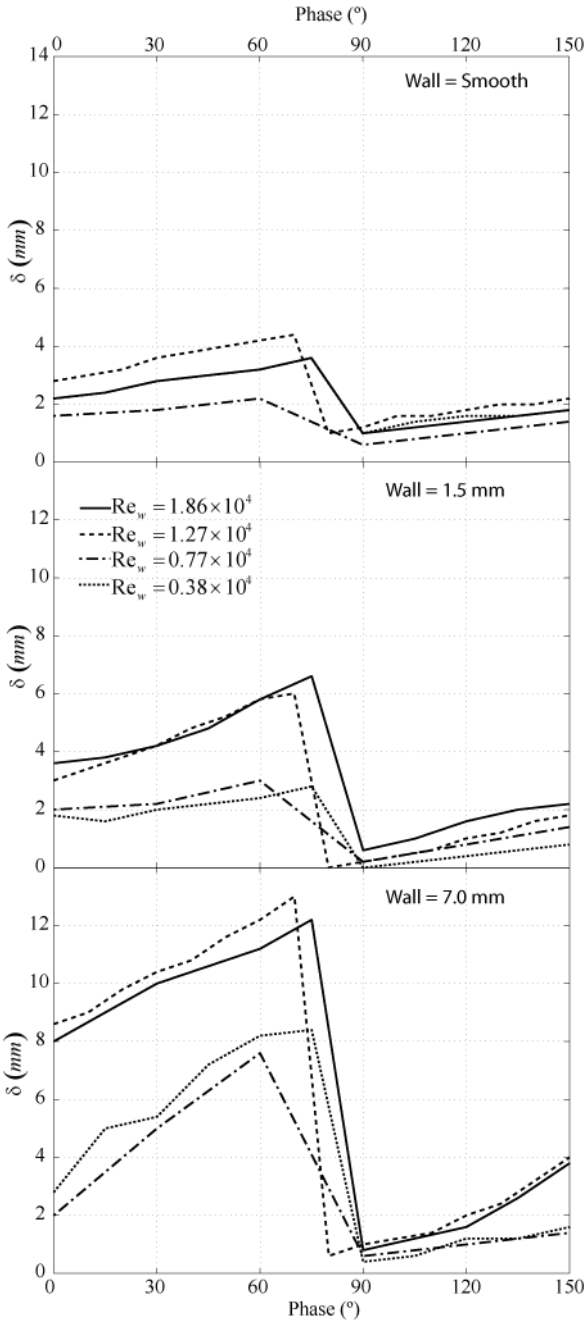

Figure 3.4. Boundary-layer thickness as a function of phase for the smooth wall (top), smaller roughness (middle) and larger roughness (bottom).

The temporal evolution of the boundary-layer thickness, Figure 3.4, displays different peak locations. This is an artifact of the temporal experimental resolution for each test, since the experiments with a period of 5 sec (Re_w=1.86·10^4, 0.38 ·10^4), possess a 10º phase increment between measurements. Experiments with a period around 3.3 sec (Re_w=1.27·10^4) were recorded every 15º and finally experiments of 1.7 sec period had 30º between phases (Re_w=0.77·10^4).

From Figure 3.4 it is submitted that the maximum boundary-layer thickness is reached between $\omega t = 75^o$ and $\omega t = 90^o$.

Smooth wall experiments show a dependence on the period, whereas in rough-wall experiments the boundary layer thickness depends more on the amplitude as suggested by Jensen et al. (1989). In the smooth-wall tests, Eq. (3.2) predicts extremely similar boundary-layer thicknesses to those determined directly from the experimental data, as shown in Table 3.2. The thicknesses predicted from the Li (1954) relationship given by

$$\beta = 4.6\delta, \tag{3.3}$$

are indeed quite different. This confirms that the smooth-wall boundary-layer thickness does not depend on the wave Reynolds number, but rather on the period of the oscillation.

Table 3.2. Boundary-layer thickness for the smooth-wall experiments. Data in mm.

Test no.	δ_{Exper}	$\delta_{Carstensen}$	δ_{Li}
1	2.2	2.4	4.8
2	2.8	3	5.8
3	1.6	1.7	3.4
4	2.2	2.4	4.8

In the rough wall cases, for smaller D_{50} and constant *A*, the boundary-layer thickness is inversely proportional to the period –Tests no. 5 and 6. Conversely, experiments with the largest roughness elements show an increase in boundary layer height proportional to the period, for experiments with constant *A* –Tests no. 9 and 10.

3.3.2 Friction Factor

The friction factor is commonly defined as

$$f_w = 2\frac{u_{*m}^2}{U_{0m}^2}, \tag{3.4}$$

where u_{*m} is the maximum friction velocity. However, this expression is subject to the computation of the friction velocity, which can be found in two different ways: (a) fitting a log-law profile to the experimental streamwise phase-averaged velocity profile, or (b) computing the

shear stress at the wall from the acquired PIV data. In this study, the friction velocity is defined following the latter definition, which does not presume the occurrence of a universal logarithmic velocity profile in the present rough-wall experiments.

Pedocchi & Garcia (2009) proposed the following expression

$$\frac{1}{\sqrt{f_w}} = 1.9 \ln\left(\frac{1}{1.5}\frac{A}{k_s}\sqrt{\frac{1}{f_w}}L_w\right), \tag{3.5}$$

where

$$L_w = \left\{\frac{1}{7.5}\left[1-\exp\left(\left\{\frac{1}{90}\frac{\mathrm{Re}_w}{A/k_s}\sqrt{\frac{f_w}{2}}\right\}^2\right)\right]+\frac{1}{2.1}\left(\frac{\mathrm{Re}_w}{A/k_s}\sqrt{\frac{f_w}{2}}\right)^{-1}\right\}^{-1} \tag{3.6}$$

to describe the friction-factor behavior for flows in the laminar-to-turbulent transition– when $A/(2.5D_{50}) > 30$ A/(2.5D$_{50}$) >- and Re$_w$ < 6.6 ·10^4. For these experiments, only Test nos. 5 and 6 can be fit within this range and the flow may be considered laminar based on this representation.

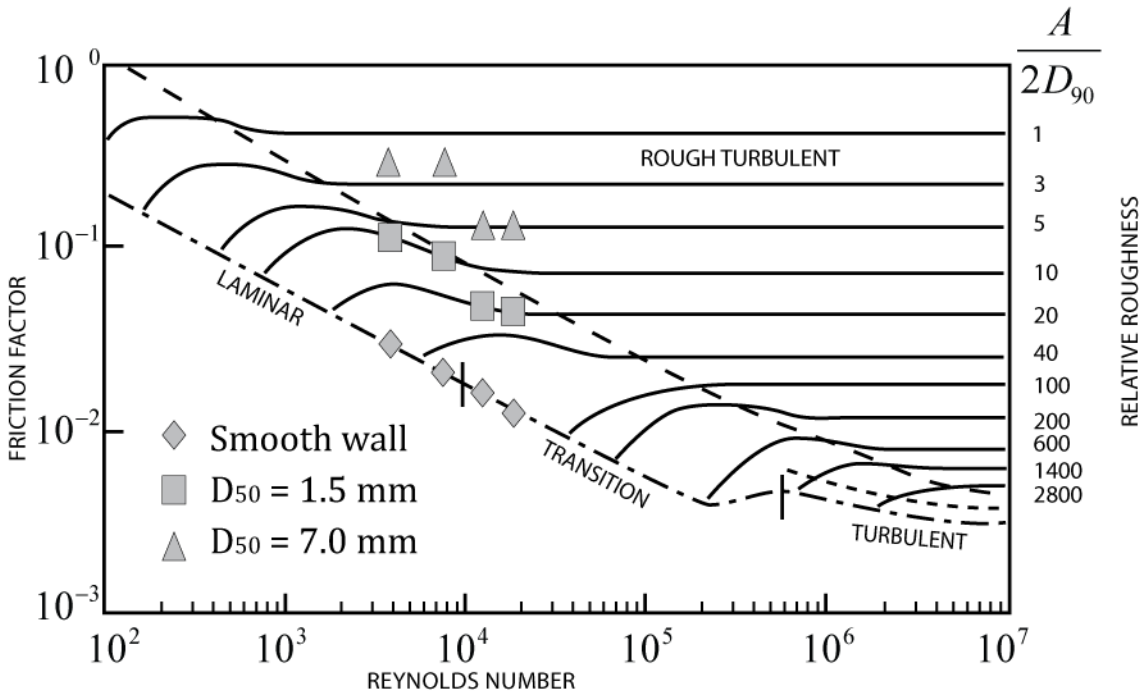

Figure 3.5. Friction factor defined within the Kamphuis (1975) diagram.

Kamphuis (1975) proposed a Moody-type diagram to describe the friction factor for oscillatory flows. Scenarios presented in this study are plotted within this diagram in Figure 3.5 and indicate the smooth-wall flows to be laminar and in the transition to smooth turbulent. In

contrast, the flows over the smaller roughness are found to be in transition toward fully-rough turbulent flow and the flows over the larger roughness are in the fully-rough regime marked by constant f_w with increasing Re_w.

Table 3.3. Friction factor and phase shift between friction and free-stream velocity computed using various equations.

	Test no	T (sec)	A (mm)	Re_w (10^4)	f_w (Kamphuis)	f_w (Pedocchi & Garcia)	φ (Pedocchi & Garcia)	φ (u* from Eq.11)	φ (u* from Eq.12)
Smooth	1	3.3	100	1.86	0.01	0,01	45º	~45º	~45º
	2	5	100	1.27	0.02	0,02	45º	~45º	~45º
	3	1.7	45.5	0.77	0.02	0,02	45º	~45º	~45º
	4	3.3	45.5	0.38	0.03	0,03	45º	~45º	~45º
Rough (D_{50}=1.5mm)	5	3.3	100	1.86	0.04	0,01	36º	~-10º	~10º
	6	5	100	1.27	0.05	0,02	36º	~-15º	~5º
	7	1.7	45.5	0.77	0.09	0,11	37º	~-15º	~30º
	8	3.3	45.5	0.38	0.10	0,08	36º	~-15º	~30º
Rough (D_{50}=7.0mm)	9	3.3	100	1.86	0.13	0,16	39º	~-5º	~10º
	10	5	100	1.27	0.13	0,16	39º	~-10º	~10º
	11	1.7	45.5	0.77	0.20	0,25	39º	~--30º	~0º
	12	3.3	45.5	0.38	0.20	0,25	39º	~-30º	~0º

Table 3.3 shows the differences between the Kamphuis (1975) approach and the Pedocchi & Garcia (2009) method. There is no significant difference in the friction factor for the smooth-wall experiments, because both authors use the same expression to compute this parameter ($f_w = 2/\sqrt{Re_w}$). However, the results begin to diverge for the experiments with rough walls; in particular the friction factor for Test nos. 5 and 6–considered in the laminar regime according to the Pedocchi & Garcia (2009) representation–is under-estimated if the

definition for laminar flows is used and compared to results obtained with the Kamphuis (1975) diagram. This may indicate that such experiments are not in the laminar regime but rather in the transition to rough turbulent. The empirical formula proposed by Pedocchi & Garcia (2009) for flows in transition is used for Tests nos. 7 to 12 (although they cannot be fitted in any of the flow ranges defined by Pedocchi & Garcia (2009) because $A/(2.5D_{50})$ <-30), resulting in approximately the same results as reported by Kamphuis (1975).

These observations confirm that the Kamphuis (1975) definition of the flow regimes better represents the experiments carried out in this research. Nevertheless the definitions of the friction factor from Pedocchi & Garcia (2009) can also be used because the smaller roughness experiments are in the laminar-to-turbulent transition regime and the larger roughness experiments are in the rough turbulent regime but very close to the transition zone.

3.3.3 Mean Velocity Fields

Mean velocity fields were computed using phase averaging, as shown in Eq. (3.7), where U_0 is the velocity of the outer flow and the piston, U_{0m} is the maximum streamwise velocity of the outer flow, U_m is the maximum streamwise velocity at each point, and equal to U_{0m} for $y = \infty$. Index *i* is used to define every cycle, ω is the frequency and *t* is the time (thus, ωt is the phase). *N* is the number of cycles over which averaging was performed.

$$\begin{aligned} U_0\left(\hat{t}\right) &= -U_{0m}\cos\left(\omega\hat{t}\right) \\ U^i\left(x,y,\hat{t}\right) &= -U_m^i\left(x,y\right)\cos\left(\omega\hat{t}\right) \\ \bar{U}\left(x,y,\hat{t}\right) &= \frac{1}{60}\sum_{i=1}^{i=60}U^i\left(x,y,\hat{t}\right) \\ \bar{U}\left(x,y,\hat{t}\right) &= -U_m\left(x,y\right)\cos\left(\omega\hat{t}\right) \end{aligned} \tag{3.7}$$

At each phase, $\omega\hat{t}$, an ensemble average and fluctuation of all cycles were computed in order to define subsequent quantities related to turbulence (e.g. Reynolds stresses and turbulence intensities).

$$\mathrm{var}\left(y,\omega,t\right) = \int_{-L/2}^{L/2}\mathrm{var}\left(x,y,\omega,t\right)dx \tag{3.8}$$

One advantage of using PIV is that it allows for spatially-averaged variables in the *x* direction, Eq. (3.8), since the field of view and the resolution gave more than 200 points in this direction. Importantly, the field of view was far enough from the ends of the flume to develop homogeneous flow characteristics in the direction of oscillation.

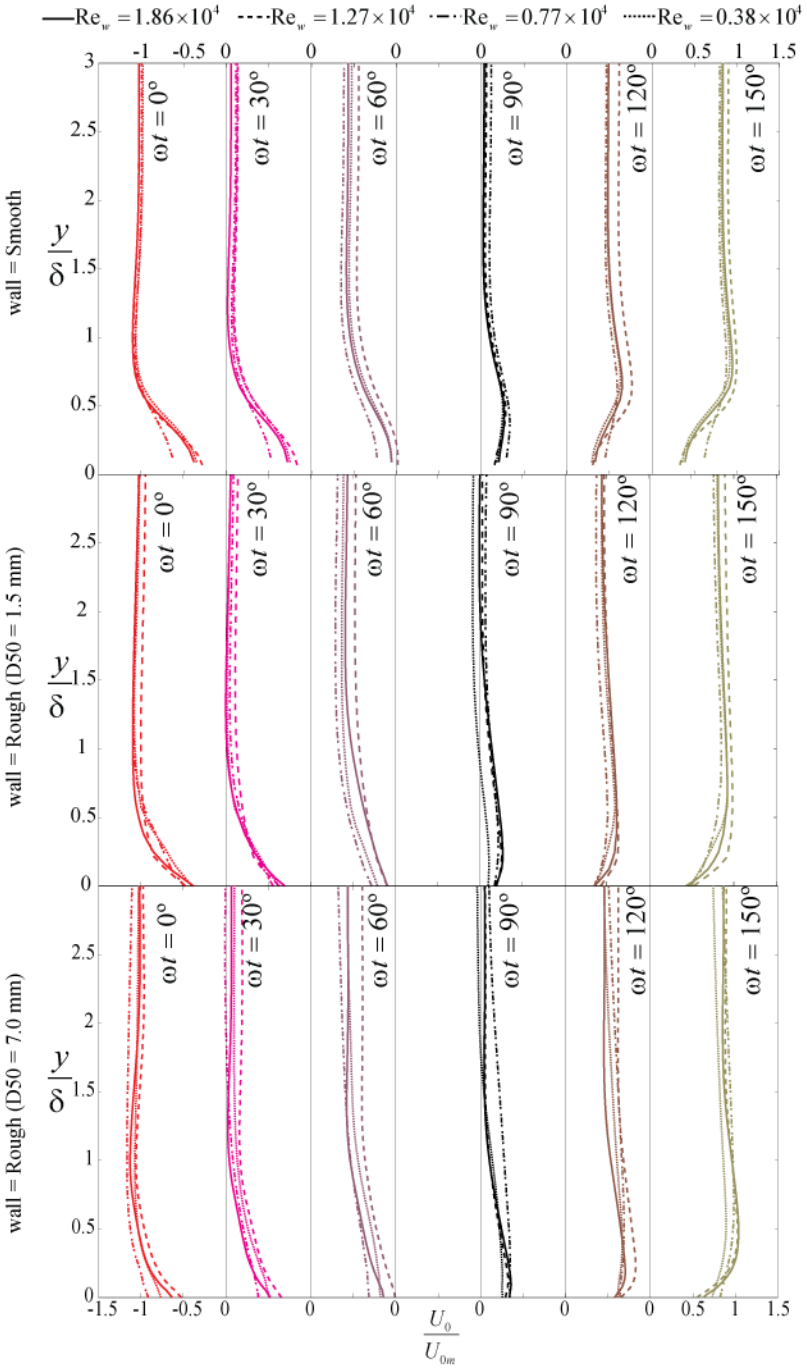

Figure 3.6. Mean streamwise velocity profiles as a function of phase for the smooth wall (top), smaller roughness (middle) and larger roughness (bottom).

Mean streamwise velocity profiles as a function of wall-normal position for each test are shown in Figure 3.6 (only half cycles are shown). These phase-averaged profiles were computed by ensemble-averaging instantaneous velocity fields of a given phase followed by line averaging the resulting ensemble-averaged fields (such as those shown in Figure 3.3 for Test no. 9, for example) in the streamwise direction. Boundary-layer thickness and free-stream maximum velocity are used to normalize the wall-normal coordinate and the streamwise velocity,

respectively. Regardless of the complexity of the flow close to the wall (Figure 3.3, for example), this scaling leads to reasonable collapse onto one curve for each phase and will be further used to define other dimensionless variables. As seen in Figure 3.6, in the smooth wall case the flow reversal close to the wall begins around $\omega t = 60^{o}$. However, in the rough-wall cases, the boundary layer begins a little later, but always prior to the flow reversal.

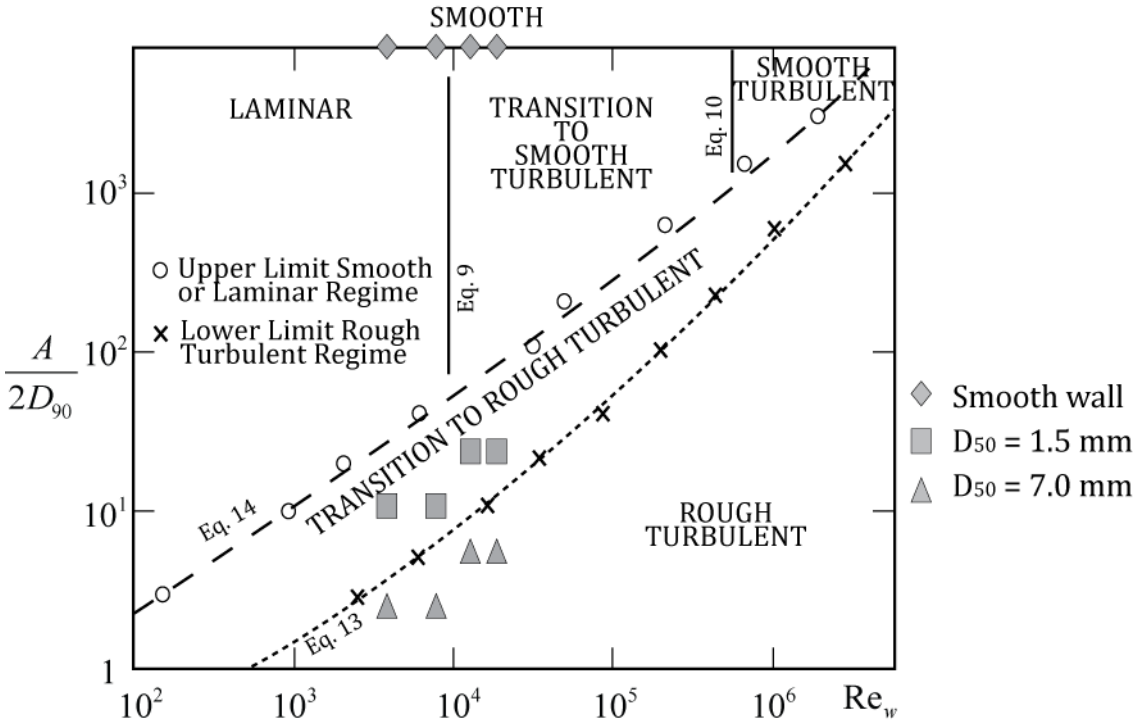

Figure 3.7. Flow regime as defined by Kamphuis (1975).

The flow regime is given by the ranges reported by Kamphuis (1975) (Figure 3.7). As indicated previously, the flow regime varies during any given cycle. However, it is considered that most of the stages will be within the fixed flow regime used as a global definition for the whole cycle. Figure 3.7 shows smooth wall experiments to be in the zone dividing the laminar and the transition to smooth turbulent regimes. In order to determine whether they might be considered laminar or in the transition zone, smooth-wall laminar profiles were fitted to the Stokes' laminar solution of the momentum equation

$$U_0(y,t) = -U_{0m}\left[\cos(\omega t) - e^{-\delta_1 y}\cos(\omega t - \delta_1 y)\right], \qquad (3.9)$$

using the inverse of the Stokes length, $\delta_1 = 1/\beta$, as the fitting parameter (Figure 3.8). Table 3.4 displays the comparison between the fitted results and the expected value of β, with good agreement found between them.

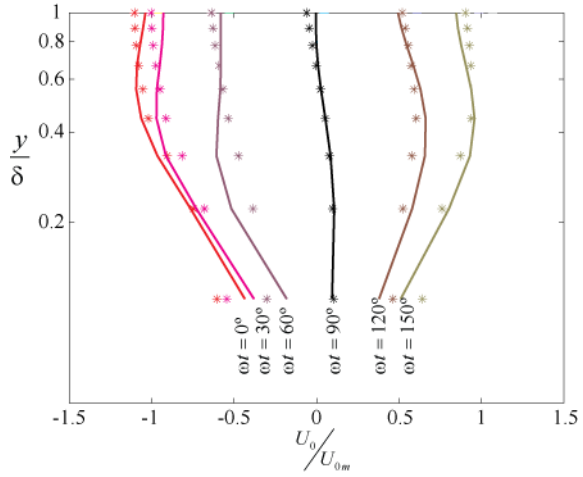

Figure 3.8. Fitting of smooth-wall velocity profiles to theoretical solution (Test no. 1).

Table 3.4. Comparison of the δ_1 parameter between the theoretical results and the curve fitting of the smooth-wall laminar experiments. Data in 1/mm.

Test no.	δ_1^{fit} (10^3)	δ_1^{theory} (10^3)
1	1.26 ± 0.11	1.02
2	0.89 ± 0.09	0.79
3	2.14 ± 0.46	1.25
4	1.19 ± 0.12	1.02

Experiments with the smaller roughness are all considered in the transition to rough turbulent whereas experiments with the larger roughness exhibit rough turbulent behavior, but lie very close to the transition to rough turbulent zone. In this latter case, a logarithmic law proposed by Jonsson (1980) as follows,

$$U_0(y,t) = -\frac{u_{*m}}{0.4}\ln\left(\frac{30y}{k_s}\right)\cos(\omega t+\phi), \qquad (3.10)$$

was fitted to experimental values with no feasible results for k_s parameter in some phases. This observation indicates that the larger roughness experiments should not be considered in the turbulent rough regime. However, the ratio between turbulent and viscous stresses is in the order of 10^2, which confirms that the flow is in the turbulent regime. The existence of a certain

logarithmic profile is left for further study on the applicability of a general logarithmic law for oscillatory flows in transition.

3.3.4 Shear Stresses and Shear Velocities

The phase-averaged and streamwise line-averaged shear stress is defined in two different ways: (i) addition of the viscous and turbulent contributions to total shear stress given by

$$\frac{\tau(y,\omega,t)}{\rho} = -\overline{u'v'}(y,\omega,t) + \nu\frac{\partial U(y,\omega,t)}{\partial y}, \tag{3.11}$$

and (ii) the integral of the momentum equation assuming no mean vertical velocity expressed as

$$\frac{\tau(y,\omega,t)}{\rho} = \int_y^{\infty}\frac{\partial\left(U_0(\omega,t)-U(y,\omega,t)\right)}{\partial t}dy = \int_y^{\delta(\omega t)}\frac{\partial\left(U_0(\omega,t)-U(y,\omega,t)\right)}{\partial t}dy . \tag{3.12}$$

This latter representation only requires knowledge of mean velocity values, and does not rely upon direct measurements of the turbulence which could be under-resolved in any high-Re experiment. The upper limit in these calculations is taken as the temporal boundary-layer thickness since the stresses should, on average, vanish beyond this height. Finally, the friction velocity, is given by

$$u_*(\omega,t) = \sqrt{\frac{\tau(0,\omega,t)}{\rho}} . \tag{3.13}$$

Figure 3.9 presents the results for friction velocity obtained using the shear stress definition from Eq. (3.11) and Eq. (3.12). For the smooth-wall tests, a difference in the absolute value is found between the two definitions of the bottom shear stress (Figure 3.9a). Values obtained using the integral of momentum equation are twice as large as the friction velocity computed using the sum of the viscous and Reynolds shear stresses. This is likely due to the false assumption of momentum flux across the lower boundary of the control volume; when this lower boundary is the wall, such flux is zero, and this is not introduced in the derivation. Another possible reason explaining the difference in friction velocity amplitude is the underestimation of turbulent stresses due to the laser light reflections in the near-wall region when viscous and shear stresses addition is used to compute the total stresses. However, when Eq. (3.12) is used, the scatter between scenarios is larger especially during the flow reversal stages due to high pressure gradients which are difficult to capture with a constant sample rating.

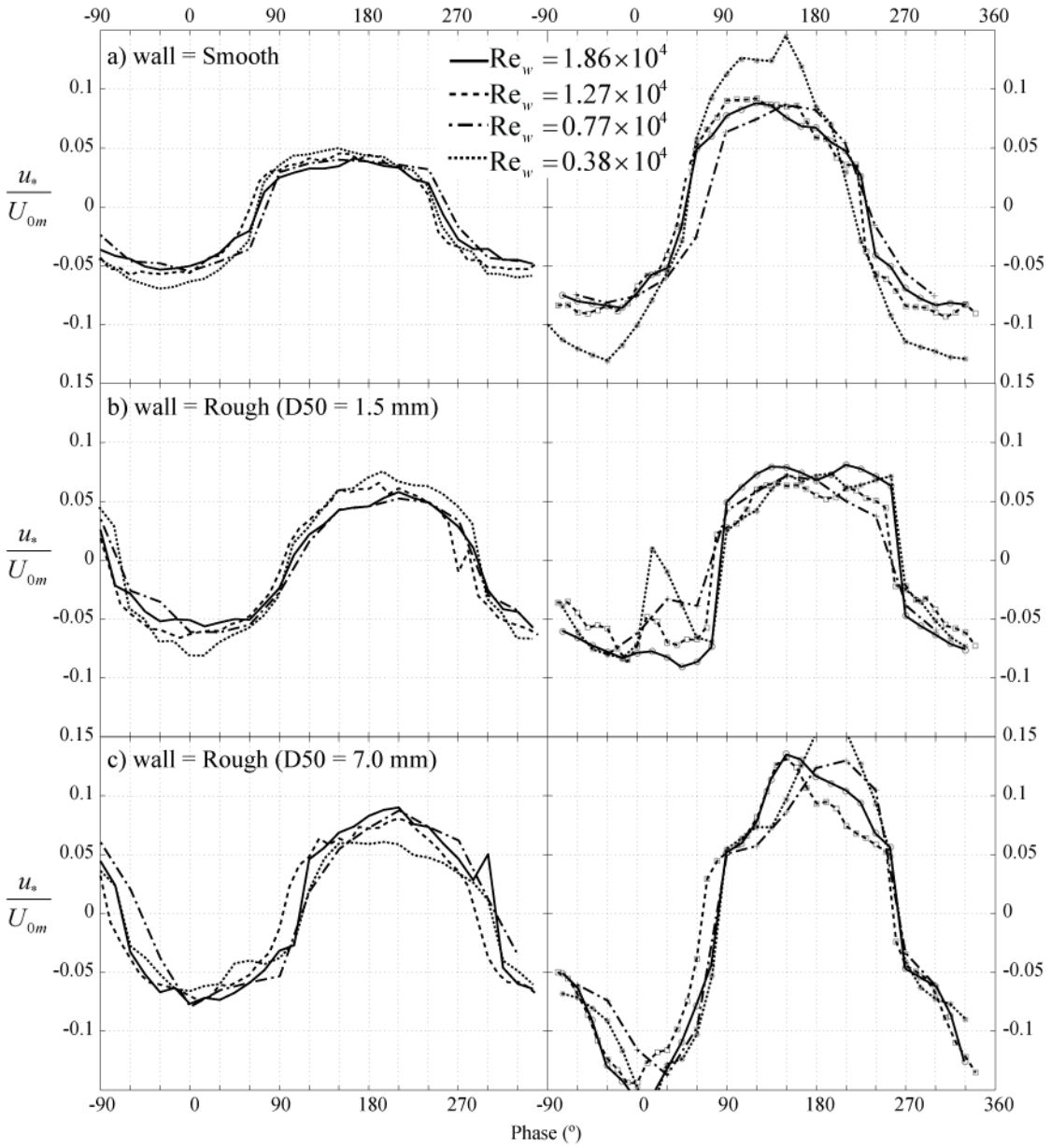

Figure 3.9. Friction velocity as a function of phase. Left column: sum of viscous and Reynolds shear stresses [Eq. (3.11)]; Right column: integral of momentum equation [Eq. (3.12)].

In the rough-wall experiments, the scatter is higher when the integral of momentum equation is used as well. In terms of friction velocity amplitude, the results are slightly higher when computing with Eq. (3.12), in particular for the larger roughness tests (D_{50}=7 mm). This is likely due to the assumption of no vertical flux momentum in Eq. (3.12), as the mean vertical velocity was considered to be zero. However if the vertical flux momentum term, $\overline{U}\overline{V}$, is added to Eq. (3.12) the differences between the results obtained from Eq. (3.11) and Eq. (3.12) are not reduced significantly. Another reason that may explain the differences in amplitude of the friction velocity obtained using both equations is the number of profiles used to compute the average in the streamwise direction. Friction velocity is obtained from Eq. (3.13), and so the

consideration of the zero level plays a role. Zero level for the rough walls is defined as the mean elevation of the grain crests, and this value is going to be lower for experiments carried out with a higher roughness size. Thus, the number of profiles used to average over the streamwise direction is lower for larger roughness cases.

Another variable differing substantially when Reynolds stresses are computed using either Eq. (3.11) or Eq. (3.12) is the phase shift between shear and free stream velocity. Interestingly, the phase lead is also a parameter that can be used to define the flow regime. In the laminar case, regardless of the wall roughness used, the phase shift was found by previous authors –i.e. Jonsson (1980), Pedocchi & Garcia (2009)-, to be independent of the Reynolds number, with a constant value of 45º, to follow the expression

$$\sin\phi = \frac{1}{\sqrt{2}}. \tag{3.14}$$

In particular, for oscillatory flows over smooth walls Jensen et al. (1989) detected that for $Re_w > 6\cdot10^4$ the phase lead begins to decrease from $1/\sqrt{2}$ with increasing values of the wave Reynolds number until values lower than 10º and close to no phase shift. Thus, the flow regime changes from the laminar to smooth turbulent regime. In Figure 3.9a and Table 3.3, both methods of computing shear stresses yield the same phase shift between the friction velocity and the free stream velocity. In fact, the results are exactly those predicted by Eq. (3.14) and Jensen et al. (1989), although Tests nos. 3 and 4 are in the early transition to smooth turbulent regime, according to the Kamphuis (1975) diagram shown in Figure 3.7.

For rough walls, Pedocchi & Garcia (2009) suggested an empirical relation between the friction factor and the phase shift valid only for flows in the laminar-to-turbulent transition regime, given by

$$\sin\phi = \frac{1}{\sqrt{2}} - \frac{1}{30}\sqrt{\frac{1}{f_w}}, \tag{3.15}$$

with the friction factor obtained using Eq.(3.5) and Eq. (3.6). In Eq. (3.15), the higher the friction factor, the higher the phase shift. Figure 3.10 shows the phase shift obtained using Eq. (3.15) and compared to other authors (u_* was computed using Eq. (3.4) from the friction factor obtained following Pedocchi & Garcia (2009) empirical formula). Compared to other experiments, phase shift is under-predicted using Eq. (3.15), meaning that the friction factor is

under-predicted as well. Yet the underestimation of the fitting parameter z_0, may be another reason explaining the flow regime location of the experiments detailed in this section.

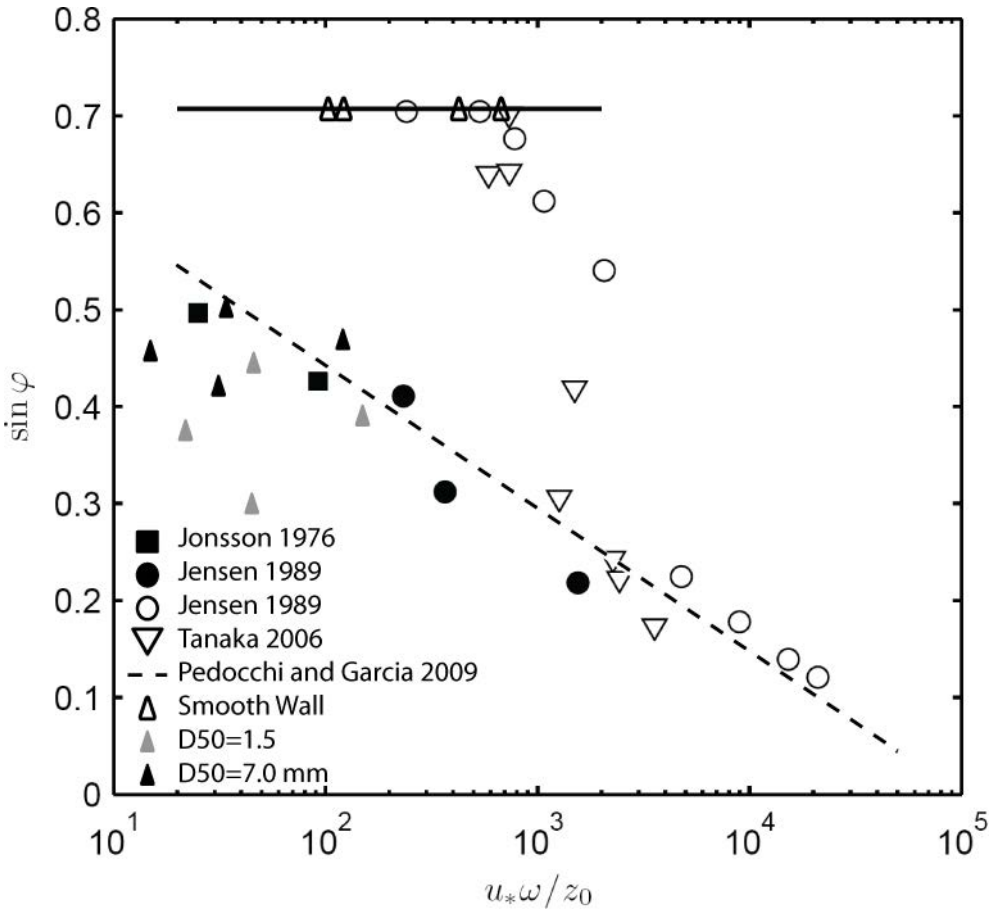

Figure 3.10. Experimental values of the phase shift between the friction velocity and the free-stream velocity. Filled symbols: rough bed experiments. Open symbols: smooth bed experiments. Figure from Pedocchi & Garcia (2009)

Table 3.3 shows the differences found in the phase shift when Eq. (3.15) is used, and when the phase lead is obtained from Figure 3.9b and Figure 3.9c. When the total stress decomposition into viscous and Reynolds stresses is used, the phase lead is negative–implying that it occurs after the free stream peak velocity. Conversely, if the friction velocity is computed with the integral of momentum equation, angles obtained are positive and, some are closer to the values predicted with Eq. (3.15), as shown in Table 3.3.

In order to understand further where the negative phase lead values originate when the friction velocity is computing using the viscous and turbulent stresses addition, Figure 3.11 details each component of the total stresses in Test no. 5, considered representative of all other tests. In Figure 3.10 Reynolds shear stresses are retarded with respect to viscous stresses, and so are the cause of the phase lead between friction and free-stream velocity. However it is

interesting to note that viscous stresses are in phase with the free-stream velocity in Figure 3.10: according to Batchelor (1967) and Jonsson (1980), viscous stresses should have a phase lead of 45º with respect to the free flow because of the action of friction forces in the viscous sublayer. This indicates that the defined zero level may not be located at the viscous sublayer but a little bit above.

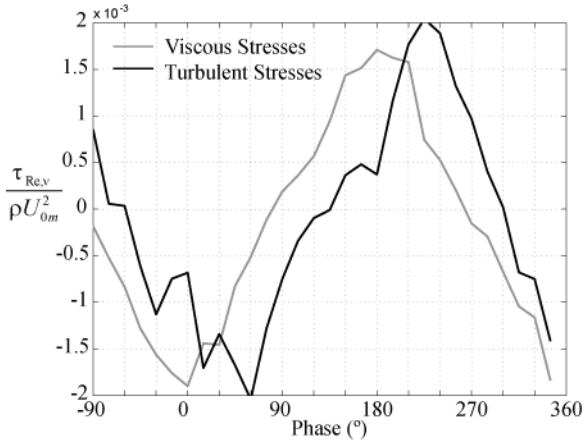

Figure 3.11. Viscous and turbulent stresses for Test no. 5 (smaller roughness case) as a function of phase.

Figure 3.12 shows the vertical profile of the maximum shear stress phase found for Test no. 5 computed from the sum of viscous and turbulent stresses. The value obtained for the zero level is even higher than 180º, meaning that the maximum is retarded with respect to the free-stream velocity, as mentioned previously. Furthermore, it is important to mention that, below zero, the phase peak decreases indicating that the viscous sublayer is, indeed, below the zero level. Given these observations, the over-delayed phase shift in the results shown in Figure 3.9 are likely due to overestimation of the zero level.

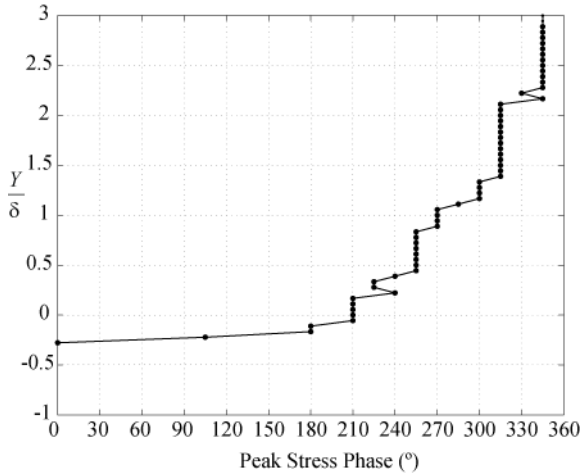

Figure 3.12. Vertical profile of maximum shear stress phase [computed from Eq. (3.11)]. Test no. 5 (smaller roughness case).

When phase shift is computed using the friction velocity obtained from the integral of momentum equation, [Eq. (3.12)], the results (Figure 3.9, right column) are closer to those predicted by the relationship proposed by Pedocchi & Garcia (2009), Table 3.3. Phase shift for the smaller roughness should be around 30º for all scenarios, and this angle is found only in Test nos.7 and 8. Sleath (1987) suggested that this may also be due to the false assumption of zero mean vertical flux, as detailed previously. However, if the term of the mean vertical momentum $\overline{U}\cdot\overline{V}$ is included in Eq. (3.12), the phase shift does not change significantly and the error is attributed to the dispersion of the data. In the case of the larger roughness, no phase shift is observed when the integral of momentum equation is used to compute the friction velocity.

3.3.5 Turbulence Intensities

Figure 3.13 illustrates how the root-mean-square (rms) of the turbulent velocity fluctuations progress in phase and as a function of wall-normal position. The differences found for the larger roughness between the two higher Reynolds number experiments and the other pair, are mainly due to the dimensionless vertical distance, because larger values of boundary-layer thickness were observed.

In all tests, maximum values are reached at the maximum free-stream velocity phases ($\omega t = 0^o$). As suggested by Jensen et al. (1989) , at the flow reversal phases, turbulence becomes uniformly distributed across the depth. For smooth-wall conditions, all profiles fall on a similar curve, in each phase, and turbulence is damped around $y \approx 0.5\delta$, and becomes constant for $y > 0.75\delta$. When k_s increases, turbulence is propagated upwards, though for the smaller roughness, turbulence is still damped above $y \approx 0.5\delta$, in earlier stages, for Test nos. 5 and 6. In the case of the larger roughness, turbulence is directly related to the amplitude of the oscillation and is diffused upwards with little damping.

Recalling that smooth-wall experiments fall within the laminar and laminar-to-turbulent transition regimes, the incipient turbulence found close to the wall was previously described by Carstensen et al. (2010). As he pointed out: “a certain type of coherent structure called vortex tubes may appear due to the inflection-point shear layer instability when the deceleration begins”. Although experiments in the present study are slightly below the Reynolds numbers that Carstensen et al. (2010) defines as the threshold for these structures to emerge, this is thought to be the best explanation for the existence of local turbulence in the tests where the bulk flow is considered to be laminar.

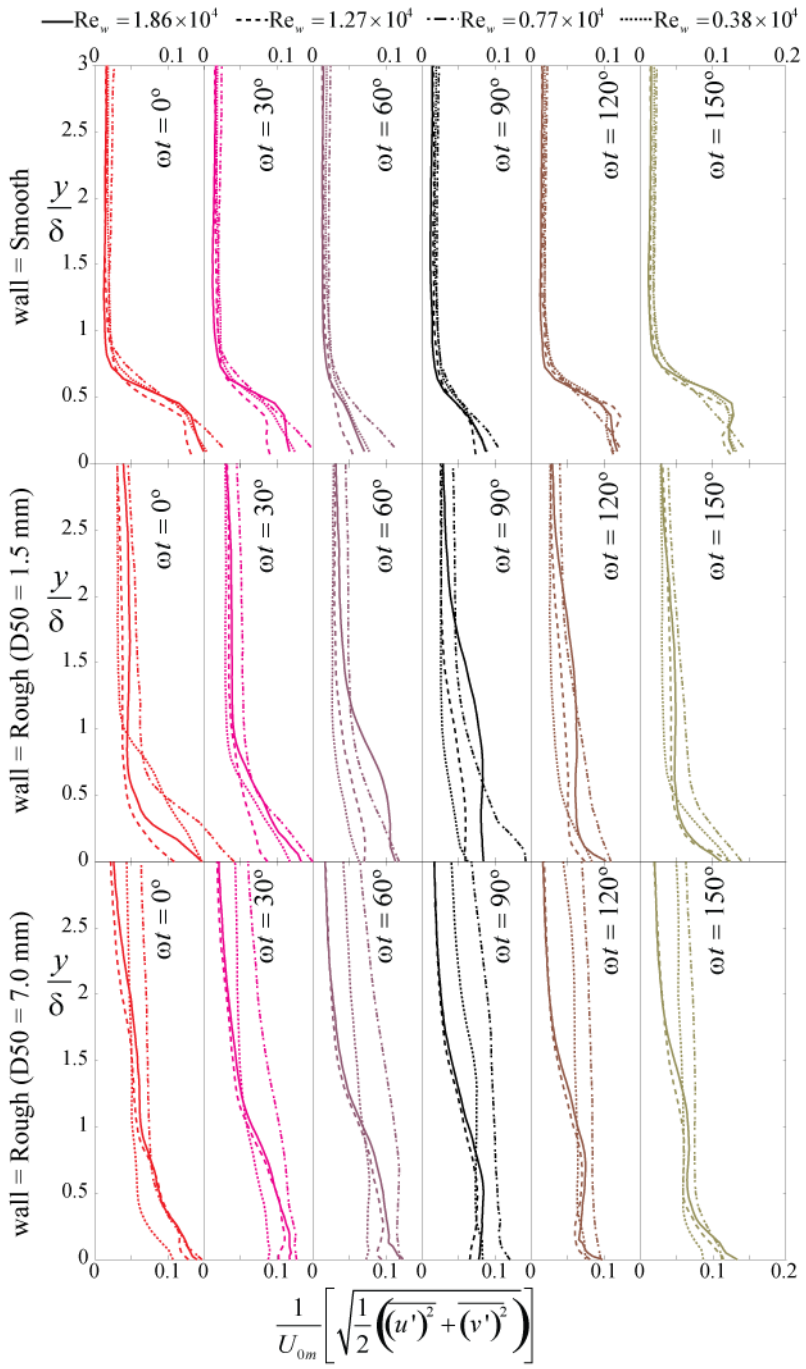

Figure 3.13. Turbulence intensity profile for the smooth wall (top), smaller roughness (middle) and larger roughness (bottom).

Finally, the peak in turbulent kinetic energy observed experimentally by Jensen et al. (1989) and numerically by Pedocchi et al. (2011), albeit for higher Reynolds number, at an approximate value of $y^+ = 10$, is also found in the current study. However, the levels of tke are underestimated herein owing to limited PIV spatial resolution as well as determination of the tke based only on the two velocity components measured by PIV.

3.4 Summary

This chapter has presented an initial characterization of the oscillatory flow reproduced experimentally. The diagram proposed by Kamphuis (1975) was found to better define the flow regime, showing that most of the scenarios presented in this chapter fall in the laminar-to-turbulent flow description.

Variables were computed using different methods and compared among each other. In particular, friction velocity was computed using two different methods to obtain bottom shear stresses: i) the viscous and turbulent stresses addition and ii) the integral of momentum equation. The third method, consisting on fitting mean horizontal velocity vertical profiles to an experimental curve proposed by Jensen et al. (1989) for rough walls, could not be used because flows were not considered completely turbulent. Therefore phase shift between friction velocity and the free stream velocity was also found using both the viscous and turbulent stresses addition and the integral of momentum equation. The last one yielded better results than the former one. However, both results were highly sensitive to the zero level definition.

Finally turbulence close to the wall was detected in the smooth wall scenarios even when they were fitted in the laminar regime in the diagram proposed by Kamphuis (1975).

Chapter 4: Coherent Structures In Oscillatory Flows Over Sand Rough Beds

This chapter further analyzes the experiments defined in Chapter 3 focusing on the coherent structures present in oscillatory boundary layers in the laminar-to-turbulent regime.

4.1 Introduction

Unsteady flows are of great importance for their prevalence in nature and industry. Due to the difficulties in studying unsteady flows, canonical cases have been used to characterize for example acceleration and deceleration phases. Oscillatory flows are of particular interest because of their great relevance in the study of biological processes such as human breath cycles, nutrient cycling in plants, and also of physical processes involving sediment transport under wave action. These flows have additionally received a great deal of attention due to their simple motion.

The particular interest in oscillatory flows rises from their changing characteristics along a cycle. Depending on the Reynolds number –sometimes defined as $Re_w = U_0 A/\nu$, or as $Re_\beta = U_0\beta/\nu$, with U_0 the maximum free stream velocity, A the amplitude of oscillation, β the Stokes length and ν the fluid kinematic viscosity-, the flow can start with a laminar regime move towards the transition to rough turbulent and have some phases in the rough turbulent regime. However, several authors work with time independent variables assuming that each variable is defined in the most present flow regime during the cycle.

Oscillatory flows were first addressed by the so called Stokes boundary layer with the theoretical work developed by Lamb (1993) and Batchelor (1967). Experimental studies began with the work by Li (1954) who made the first steps towards flow regime definition. Kamphuis (1975) focused his experiments on the friction factor under oscillatory flows developing Moody-type diagram and a flow regime distribution chart. Several authors carried out more experimental work using a wide range of Reynolds numbers, and different wall types –i.e. Jonsson (1980), Hino et al. (1983), Sleath (1987), Sumer (1987) and Jensen et al. (1989)-. Many of the previously cited works tried to define oscillatory flows using the steady flow approach. For instance, Jonsson (1980) was the first to propose a time dependent logarithmic law valid for most of the flow phases in the turbulent regime. This formulation was improved by Sleath (1987) with a larger number of experiments, and further by Jensen et al. (1989).

Simple variables like the boundary layer thickness or friction factor were also included in the aforementioned studies. The Stokes length ($\beta = \sqrt{\nu T/\pi}$ where T= Oscillation period) is the most used variable in defining a characteristic length scale. However, when the lower wall is fixed and a sinusoidal pressure gradient is driving the flow, it is more convenient to use the definition made by Sumer (1987): the boundary layer thickness can be taken as the wall normal

position at which the velocity profile reaches its maximum value. For laminar flows in smooth wall Sumer (1987) definition of the boundary layer thickness, δ, is related to the stokes length by

$$\delta = \frac{3\pi}{4}\beta \tag{4.1}$$

The phase shift between bottom shear stress and the free stream surface is a phenomenon of particular interest in oscillatory flows. This phase shift has a maximum bound at 45º, a shear stresses peak occurring 45º before free stream velocity peak, and decreases with the Reynolds number until it vanishes. This phase lead is mainly due to friction forces at the wall and is maximized for laminar flows, indicating that shear stresses are responsible of the phase shift decrease.

Hino et al. (1983) and Sleath (1987) also focused their research on defining the turbulence close to the wall. Particularly Sleath (1987) described a periodic formation of jets and bursts close to the wall that were affecting other variables such as the bottom shear stresses. Of particular interest was their study of the turbulent viscosity using the steady flow approach. At a certain height eddy viscosity can be negative and thus represent a flux momentum towards the lower wall. This is because the maximum of the streamwise velocity profile is not located at the same height as the zero on turbulent stresses, and so a singular point occurs at this vertical location for the eddy viscosity.

Most of the experimental works completed so far were considered either in the fully laminar or in the fully turbulent regime. However, some research has also been done for flows in transition. Akhavan et al. (1991a) did experimental work in a circular pipe for a wide number of Re_β. They continued their research with a numerical investigation of the same phenomenon Akhavan et al. (1991b) aiming to describe the instability that triggers turbulence along smooth walls. They found that the transition point to turbulent flow is mainly due to resonance from the experimental setup. This can create a two-dimensional large wave triggering the growth of three dimensional structures formed by small perturbations along the wall. Pedocchi & Garcia (2009) focused their theoretical work on defining a friction factor formula for flows in the smooth to turbulent transition zone and an expression for the phase shift between shear- and free-stream velocities. They used data from Jonsson (1980), Jensen et al. (1989) and Tanaka & Samad (2006). In their most recent work, Pedocchi et al. (2011) performed a Direct Numerical Simulation (DNS) of an oscillatory boundary layer focusing on the role of every term in the TKE balance equation, and calibrating the conditions after Jensen et al. (1989) . They found that the

TKE production term is responsible for maintaining the level of turbulent intensity during flow reversal.

The work presented herein describes coherent structures found within the laminar to turbulent transition regime. Four scenarios with different Reynolds numbers $Re_w \sim 0.4 - 2 \times 10^4$ $\left(Re_\beta \sim 100 - 200\right)$ where tested under smooth bed conditions as well as two different rough beds. Flow fields were studied using the 2D-PIV visualization technique with two cameras aligned side by side in order to increase the field of view in the streamwise direction.

Coherent structures in steady flows have been largely described and are still a focus in the research community. In the case of oscillatory flows, the unsteadiness of the process adds elements of particular interest. Several authors have studied the existence of turbulence over smooth and rough walls for different Reynolds numbers (e.g. Hino et al. (1983), Sleath (1987), Jensen et al. (1989), and Blondeaux et al. (2004)). In general it is known that turbulence appears at the latter stages of the acceleration phases and is maintained during the deceleration half cycle. At the early stages of the acceleration phase flow can revert back to the laminar regime depending on the Reynolds number. Experimental and numerical studies have shown that turbulence may start in smooth walls for $Re_\beta \sim 86$, where the flow is unstable to initial perturbations coming from wall imperfections or setup defects, Vittori & Verzicco (1998). When the Re_β is between 100 and 500, flow perturbations are observed and some authors consider this a disturbed laminar regime, because the overall characteristics of the flow are still similar to the laminar case –i.e- Blondeaux & Vittori (1994), Vittori & Verzicco (1998) and Costamagna et al. (2003)-. When $Re_\beta < 3500$ larger parts of the cycle present turbulent phases and the regime is deemed intermittently turbulent. One of the most recent experimental studies published comes from Carstensen et al. (2010), who focused their research on coherent structures in transitional flows over smooth walls. They described two different structures depending on the Reynolds number. The first one, called vortex tubes –for $Re_w < 3 \times 10^5$- , were defined as 2D spanwise rotating tubes appearing at the end of the deceleration phase, and disappearing at the end stages of the acceleration phase. Vortex tubes were primarily created by the Kelvin-Helmholtz instability in the shear layer at phases prior to the flow reversal. The second structure, named turbulent spots $Re_w > 1.5 \times 10^5$, was described as 3D structures appearing randomly in space. Mazzuoli et al. (2011), focused his numerical research on reproducing the latter structures, following the scheme used previously by Vittori & Verzicco (1998) and Costamagna et al. (2003).

Structures present in oscillatory flows over rough beds were first described as jets and bursts, Jensen et al. (1989). In fact, the distinction between jets and bursts was that the former structures were associated with individual roughness elements and occured at specific phases, Sleath (1987). Fornarelli & Vittori (2009) performed numerical simulations over a rough wall formed from a regular pattern of semi-spheres following the experiments of Keiller & Sleath (1976). Both studies described the formation of shear layers during the acceleration phases, similar to the jets described previously by Sleath (1987).

This section uses the experiments already described in Chapter 3. Smooth wall experiments were defined in the laminar and laminar-to-turbulent regimes; rough walls are mainly in the laminar-to-turbulent regime. Then the analysis of the coherent structures will widen the range of experiments used so far.

4.2 Experimental setup

Experiments were conducted in the the Ven Te Chow Hydrosystems Laboratory at the University of Illinois at Urbana-Champaign in a U-shaped oscillatory flow water tunnel Garcia et al. (2004). Figure 4.1 shows a sketch of the flume identifying a working section approximately 0.25 m high by 0.20 m wide and 4 m long. The surface and side walls are composed of smooth transparent Perspex, and the bed is composed of a bare PVC plate. For smooth-wall experiments, the PVC plate remained clean of sediment. Gravel was glued to the surface of the PVC plate for rough bed conditions.

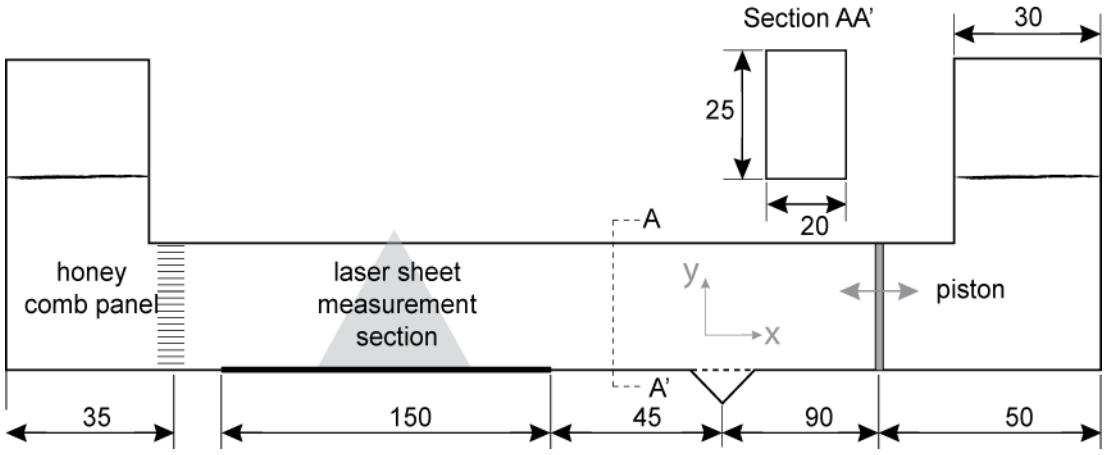

Figure 4.1. Sketch of the oscillatory tunnel, lateral view. Units in cm.

The oscillatory flow was driven by an Exlar electrical actuator powering a piston located at the right end of the flume. The actuator was controlled by a computer through a National Instruments card and a custom program devised with LabView which generates a repeatable

sinusoidal motion. Cycles were recorded continuously without stopping the actuator, but not consecutively and so they are considered independent experimental runs. The sinusoidal motion was set using an amplitude control (accuracy to within 0.1mm) and a period control with one microsecond accuracy. At the left end of the flume, a honeycomb structure was placed across the entire cross-section to avoid the influence of vortices created at the junction of the flume and the equilibrium chimney. The laser sheet measurement section was placed far enough from the transition between Perspex and PVC to ensure uniform flow characteristics at each phase.

Table 4.1 describes the different Re_w conditions for the three bed configurations: smooth bed; a smaller roughness bed (D_{50} = 1.5 mm, σ = 1.3) and a larger roughness bed (with D_{50} = 7.0 mm, σ = 1.2 mm)- for which velocity fields in the boundary layer were measured.

Table 4.1. Test conditions for both the smooth and rough cases.

	Test no.	T (s)	A (mm)	U_{0m} (mm/s)	Re_w (10^4)	Δ(ωt)	δ (mm)	$A/2.D_{50}$
Smooth	1	3.3	100	188	1.86	15º	2.2	-
	2	5	100	125	1.27	10º	2.8	-
	3	1.7	45.5	171	0.77	30º	1.6	-
	4	3.3	45.5	86	0.38	15º	2.2	-
Rough (D_{50}=1.5mm)	5	3.3	100	188	1.86	15º	3.6	33
	6	5	100	125	1.27	10º	3.0	33
	7	1.7	45.5	171	0.77	30º	2.0	15
	8	3.3	45.5	86	0.38	15º	1.8	15
Rough (D_{50}=7.0mm)	9	3.3	100	188	1.86	15º	8.0	7
	10	5	100	125	1.27	10º	8.6	7
	11	1.7	45.5	171	0.77	30º	2.0	3
	12	3.3	45.5	86	0.38	15º	2.8	3

Velocities were measured at the centerline of the tunnel using a PIV system consisting of a Gemini PIV Nd:YAG pulse laser from New Wave Research, and two 4 MPx, 12-bit frame-straddle CCD cameras from TSI Inc. The two cameras were set on opposite sides of the flume and offset so that the fields of view overlapped by 6.3 mm (Figure 4.2) to achieve a wide

streamwise field of view. Each camera was mounted to an aluminum frame and set at a distance 55 cm from the laser light sheet measurement plane. The combined field of view was 4 cm high and 8 cm long [wall-normal (*y*) by streamwise (*x*).]. The light sheet had a thickness of 0.5mm at the channel bottom, and was optimized with a cylindrical lens with a focal number of 15 mm and a spherical lens of 500 mm.

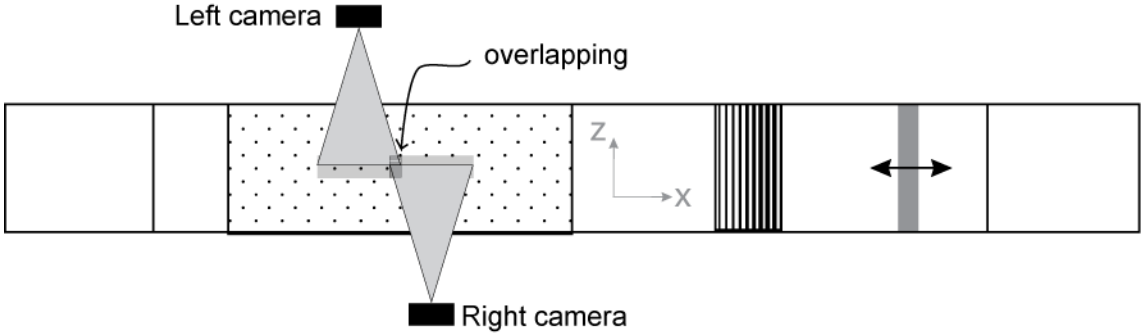

Figure 4.2. Top view sketch of the set up: cameras location. Two 4 Mpx CCD camera were used.

Table 4.1 summarizes all tests conditions analyzed for both the smooth and rough cases. U_{0m} represents the amplitude of the free stream velocity defined with

$$U_0(t) = -U_{0m}\cos(\omega t) \qquad (4.2)$$

including a negative value at $t = 0$, due to the free stream velocity initial motion from right to left in the field of view; $\omega = 2\pi/T$ represents the angular velocity of the oscillation. The definition of the boundary layer height from Sumer (1987), δ, is shown in Table 4.1.

Measurements were made at a sampling rate of 7.25 Hz, which was the maximum frequency allowed by the PIV system. Thus, the initial periods of oscillation considered (T = 5 sec, 3 sec, 2 sec) were adjusted proportionally to the sampling rate to exactly fit the number of phases recorded in a cycle. Therefore, each scenario has a number of recorded image-pairs proportional to 12 –which represents an increment in phase between samples of 10º when T=5.007sec, 15º when T=3.338sec and 30º when T=1.669-. Particles used as tracers were Spheriçel® hollow glass spheres of 11 µm mean diameter and a density of 1.1 g/cm^3 from Potter Industries Inc.. 60 cycles were recorded for each scenario, a number slightly higher than the proposed by Sleath (1987).

PIV analysis was conducted using the Insight 8 software from TSI Inc. The final interrogated area for all experimental runs was 16 x 16 px^2, which was constructed by applying a recursive Nyquist method to the original interrogation area of 64 × 64 px^2. Moreover, the final

interrogation area of 16×16 px^2 overlapped by 50%, yielding a vector grid spacing of 0.4 mm × 0.4 mm in each vector field. A local validation was performed between the recursive passes in order to clean initial bad vectors. Optimal displacement was obtained by using an FFT correlation engine. Final validation was done using 3 local median validations of different sizes, and two replacement steps for bad vectors, the last of which was performed using a smoothing window size of 3×3 px^2. The interrogation process was made separately for each camera image forwarded by a final merging of frames at the vector field level. The true vector field offsets was obtained with a simple matching code, which minimized the differences between the right and the left vector fields in the overlapping region. The final merging process consisted on a smooth transition between the two fields, thus avoiding any transition region in the middle of the composite field of view.

4.3 Coherent Structures

The analysis of the vector field obtained from the PIV interrogation process and the subsequent merging operation was followed by a phase averaging from a total amount of 60 cycles, as suggested by Sleath (1987):

$$\begin{aligned} U^i\left(x,y,\hat{t}\right) &= -U_m^i\left(x,y\right)\cos\left(\omega\hat{t}\right) \\ \bar{U}\left(x,y,\hat{t}\right) &= \frac{1}{60}\sum_{i=1}^{i=60} U^i\left(x,y,\hat{t}\right) \quad , \\ \bar{U}\left(x,y,\hat{t}\right) &= -U_m\left(x,y\right)\cos\left(\omega\hat{t}\right) \end{aligned} \tag{4.3}$$

at a fixed time $\hat{t}$, where the superscript i denotes the cycle, the subscript m is the maximum value of U, ω is the frequency of the oscillation, and the bar represents a phase averaged velocity. Turbulent quantities were first computed for each fluctuation field and then averaged over the 60 cycles as detailed:

$$\overline{u'v'}\left(x,y,t\right) = \frac{1}{60}\sum_{i=1}^{60}\left[\left(U^i\left(x,y,t\right)-\bar{U}\left(x,y,t\right)\right)\times\left(V^i\left(x,y,t\right)-\bar{V}\left(x,y,t\right)\right)\right] \tag{4.4}$$

The variable used to visualize the coherent structures is the swirling strength, λ_{ci}^2, -Zhou et al. (1999)- where λ_{ci} is defined as the imaginary part of the complex eigenvalue of the local velocity gradient tensor $\underline{D}$

$$\underline{D} = \begin{bmatrix} \frac{\partial u}{\partial x} & \frac{\partial u}{\partial y} \\ \frac{\partial v}{\partial x} & \frac{\partial v}{\partial y} \end{bmatrix}, \tag{4.5}$$

confirmed by Adrian et al. (2000) as one of the best variables for identifying not only the existence but the position of the structure. An example is provided in Figure 4.3, where four different variables are plotted together with the velocity field in a zoomed view of Test no. 6. The selected phase, $\omega t = 70º$, is when the flow reversal close to the wall takes place, and a vortex is detected. Vorticity, $\Omega = \nabla \times \vec{u}$, is clearly showing the vortex, and so is the swirling strength. This is not the case for the Reynolds stresses and also the Turbulent Kinetic Energy (TKE), $TKE = \left[\frac{1}{2}\left(\overline{u'^2} + \overline{v'^2}\right)\right]^{1/2}$, which show other zones with higher values than those seen at the center of the vortex.

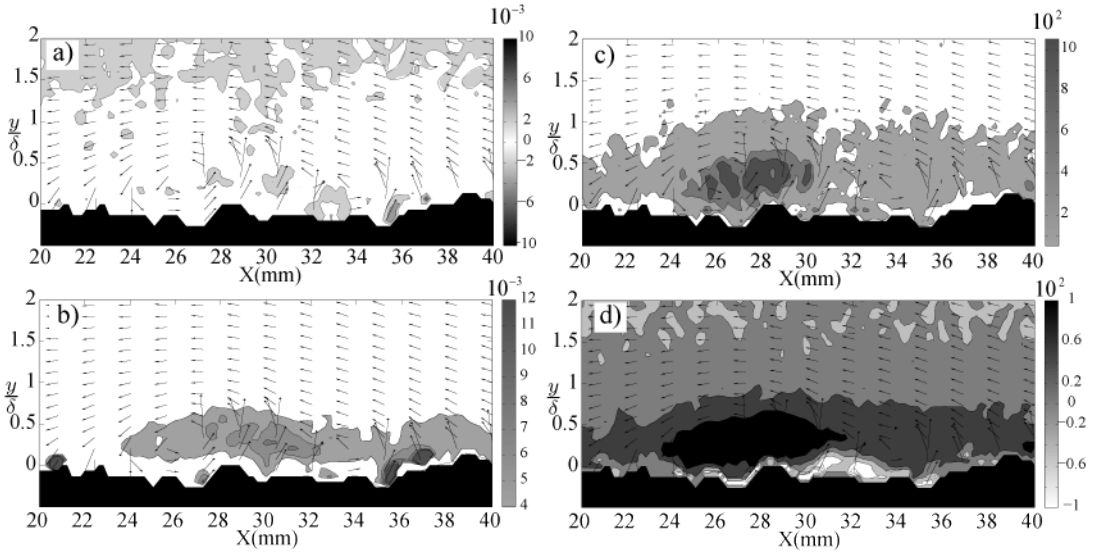

Figure 4.3. Close view of a snapshot took at Exp. No.6 at the phase $\omega t = 70º$. Background variable: a) $\frac{\overline{u'v'}}{U_{0m}^2}$; b) $\frac{\overline{u'^2+v'^2}}{U_{0m}^2}$; c) $T^2\overline{\lambda_{ci}^2}$; d) $T\bar{\Omega}$

Figure 4.4 defines all the flow regimes studied herein after Kamphuis (1975). Smooth wall experiments fall close to the line dividing the laminar and turbulent regime. Although the limits between regimes are not always exact, velocity profiles show how Tests nos. 3 and 4 may be considered in the laminar regime whereas Tests nos. 1 and 2 can be defined as flows in the laminar-to-turbulent transition zone. Scenarios tested with the smaller roughness configuration, are clearly within the smooth-to-rough transition zone. Finally larger roughness scenarios fall in the rough turbulent regime but in a region very close to the transition zone, suggesting that most

of the phases are within the transition zone with only a few of them extending into the rough turbulent regime. A detailed discussion of the flow regime definition can be found in Chapter 3.

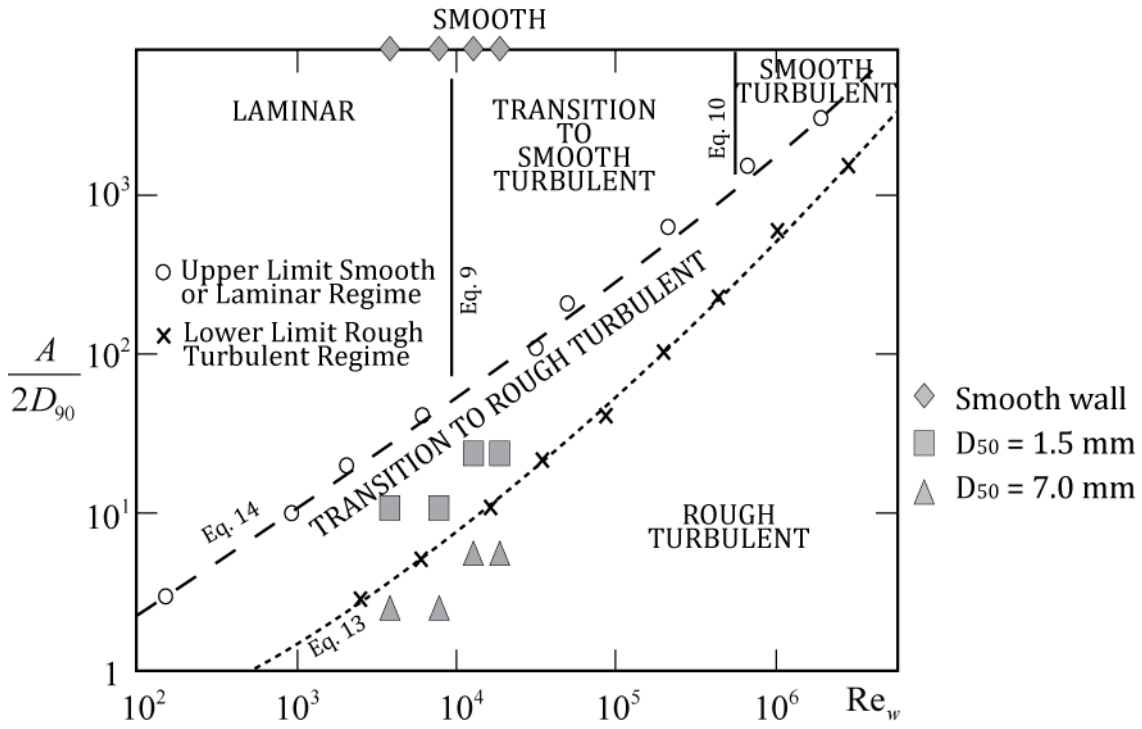

Figure 4.4. Diagram defining the flow regime, from Kamphuis (1975). Smooth wall experiments are close to the Re_w dividing the laminar and the transition regime. Smaller roughness bed experiments are within the transition to rough turbulent and finally larger roughness bed scenarios fall close to the division between the latter regime and the rough turbulent.

The previous definitions of the flow regime will therefore condition the existence of the coherent structures detailed below and found in the experiments. It is important to recall that the study was done using a 2D PIV system and so no 3D phenomenon will be described. Only one signature found within the smooth wall experiments, and characterized by Carstensen et al. (2010) will be assumed as a 2D representation of a 3D structure.

4.3.1 Smooth Wall

Carstensen et al. (2010) defined two different coherent structures for oscillatory flows over smooth wall beds: vortex tubes ($7 \times 10^4 \leq Re_w \leq 3 \times 10^5$) and turbulent bursts ($Re_w \geq 1.5 \times 10^5$). However, the ranges of Re_w used in our research are below the limits described by Carstensen et al. (2010) for both structures. However, streamwise averaged turbulent intensities plotted in Figure 4.5, show the existence of turbulence indicating certain structures are likely present. In fact, such turbulence has its minimum value at the middle stages of the deceleration

phase ($\omega t = 60º$), immediately before the flow reversal close to the wall. Maximum values are obtained at the end of the acceleration phase and the beginning of deceleration cycle.

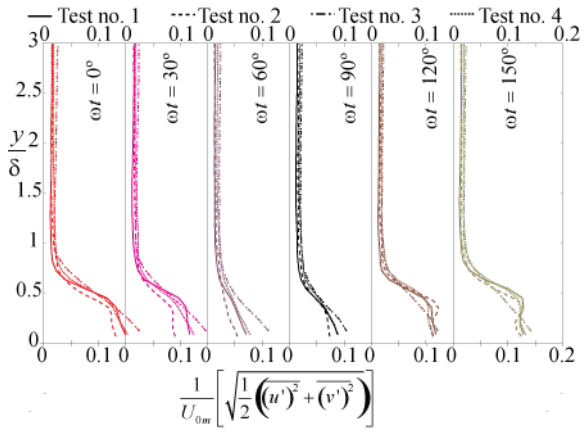

Figure 4.5. Representation of the turbulent intensities addition in smooth wall experiments.

Carstensen et al. (2010) did not detect any streamwise vortices formed by streaks, as the ones described by Vittori & Verzicco (1998) in their simulation of a flat wall with imperfections. Thus, regardless of the limitations we have with a 2D PIV analysis, structures found herein are considered to be closer to the vortex tubes, and therefore 2D structures.

The snapshots presented in Figure 4.6, show the existence of structures below δ, exactly the height below which turbulence is present. In fact, the maximum turbulence intensities from Figure 4.5 exist at the same height as the center of the structures shown in Figure 4.6. On the other hand, the maximum intensity in the structures is found at the early stages of the deceleration process, (Figure 4.5). The turbulence described in Figure 4.5 is henceforth assumed to originate from the structures shown in Figure 4.6.

Figure 4.6 (d) shows how vortices appear during the flow reversal close to the wall - $\omega t = 60º \sim 90º$-. According to several authors (e.g. Akhavan et al. (1991b), Carstensen et al. (2010), and Mazzuoli et al. (2011)) the triggering of turbulence is due to small imperfections in the wall and the secondary modes present in the flow as a result of the experimental setup. However, only Kelvin-Helmholtz instability explains the formation of vortices when the flow reversal close to the wall takes place, as suggested by Carstensen et al. (2010).

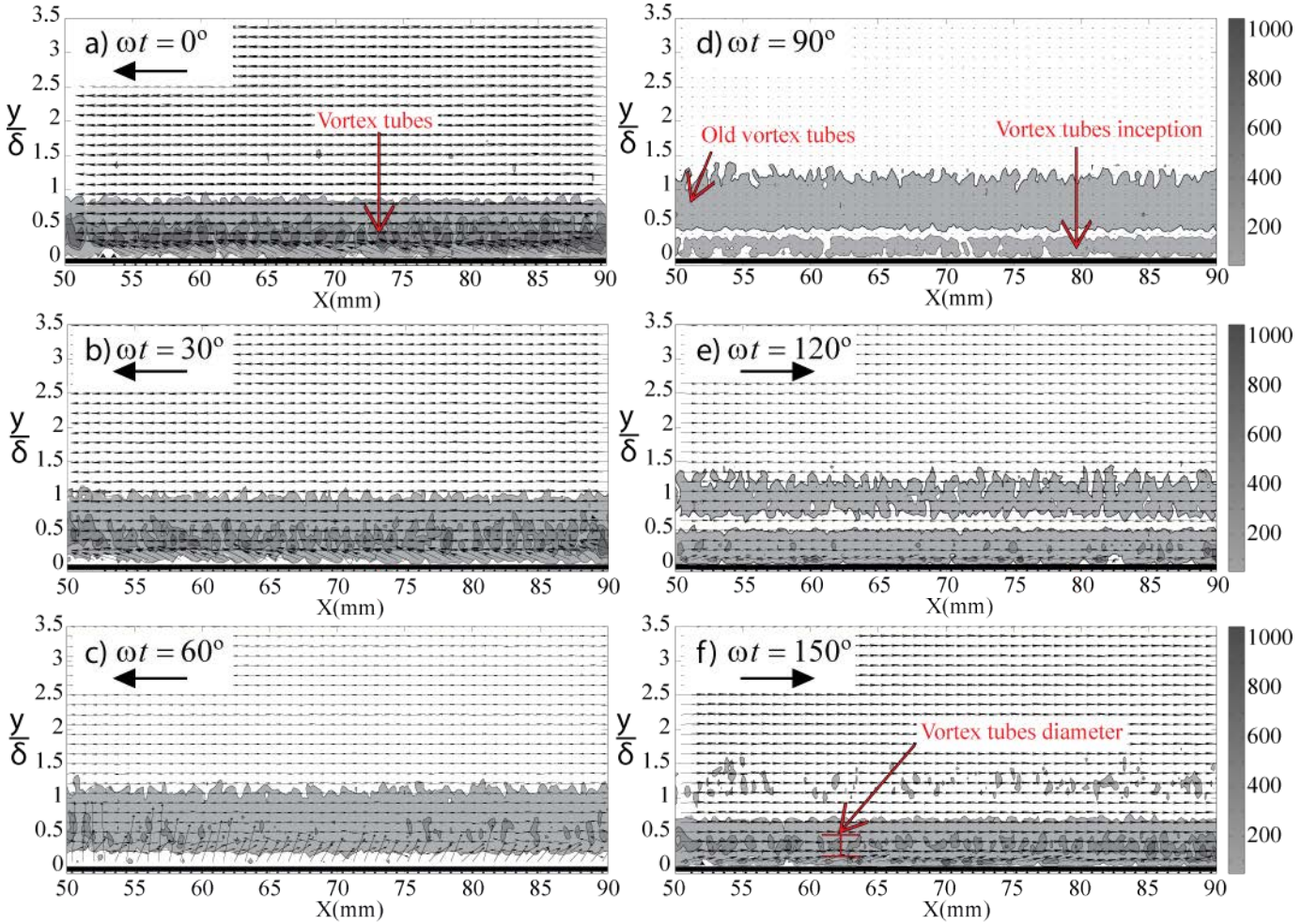

Figure 4.6. Time evolution of the non-dimensional Swirling strength $(T^2\lambda_{ci}^2)$. Test no. 2, smooth wall $Re_w = 1.27 \times 10^4$. Half cycle. Arrows represent the direction of the free stream flow (no arrow represents the free stream flow reversal).

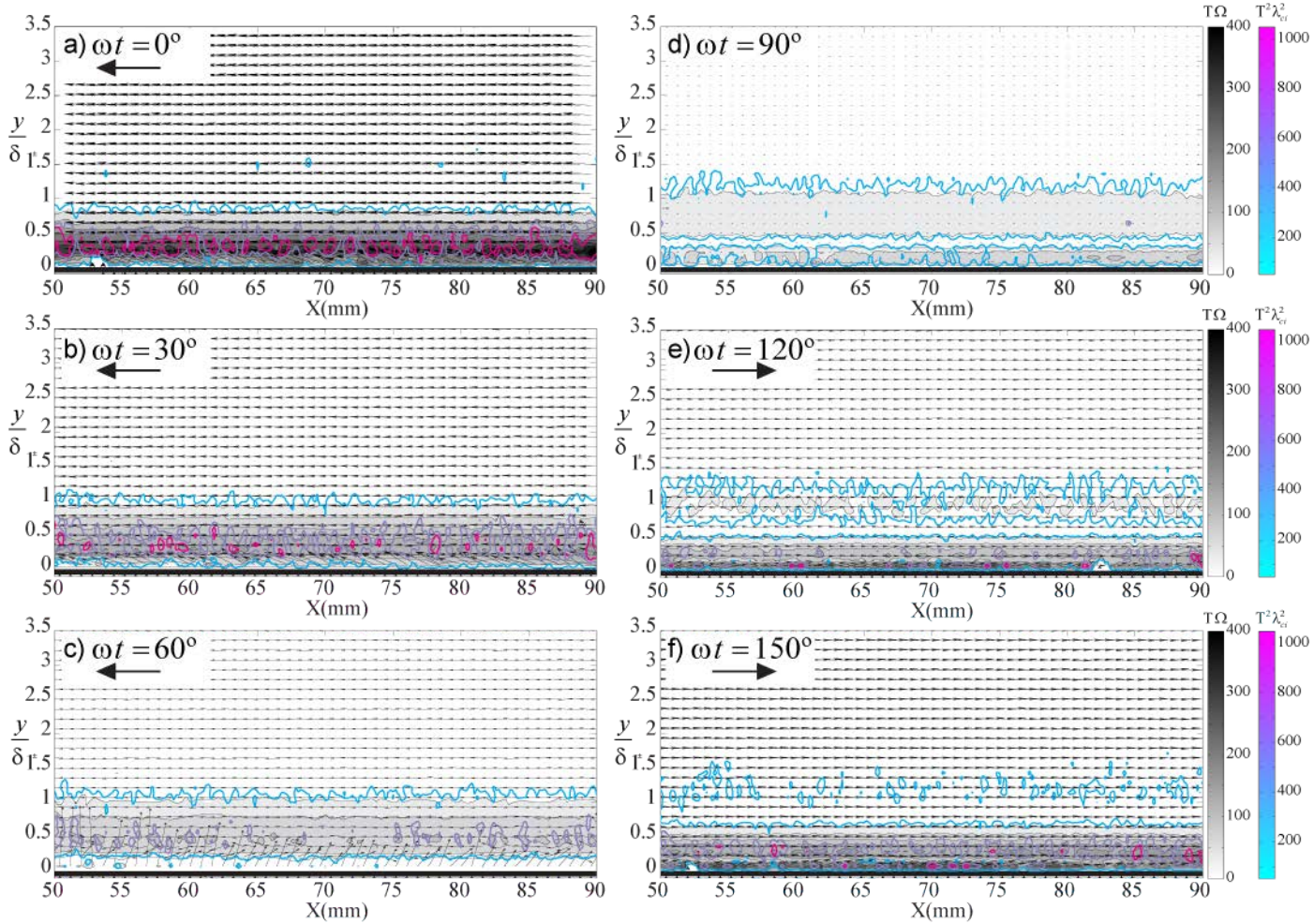

Figure 4.7. Time evolution of the correlation between non-dimensional vorticity $(T|\Omega|)$ –background variable- and the non-dimensional swirling strength $(T^2\lambda_{ci}^2)$ – contour variable-. Test no. 2, smooth wall $Re_w = 1.27 \times 10^4$. Half cycle. Arrows represent the direction of the free stream flow (no arrow represents the free stream flow reversal).

Snapshots of vorticity plotted in Figure 4.7 along with Figure 4.6 are helpful in describing the formation and evolution of the vortex tubes. In Figure 4.7 inception of small vortices occurs during the flow reversal close to the wall. Thereafter, at the beginning of the acceleration phases, vortices increase their size and vorticity but without any motion in the streamwise direction. If the Kelvin-Helmholtz instability is assumed to be the phenomenon creating the vortices, then the position of the shear-stress inflectional point determines the center of these vortices. The streamwise velocity profile for laminar oscillatory flow over smooth beds:

$$U_0(y,t) = -U_{0m}\left[\cos(\omega t) - e^{\delta_1 y}\cos(\omega t - \delta_1 y)\right] \qquad (4.6)$$

predicts how the shear-stress inflectional point moves upwards with time, thus explaining the vertical motion of the center of the vortex and also their growth in diameter. At early stages of the acceleration process vortices increase rapidly in diameter and move with the flow close to the wall. In the laminar regime, the inflectional point moves upwards with constant velocity. This is only the case of Test nos. 3 and 4, which are considered to be in the laminar regime (Figure 4.4), thus confirming that Tests nos.1 and 2 are in the laminar-to-turbulent regime.

At this stage is worthwhile to recall that structures present in Figure 4.6 and Figure 4.7 from (a-c) come from the previous half cycle. Thus a complete cycle of the structures originating from vortex tubes is still represented with the snapshots plotted in both figures. Vortices created close to the wall after $\omega t = 60º$ continue growing beyond $\omega t = 150º$ similar to the vortex tubes shown in Figure 4.6 (a) and (b). Therefore, at the inception stage, vortices created during the previous half cycle with opposite vorticity occur above the elevation at which new vortices form. Although this change in sign is not visible in Figure 4.7, the streamwise phase averaged shear stresses, plotted in Figure 4.8, show this phenomenon. In this figure, two peaks in shear stress of opposing sign are present at different elevations for the interval $90º < \omega t < 150º$.At $\omega t = 60º$ shear stresses close to the wall are negligible and start growing with positive sign; afterwards two clear peaks form in the vertical profile, one close to the wall and the second one higher in the flow, $y/\delta \approx 0.75$. At later stages, both peaks rise in the vertical. However, the peak located far from the wall is gradually smoothed until it disappears, whereas the one close to the boundary becomes sharper. Figure 4.8 shows the evolution (sharpening) of the first peak in the phases $0º < \omega t < 60º$, which later becomes the second peak.

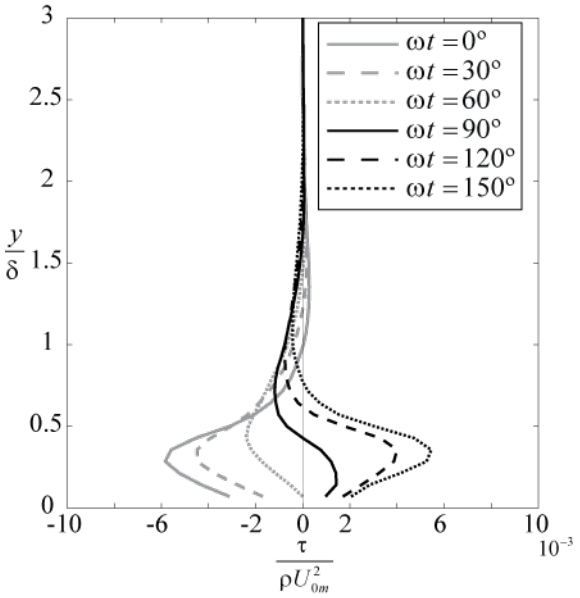

Figure 4.8. Total shear stresses –streamwise averaged- profiles from Test no. 2, smooth wall $Re_w = 1.27 \times 10^4$. Half cycle.

Figure 4.9 shows a comparison between 2D plots of the swirling strength and vertical profiles of the streamwise shear stresses. Both peaks in shear stress correspond exactly with the centers of longitudinal vortex tubes. This confirms that the Kelvin-Helmholtz instability is responsible for the formation of vortex tubes. Shear stresses in the smooth wall experiments are mainly composed of viscous stresses, which in turn show a vertical gradient of horizontal velocity. Moreover, the height with zero shear stresses coincides with the division between new structures and the "old" vortices crated during the previous half cycle.

Carstensen et al. (2010) describes how vortex tubes inception occurs prior to the free stream flow reversal ($\omega t = 60º$) and they last less than a quarter of a cycle. However, Figure 4.6, Figure 4.7 and Figure 4.9, show the existence of certain structures originating from previous vortices. This difference may be the result of dye used in Carstensen et al. (2010), which is helpful to visualize the structures but may have become diluted before the structure was effectively dissipated. Then the whole cycle of vortex tubes created close to the wall at the latter stages of the deceleration phases lasts three quarters of a cycle. Moreover, during the acceleration process two different structures are present: 1) the recently created vortex tubes; 2) an amorphous feature arising from the merging of the vortex tubes. The merging process takes place when the flow starts the reversal close to the wall and forces the present vortices to move upwards, Figure 4.6 (c). This is even clearer if Figure 4.6, Figure 4.7 and Figure 4.9 are observed carefully: the intensity of structures increases and reaches its maximum value at the maximum free stream velocity phase.

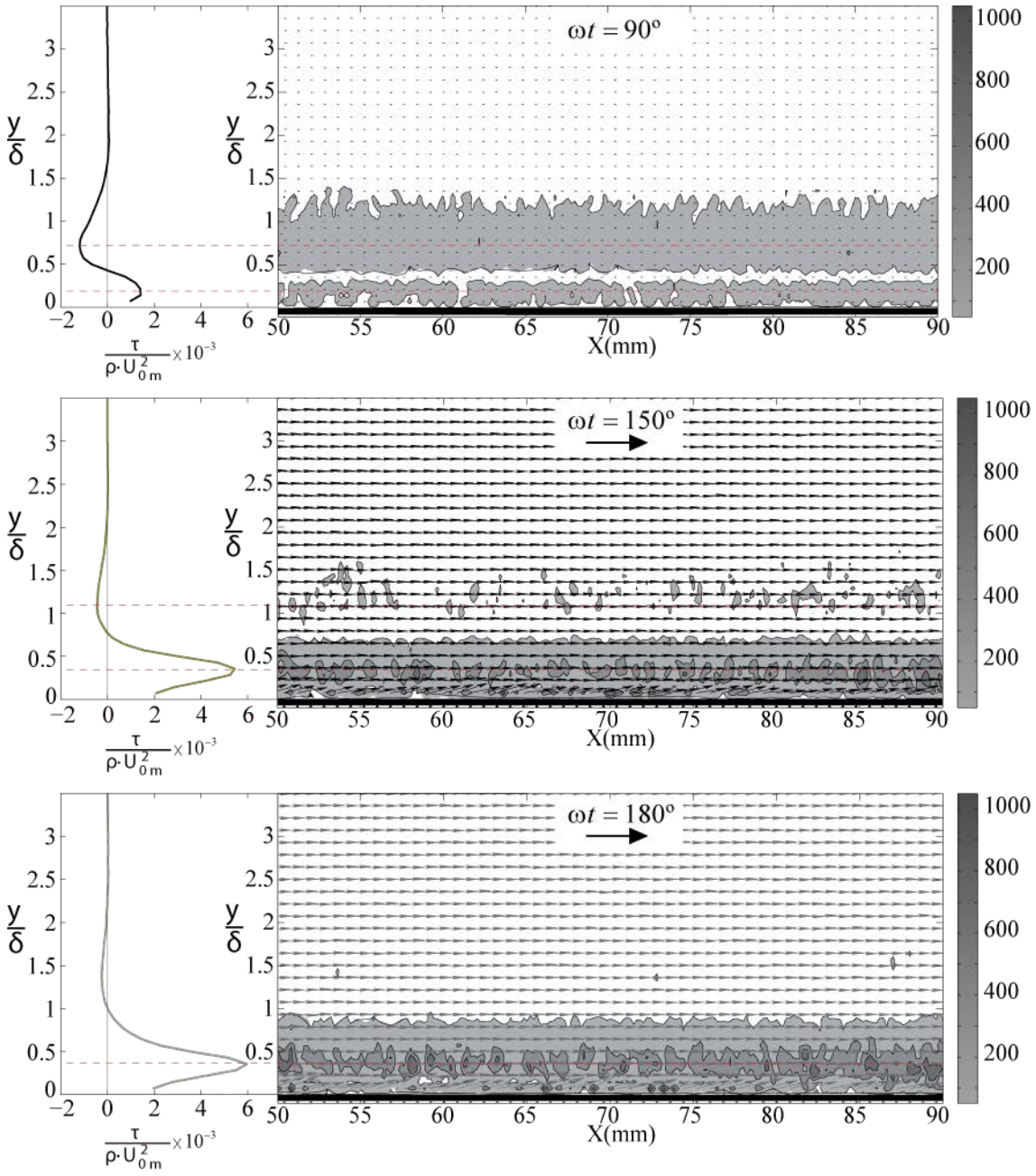

Figure 4.9. Combination of streamwise averaged shear stresses –left column-, and snapshots of velocity field with $T^2\lambda_{ci}^2$–background variable-. Test no. 2, smooth wall $Re_w = 1.27 \times 10^4$. Half cycle. Arrows represent the direction of the free stream flow.

4.3.2 Rough Wall

Few studies are directed towards the definition of structures in rough wall oscillatory boundary layers. The first experimental work of Keiller & Sleath (1976) focused on regular rough surfaces using semispheres. This was later reproduced numerically by Fornarelli & Vittori (2009) who also compared their results to another experimental work carried out using square roughness elements Krstic & Fernando (2001). Sleath (1987) and Jensen et al. (1989) detailed

the existence of jets of fluids coming off of the irregular sediment bed, indicating the possibility of some structures being created close to the wall and being ejected during the oscillatory motion.

One recent experimental study published by describes the existence of turbulent spots in the range $5 \times 10^4 < Re_w < 1 \times 10^5$ building off of their original work in smooth wall oscillatory boundary layers Carstensen et al. (2010). The lower boundary limit of this range is slightly higher than in this study. However, the ratio A/k_s is not discussed in Carstensen et al. (2012) and may play a role on defining this range since some structures similar to turbulent spots are also detected and will be further described. Another main difference between Carstensen et al. (2012) experiments and the experiments described herein is that their structures were studied with a steady increase of the velocity amplitude.

Observations in two different irregular rough beds showed three kinds of coherent structures:

(i) Vortices: Structures created during the wall flow reversal that are ejected as vortices and ultimately become bursts.

(ii) Turbulent spots: Structures that emerge like vortices during the flow reversal at the wall but are not strong enough to maintain coherence. These structures are ejected as bursts and reach lower heights than vortices (i). They will be named indistinctly turbulent spots or bursts.

(iii) Shear layers: These features were only detected in experiments with $A/2D_{50} < 15$, and consist of several vortices shed continuously from a particular grain. At the wall flow reversal stages, vortices (i) are formed at the same place from the remaining structure of the shear layer.

Vortices

An example of a vortex is plotted in Figure 4.10, in which three different variables are used as tracers: swirling strength, λ_{ci}^2, total shear stress, $\tau = \tau_v + \tau_{Re}$, and TKE. As suggested by Adrian et al. (2000), swirling strength is found to be the best tracer, particularly because swirling strength defines both the shape and the location of the vortex center. Vorticies are formed during the wall flow reversal stage similar to the smooth wall scenario, but the location appears to be set by grain position. This suggests the position of vortices is controlled by the distribution of bed roughness. In other studies like Fornarelli & Vittori (2009) with regular rough walls, vortices were formed behind all semispheres, also during the wall flow reversal. Another interesting

characteristic shown in Figure 4.10 is the shear stress and TKE peak location - right of the vortex center. Recalling that in Figure 4.10, flow close to the wall has already reversed going from left to right and that the represented phase is at the end stages of the deceleration process, the shear stress and the TKE peak are located exactly at the same place upstream the peak location of the vortex. This excess is responsible of the latter shed of the vortex from the wall.

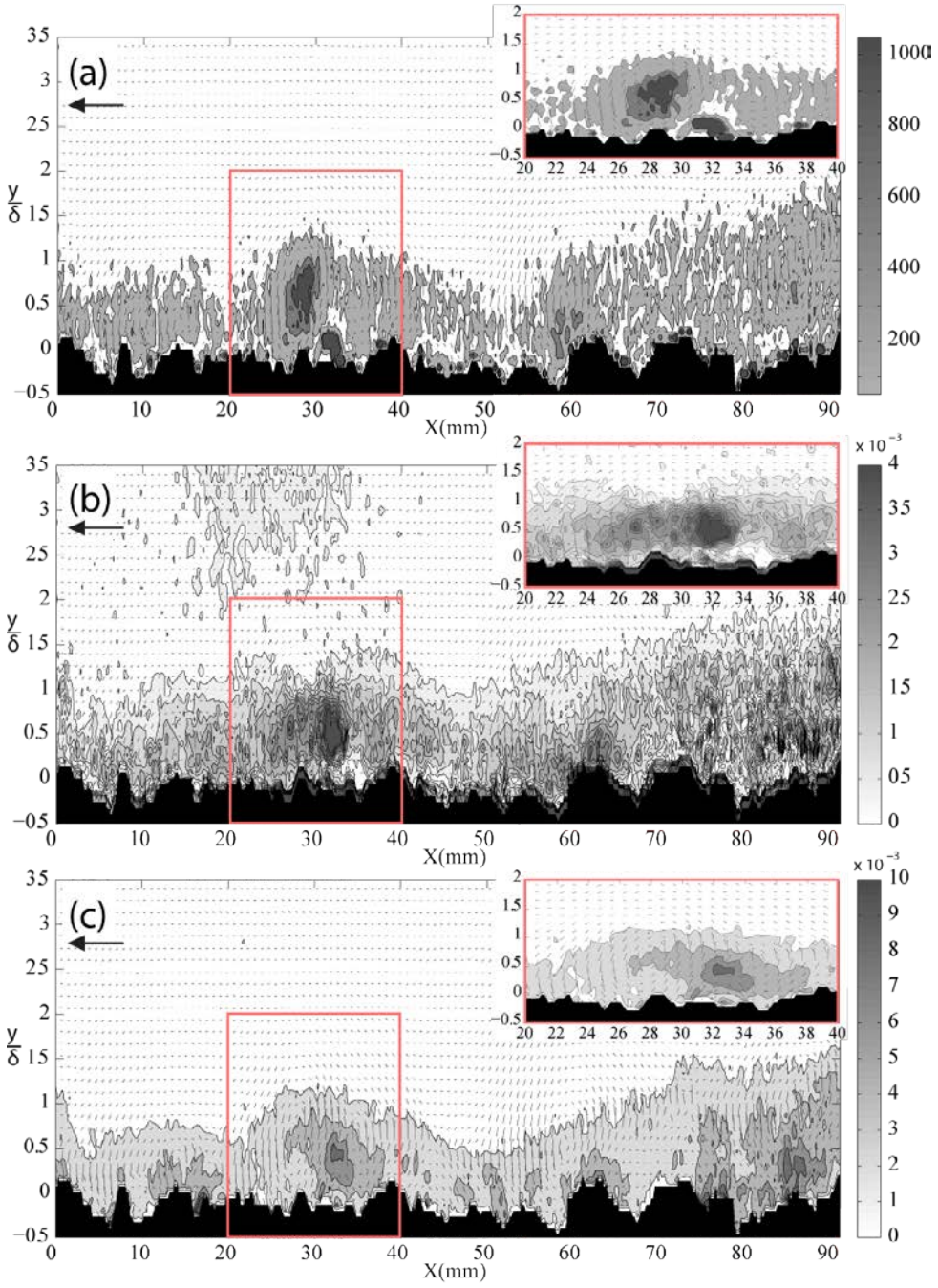

Figure 4.10. Detail of the formation of a vortex. Test no. 6; roughness: $D_{50} = 1.5mm$; $Re_w = 1.27 \times 10^4$. Phase: $\omega t = 80º$. (a) Background variable: $\lambda_{ci}^2 T^2$; (b) Background variable: $\tau/\rho U_{0m}^2$; (c) Background variable: TKE/U_{0m}^2.

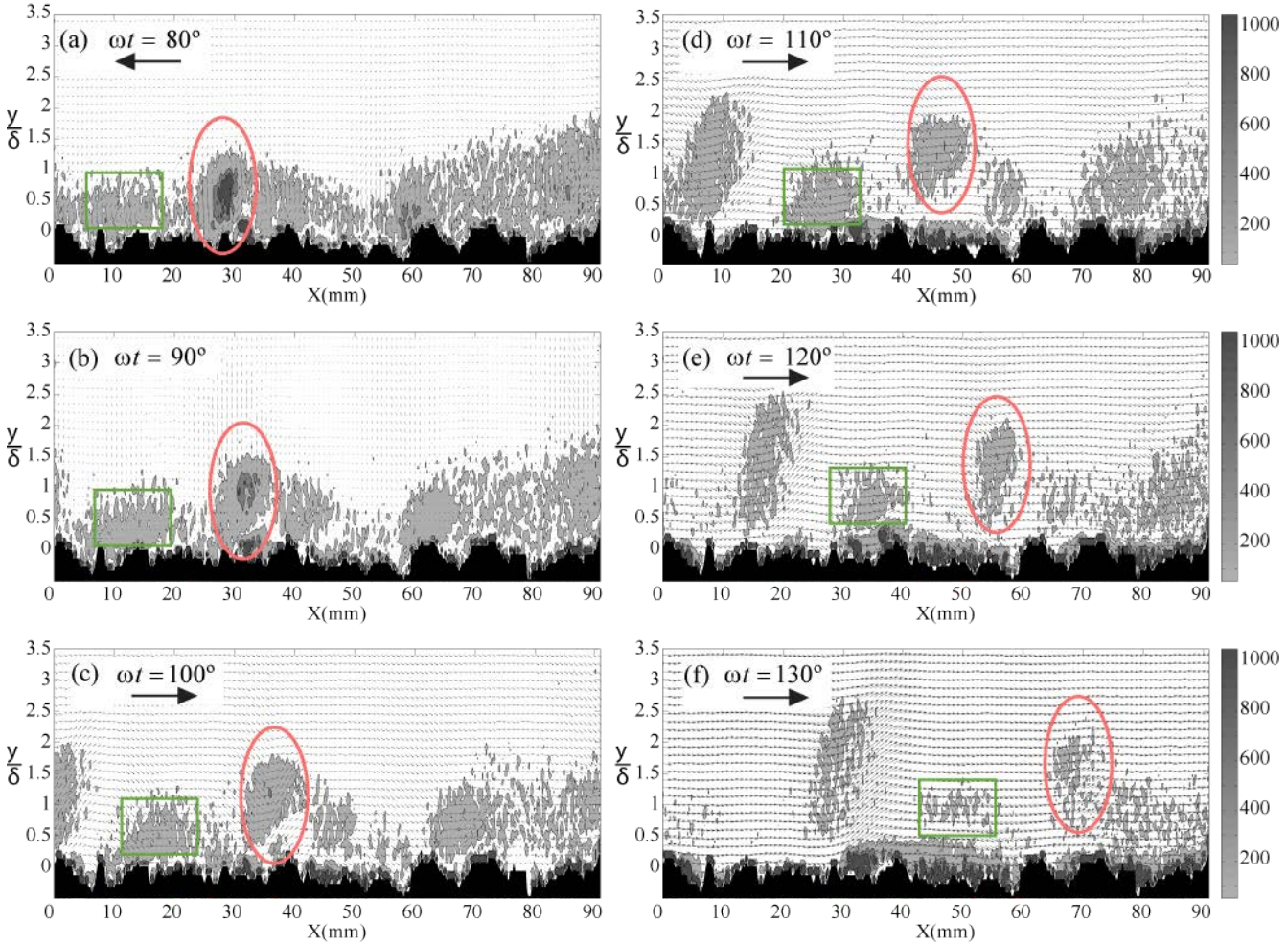

Figure 4.11. Time evolution of the position of a vortex, ellipse, and a turbulent burst, rectangle, created during the wall flow reversal $\omega t = 70^{o}$. Background variable: $T^2\lambda_{ci}^2$. Test no. 6; roughness: $D_{50} = 1.5mm$; $Re_w = 1.27 \times 10^4$. Arrows represent the direction of the free stream flow (no arrow represents the free stream flow reversal).

Figure 4.11 shows the time evolution of the same vortex plotted in Figure 4.10 from its shedding point. It is important to point out that the vortex shown either in Figure 4.10 and Figure 4.11 was actually created at the previous phase of $\omega t = 70º$. It can be clearly seen how the structure of the vortex is maintained only until $\omega t \sim 90º$; after that, although still present, the vortex breaks up and the signature is transported with the flow as a burst until it disappears. Other structures also present in Figure 4.11 are described as bursts because they were not originally created from defined vortices.

Results shown so far coincide with some of the numerical work published by Fornarelli & Vittori (2009). The vortex is formed behind the sediment grain where pressure is minimum during the wall flow reversal, but pressure gradients are higher. Krstic & Fernando (2001) described a dipole-like vortex formed during the wall flow reversal which was not detected in any of the scenarios presented herein. This may be due to the shape of the roughness used by Krstic & Fernando (2001) which may have led to the formation of a second vortex after the first vortex was formed. In fact, the shedding process of the dipole-like vortices described by Krstic & Fernando (2001), coincides with the one shown in Figure 4.11 in which vortices are elongated while propelling from the wall. Vorticies were present in all the experiments but their trajectories did not differ from the one described for Test no. 6.

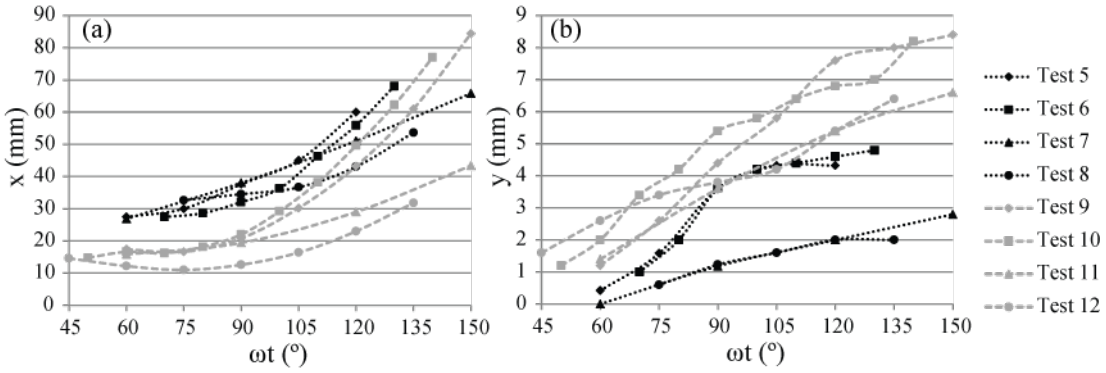

Figure 4.12. Time evolution of the center of one vortex in all experiments. (a) Horizontal position; (b) Dimensional vertical position. Black lines: small roughness scenarios; gray lines: large roughness scenarios.

Figure 4.12 plots the time evolution of the center of the vortex, being defined as the middle point of the zone with constant swirling strength ($T \times \lambda^2 \geq 50$). In general terms, larger roughness scenarios have longer lived vortices-bursts. Clear distinctions can be seen for different bed scenarios, but among all tests, there is similarity in those curves belonging to tests with the same A/k_s ratio (Test no.5 and Test no.6; Test no. 7 and Test no. 8). Looking carefully at the horizontal displacement, Figure 4.12 (a), higher velocities at latter stages are found in tests with

higher amplitude regardless of the roughness size of the bed. This is because the real vertical position of the vortices is higher and so mean velocity profiles are also higher. The evolution of the vertical position (Figure 4.12 b) shows an inflectional point close to the free stream flow reversal stages - indicating that the detachment from the wall was complete. This is clearer for higher amplitude experiments with a small roughness bed size. The evolution of the vertical position combined with the horizontal displacement, shows that higher horizontal velocities are reached once the detachment finished. It is interesting to see the good collapse for small roughness scenarios when plotting the dimensional vertical position evolution, between tests with the same amplitude. The dependence on the vortex horizontal and vertical position evolution with the amplitude, Figure 4.12 (b), and of course the roughness size, shows that these two variables can be defined as characteristic lengths of the flow.

Turbulent Spots

The turbulent spots are defined according to the description already given by Carstensen et al. (2012). These are 3D structures randomly located in the plan view that occur close to the wall flow reversal. In particular, for smooth wall flows, Carstensen et al. (2010) indicates that turbulent spots first occur during the bed shear stress reversal. Then they grow in size and eventually merge. Spikes on the shear stress signal were detected when the turbulent spot passes a hot film probe. However, Carstensen et al. (2010) and Carstensen et al. (2012) based their description only in plan view videos and a hot-film probe. Mazzuoli et al. (2011) performed 3D numerical simulations and turbulent spots in oscillatory flow over smooth beds are also described in the vertical plane. Based on previous descriptions, the structures detected in this research have been found to present similar characteristics in the vertical plane as the ones described by Mazzuoli et al. (2011) for smooth wall experiments, although no information of the plan view was recorded.

Figure 4.11 follows the trajectory of a burst compared to the vortex trajectory. The first difference between turbulent spots and vortices described in the previous section is the consistency of the vortex itself. That is, spots may be created as vortices but the coherence of the vortex is lost immediately even before the structure is detached from the wall. Also some of the turbulent spots are not born as a clear vortex but rather as a burst. Another difference shown in Figure 4.11 is the height reached by turbulent spots once they have been shed from the wall. Snapshot plotted in Figure 4.11 (d) shows the existence of three vortices moving at a central height of about $y/\delta \sim 1$ and two spots at a height $y/\delta \sim 0.5$. The location of turbulent spots between vortices is thought to be random. Other scenarios do not show this pattern which is

related both to the configuration of the gravel bed and the flow regime of the flux. It is important to recall that experiments done with the small roughness sediment bed have been characterized as flows in the laminar-to-turbulent transition, and that flows within the larger roughness are in the rough turbulent regime but very close to the laminar-to-turbulent transition zone. Therefore, none of the flows are fully rough when turbulent spots and vortices are created during the wall flow reversal, and so bed roughness configuration has a major influence on the location of the structures.

Figure 4.13 and Figure 4.14 show the same snapshots as Figure 4.11 detailing the position of the vortices and the turbulent spots along a quarter of a cycle where both are incipient, shed from the wall and move solidary with the flow. From Figure 4.13, where the distribution of total shear stresses is shown, another difference between vortices and turbulent spots can be deduced: vortices are also created from Kelvin-Helmholtz type instabilities, because high peaks of shear stresses are placed near the center of the vortex – particularly at the early stages of inception. On the other hand, no high gradients of velocity are detected near the locations of turbulent spots. In addition, shear stresses higher values disappear after $\omega t = 110º$ which coincides with the time vortices lose their shape and start behaving as bursts (see Figure 4.11). In Figure 4.14 TKE is plotted as the background variable showing how vortices concentrate maximum values at the right-hand-side of the center of the vortex. Likewise, turbulent spots have higher values of TKE in their heads. However, the highest values of TKE are found in the places where vortices are located showing that these features concentrate larger amount of turbulence which, in turn, adds to their lifespan. This last comparison is one of the other main differences between turbulent spots and vortices: the levels of turbulence are higher in vortex structures and last longer than for turbulent spots.

Shear Layers

These are signatures only present when the median grain diameter used in the rough wall was $D_{50} = 7.0mm$ (Test nos. 9, 10, 11 and 12). They have also been found to be related to vortices and turbulent spots which may indicate that, although not visible in the swirling strength snapshots of smaller roughness experiments, they can also be present under smaller roughness scenarios.

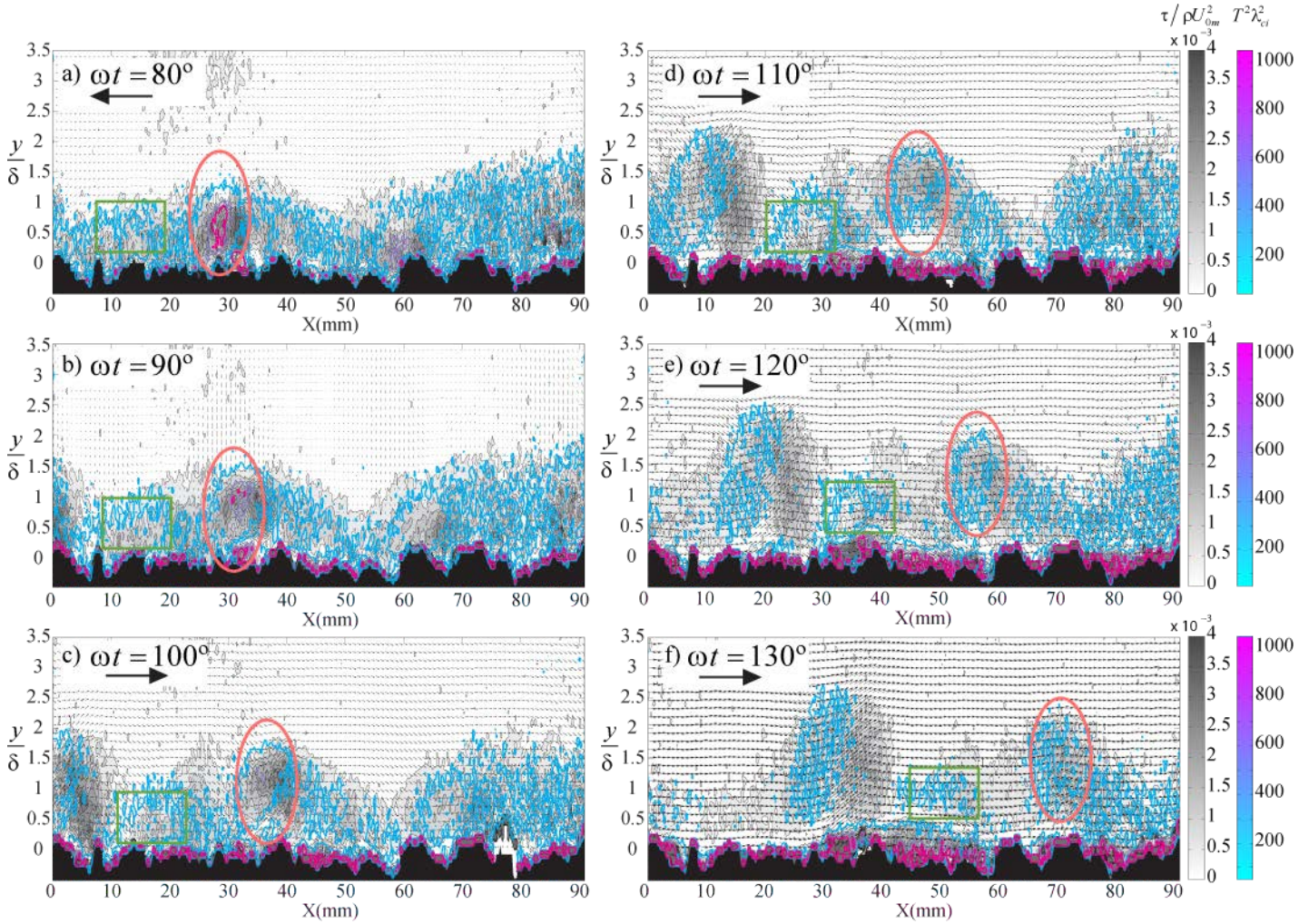

Figure 4.13. Time evolution of the position of a vortex, ellipse, and a turbulent spot, rectangle. Bacground variable $(\tau_v + \tau_{Re})/\rho U_{0m}^2$; contour variable: $T^2\lambda_{ci}^2$. Test no. 6; roughness: $D_{50} = 1.5mm$; $Re_w = 1.27 \times 10^4$. Arrows represent the direction of the free stream flow (no arrow represents the free stream flow reversal).

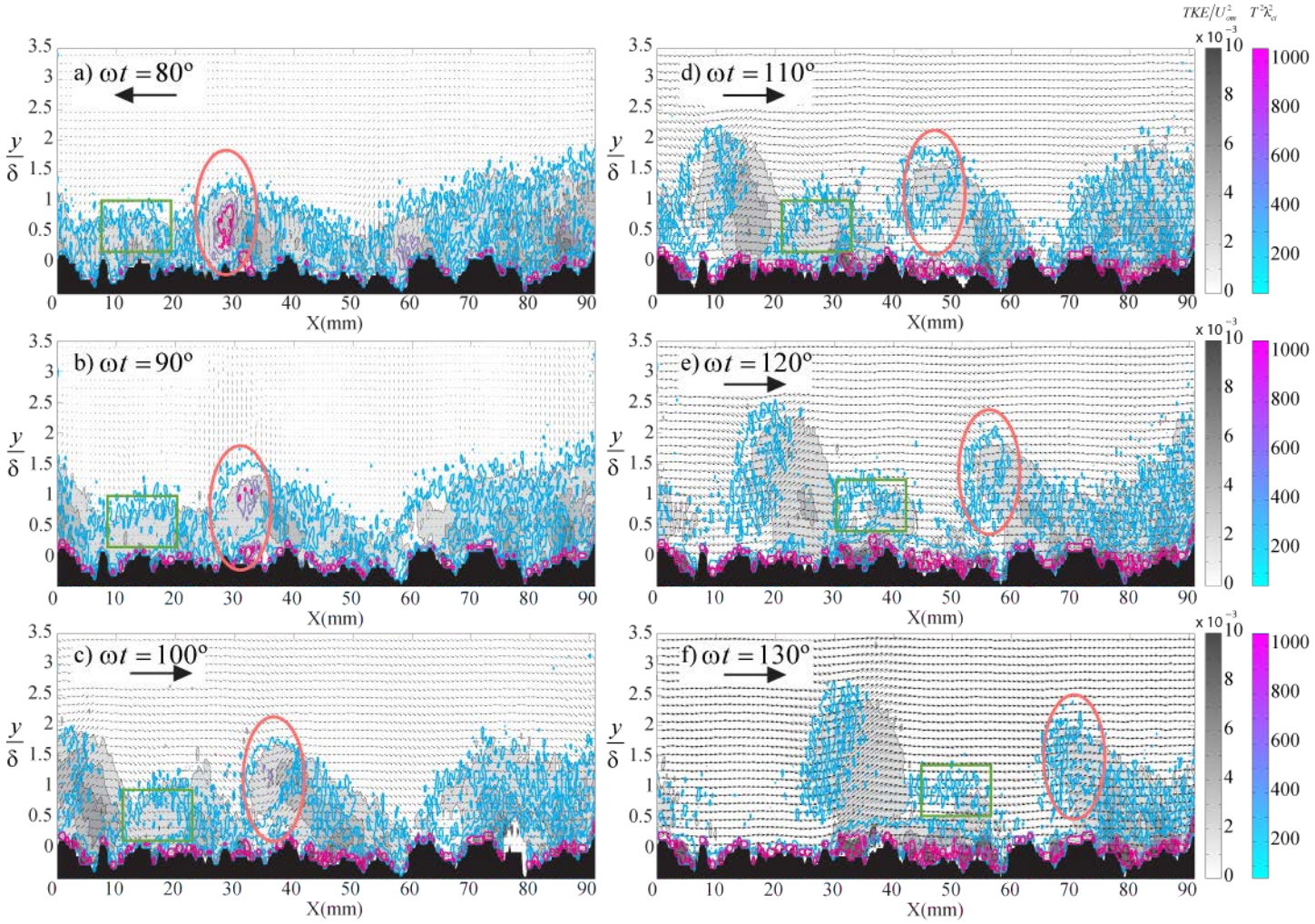

Figure 4.14. Time evolution of the position of a vortex ring, ellipse, and a turbulent spot, rectangle. Bacground variable TKE/U_{0m}^2. contour variable: $T^2\lambda_{ci}^2$. Test no. 6; roughness: $D_{50} = 1.5mm$; $Re_w = 1.27 \times 10^4$. Arrows represent the direction of the free stream flow (no arrow represents the free stream flow reversal).

Shear layers consist on a sequence of vortices shed from the wall in particular grains. This is observed in Figure 4.15 (a) where a shear layer is formed at a location $x{\sim}25\ mm$. This signature is linked to vortices described in section 4.3.2(i) through the deceleration process -Figure 4.15 (a), (b) and (c)-, in which the angle of the shear layer increases up until a moment where the wall flow reversal occurs. At this moment the vortex is formed with the remaining turbulence from the shear layer and shed from the wall at latter phases (Figure 4.15 d). Simultaneously, another shear layer forms off of another grain with an opposite sense direction and grows continuously until the maximum free stream velocity phases. During the acceleration process, shear layer grows in size instead of increasing the angle because at early stages of initiation, no significant angle can be found.

It is not completely clear if shear layer shown in Figure 4.15 (a) formed only from one grains. In Figure 4.16 (a zoomed view of Figure 4.15 (a)) shear layers previously described seems to originate from more than one grain of sediment. In fact, when looking at previous stages in detail ($\omega t < 0º$) (Figure 4.17) the shear layer is formed from one grain at early stages of the acceleration quarter cycle when the flow is defined as instantaneously laminar at this phase –symmetric to snapshot shown in Figure 4.15 (d). Then as the free stream flow and near wall velocity increase, the shear layer covers the grain reaching the next grain similar to Figure 4.15 (e). Thereafter, once wall velocity has increased, the shear layer detaches from the wall at the second grain (Figure 4.17 a) as a vortex. In Figure 4.17 (b) the boundary layer formed in the original grain, is detached but does not have energy enough to shed from the wall until it reaches a third grain in Figure 4.17 (c). Finally when the free stream flow the shear layer becomes stable without any waviness and is formed of several vortices from different grains although the boundary layer detaches originally from one grain. Other tests showed the same behavior on the initiation and development of the shear layer –see Figure 4.18-. Moreover, higher Reynolds number scenarios showed a complete development of the shear layer at previous phases.

The evolution of the turbulent stresses is shown in Figure 4.18 helps illustrate the behavior of shear layer signatures.

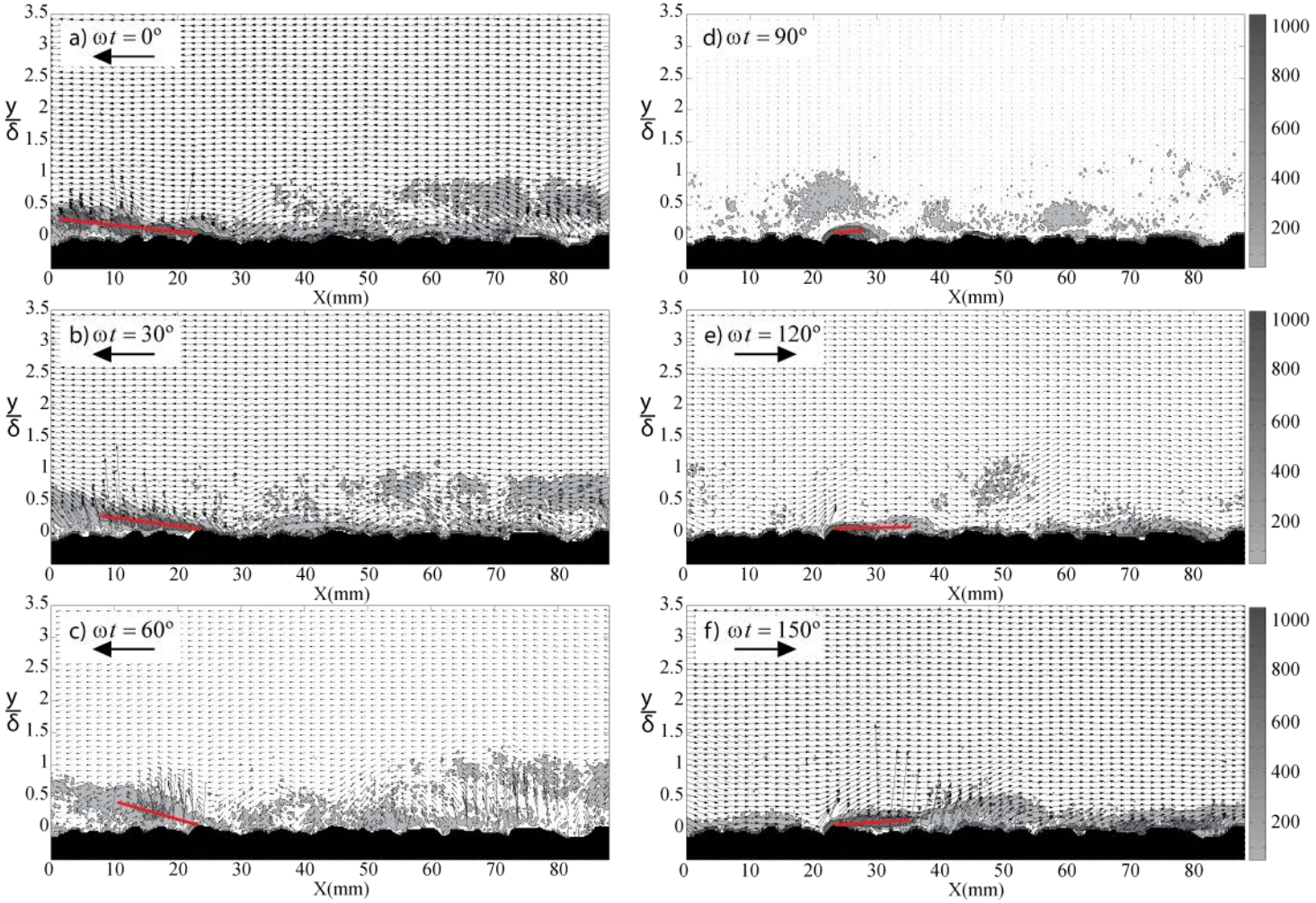

Figure 4.15. Time evolution of a shear layer formed in Test no. 10; roughness: $D_{50} = 7.0mm$; $Re_w = 1.27 \times 10^4$. Half cycle. Background variable: $T^2\lambda_{ci}^2$. Arrows represent the direction of the free stream flow (no arrow represents the free stream flow reversal).

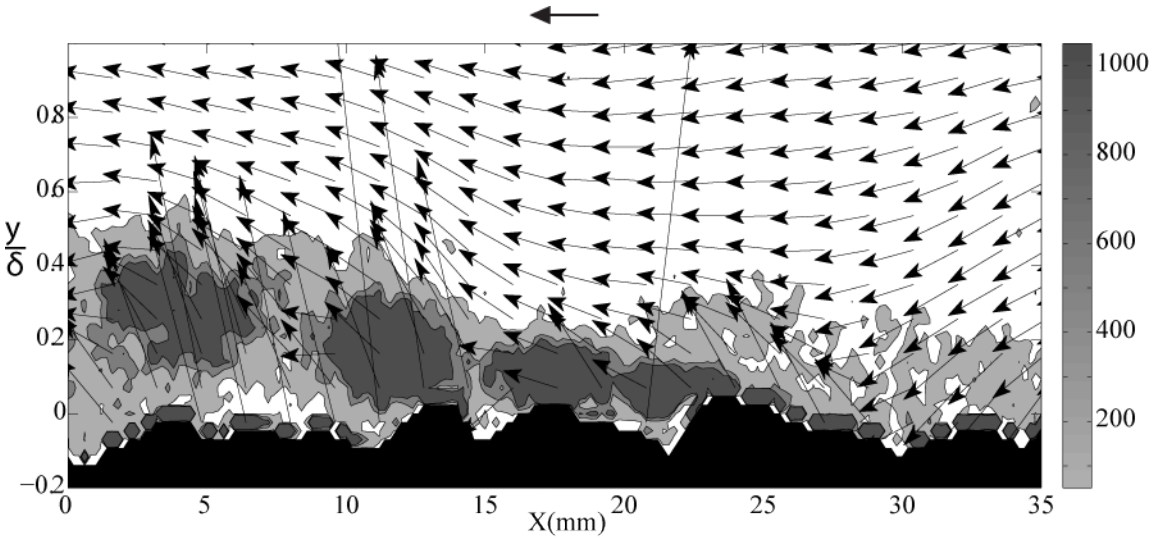

Figure 4.16. Close view of Figure 4.15 (a). Shear layer at $\omega t = 0$º. Background variable: $T^2\lambda_{ci}^2$. Test no. 10; roughness: $D_{50} = 7.0mm$; $Re_w = 1.27 \times 10^4$

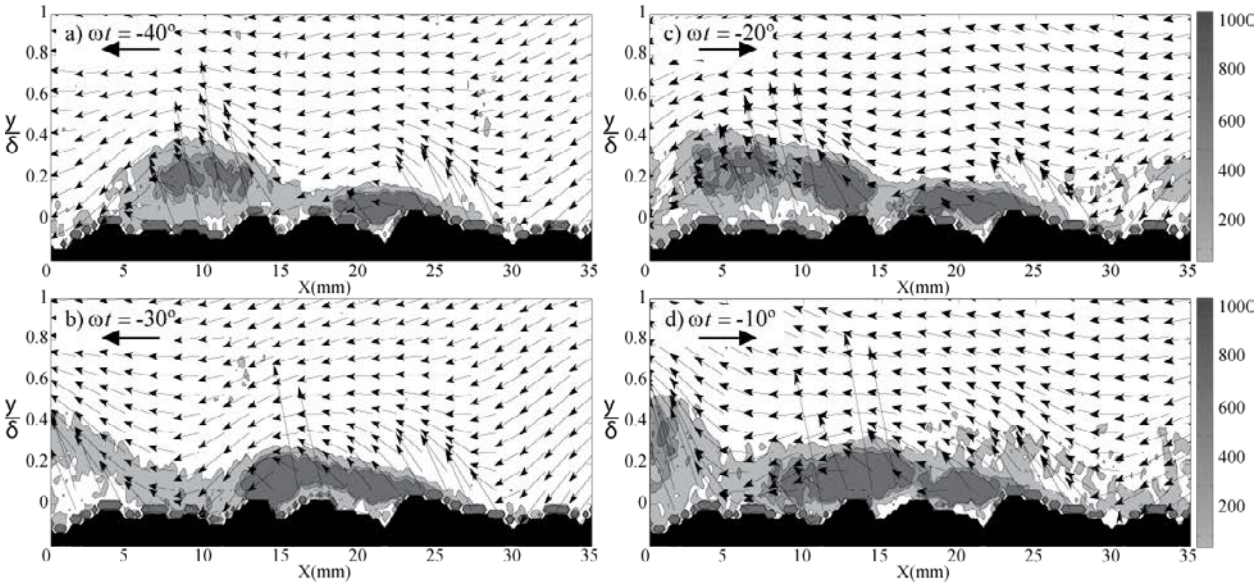

Figure 4.17. Close view at stages $\omega t < 0$º during the acceleration process. Background variable: $T^2\lambda_{ci}^2$. Test no. 10; roughness: $D_{50} = 7.0mm$; $Re_w = 1.27 \times 10^4$. Arrows represent the direction of the free stream flow (no arrow means zeros velocity of the free stream flow).

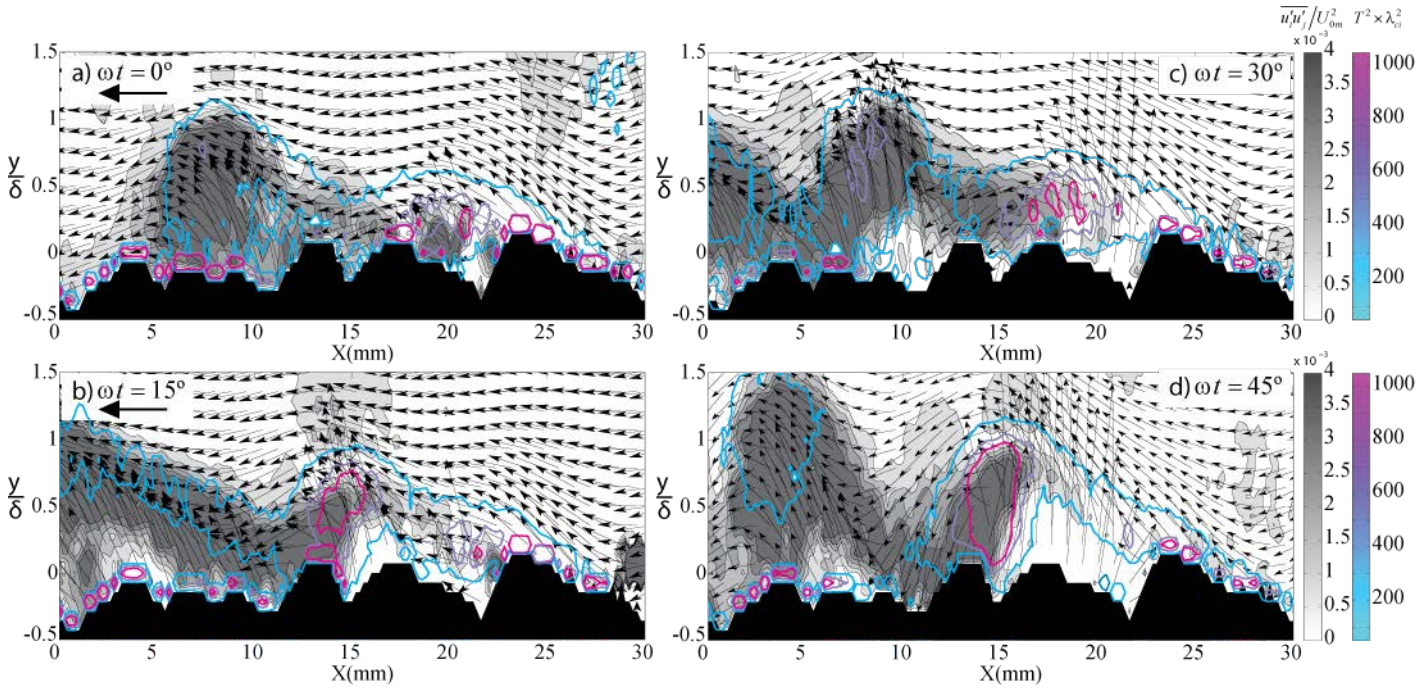

Figure 4.18. Close view of a shear layer during the deceleration stages. Background variable: $\frac{\overline{u_i'u_j'}}{U_{0m}^2}$; Contour variable: $T^2\lambda_{ci}^2$. Test no. 12; roughness: $D_{50} = 7.0mm$; $Re_w = 0.38 \times 10^4$. Arrows represent the direction of the free stream flow.

4.4 Proper Orthogonal Decomposition

Proper Orthogonal Decomposition (POD) is a technique used to capture the importance of scales in a flow Pope (2000). In the research presented herein POD will be used by means of defining the different scales present in fluctuating and instantaneous velocity fields.

When data available is from PIV, several studies (e.g. Kostas et al. (2005), Wu & Christensen (2010)) have concluded that snapshot POD technique was the most appropriate technique to study the energy contribution of each scale. The Snapshot POD technique outlined by Sirovich (1987) will be applied to rough wall fluctuating velocity fields in each phase having a maximum of 60 fields to complete the study. The basic idea behind the POD is to define a velocity field as a sum of an infinite series of uncorrelated time dependent coefficients, $a_n(t)$, times an orthogonal basis of spatial functions $\phi_n(x,y)$,

$$\vec{u}(x,y,t) = \sum_{n=1}^{\infty} a_n(t)\phi_n(x,y) \tag{4.7}$$

If the sum is truncated to a finite mode $\bar{n}$, then the POD technique minimizes the error between the real velocity field and the approximation,

$$\min \left\| \vec{u}(x,y,t) - \sum_{n=1}^{\bar{n}} a_n(t)\phi_n(x,y) \right\| \tag{4.8}$$

It turns out that both the uncorrelated time-dependent coefficients, $a_n(t)$, and the orthogonal eigenfunctions of each mode, $\phi_n(x,y)$, are related to the eigenvectors of the 2D-spatial autocorrelation matrix of the velocity $u(x,y,t)$, as detailed in Kostas et al. (2005).

The use of the POD allows a second type of analysis consisting on low and high-pass filter any instantaneous velocity field at a given mode $\hat{n}$. The result of the low-pass filter is directly obtained from the POD decomposition

$$\vec{u}_L(x,y,\omega t) = \sum_{n=1}^{\hat{n}} a_n(\omega t)\phi_n(x,y) \tag{4.9}$$

Whereas the high-pass filter velocity field can be computed as the residual from the original velocity field,

$$\vec{u}_H(x,y,\omega t) = \vec{u}(x,y,\omega t) - \vec{u}_L(x,y,\omega t) \tag{4.10}$$

The focus of study in this section are the experiments carried out over rough walls, thus POD decomposition will be performed above the maximum level of the grain crests.

4.4.1 Fluctuating Velocity Fields

When using the POD decomposition, the eigenvalues obtained from the analysis of the 2D spatial autocorrelation matrix are also a focus of the analysis. In particular, if the velocity used to obtain the POD is the fluctuating velocity fields ($u'(x,y,t)$)the eigenvalues represent the TKE contribution of each mode to the total TKE of the fluctuating system.

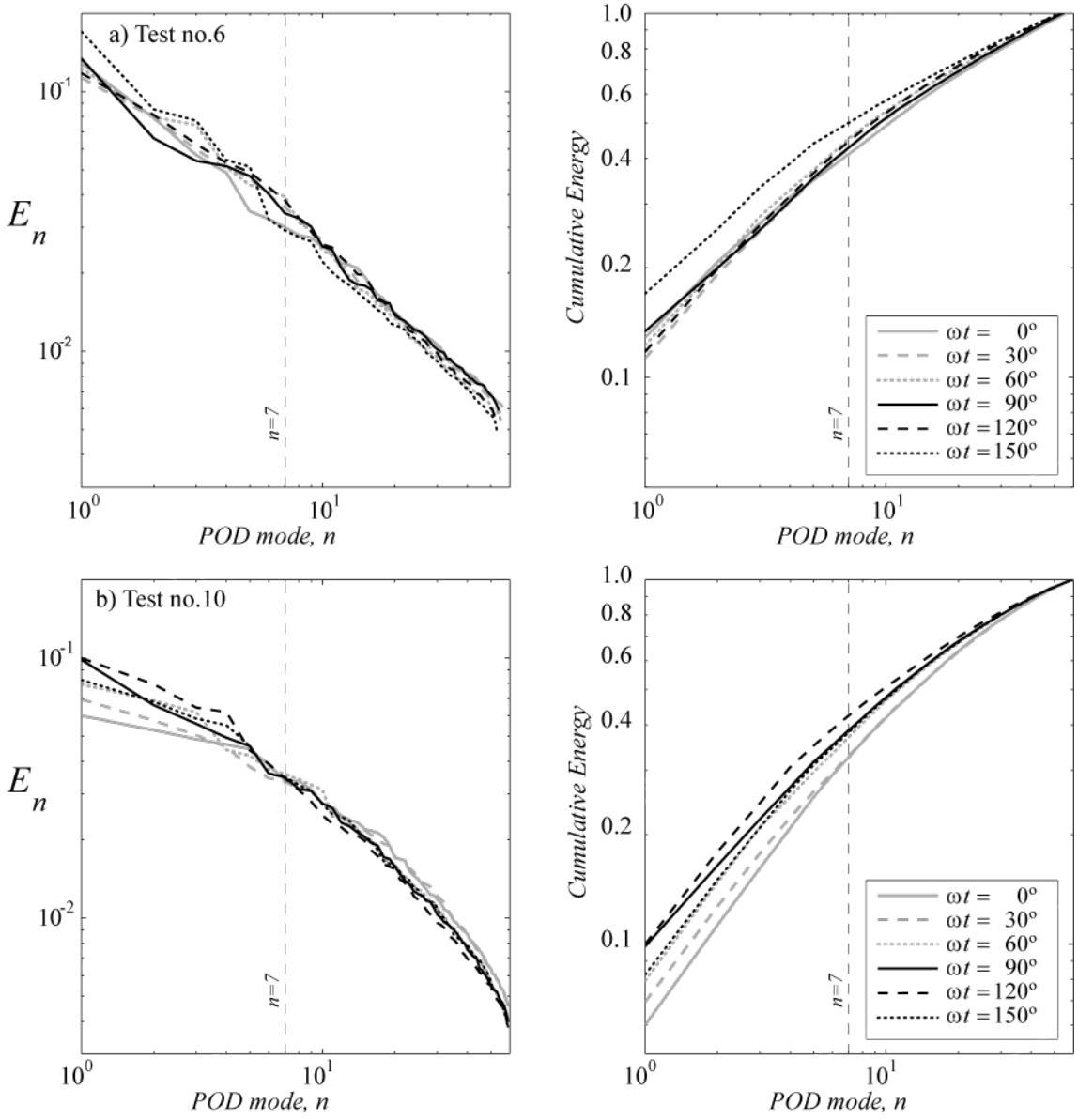

Figure 4.19. Proper Orthogonal Decomposition (POD) and energy distribution in different phases. (a) Test no. 6; roughness: $D_{50} = 1.5\ mm$; $Re_w = 1.27 \times 10^4$. (b) Test no. 10; roughness: $D_{50} = 7.0\ mm$; $Re_w = 1.27 \times 10^4$

Figure 4.19 shows the POD decomposition representing the TKE contained in each mode and the cumulative energy for two different tests –same flow conditions but different bed roughness- during a half cycle of Tests no. 6 and 10. Lower modes are representative of larger scales and vice versa. The scatter between phases is higher both in frictional energy content and cumulative energy in lower modes, expecially for the greater roughness scenario (Test no.10, Figure 4.19 b).Looking in detail at the energy distribution in Figure 4.19 (b) phases with higher free stream velocities contain less energy for lower modes; At higher modes energy is greater. This change in tendency is produced between $n>5$ and $n<9$ (Figure 4.19 b) and at $n=7$ in Test no. 10 (Figure 4.19 b). Thus lower free stream velocity phases have higher gradients in fractional energy content. This suggests that higher free stream velocity phases have a more uniform distribution of the energy contained in each mode.

The time evolution of the first 5 modes during a cycle is plotted in Figure 4.20. A trend for lower modes is found by fitting the function $A cos^2(\omega t + B) + C$, because it is a representation of the energy of a sinusoidal signal. The adjustment shown in Figure 4.21 is considered acceptable. The smoothing of the amplitude of modes oscillation for higher values is related to the A fitting coefficient. In this regard, Figure 4.22 shows the mode evolution of the fitted amplitude in Test no. 6 and Test no.10. Both curves show a clear lineal trend broken only in certain modes. For example, in Test no.6 this trend is broken from modes $n>5$ and $n>9$, which coincides with the modes where the energy of different phases cross over one to each other changing the tendency detailed above. Moreover in Test no.10 (Figure 4.22) has a break in the linear trend of the evolution of the fitting amplitude coefficient in the mode $n=7$, where, once more, all lines of energy contained in each mode for different phases coincide. Bearing in mind that the amplitude coefficient A is directly related to the standard deviation of the energy contained in a single mode during its time evolution, the location of the peak around $n=7$ indicates the singularity of this mode. Figure 4.23 shows the evolution of the C term plotted for different modes. As expected this term is related to the mean value of the energy contained in one mode along a complete cycle.

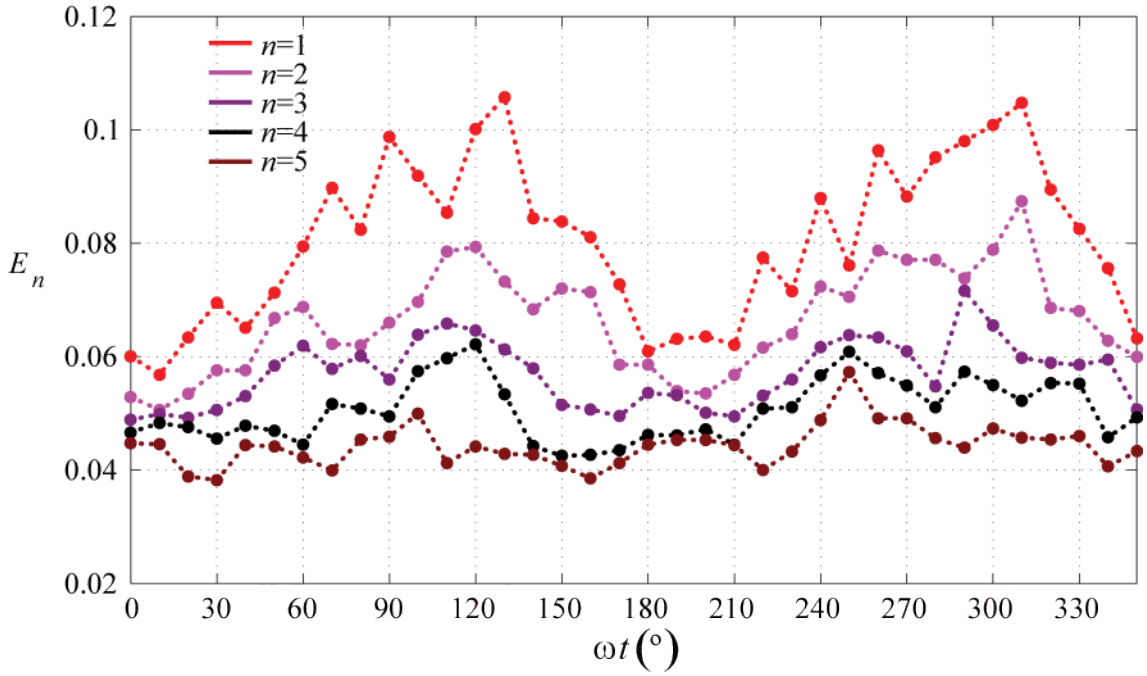

Figure 4.20. Time evolution of the first 5 POD modes during a cycle. Test no. 10; roughness: $D_{50} = 7.0\ mm$; $Re_w = 1.27 \times 10^4$

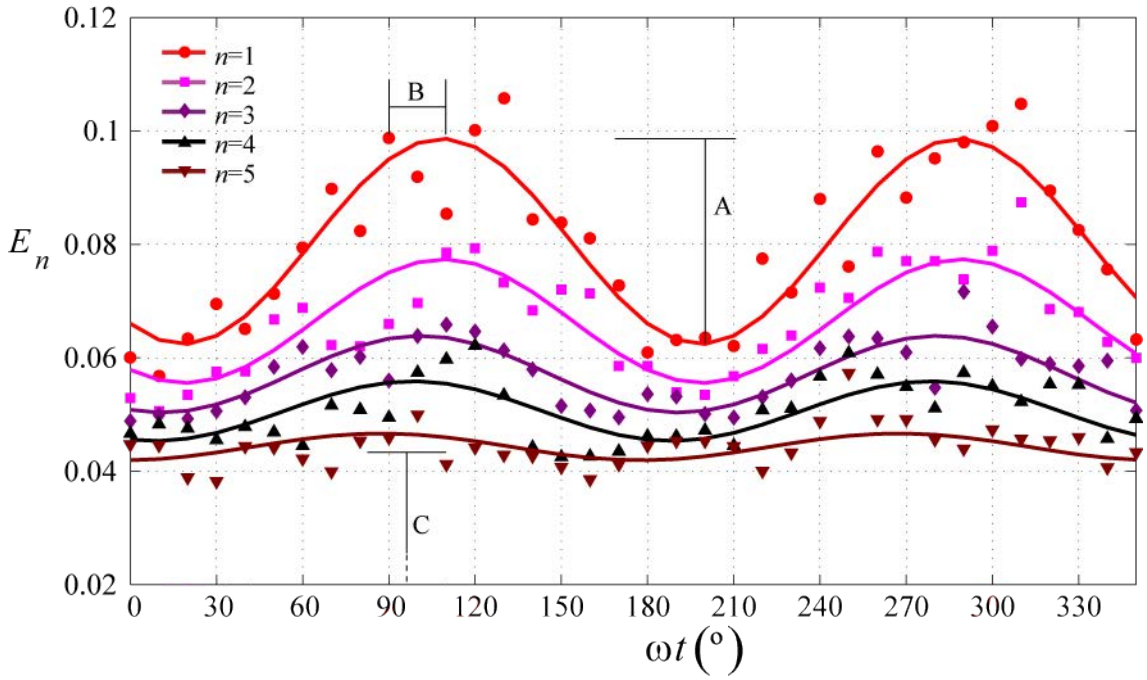

Figure 4.21. Fitted curves of the first 5 POD modes adjusted to the curve $A \cdot cos^2(\omega t + B) + C$. Test no. 10; roughness: $D_{50} = 7.0\ mm$; $Re_w = 1.27 \times 10^4$

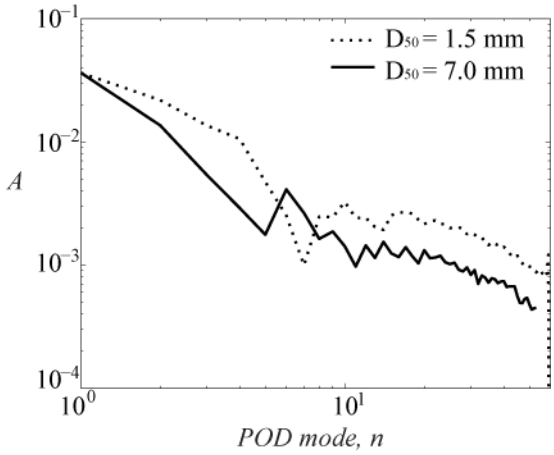

Figure 4.22. Modes distribution of the first fitting term, from the adjustment of Figure 4.21. . Dotted line: . Test no. 6; roughness: $D_{50} = 1.5\ mm$; $Re_w = 1.27 \times 10^4$. Dashed line: Test no. 10; roughness: $D_{50} = 7.0\ mm$; $Re_w = 1.27 \times 10^4$

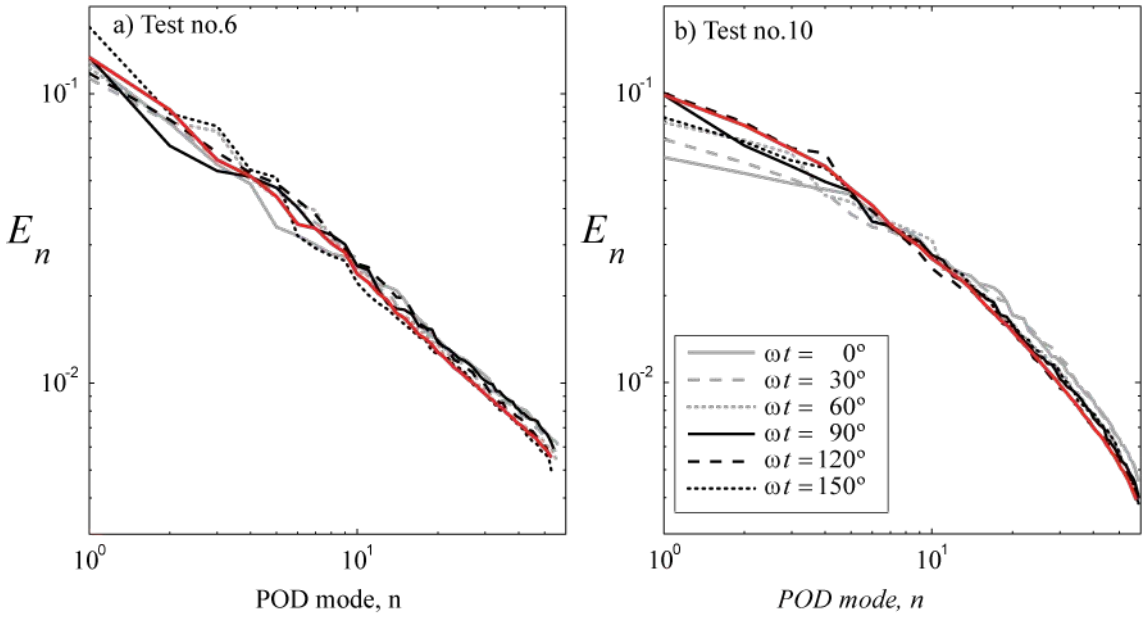

Figure 4.23. Red line: modes distribution of the term C from the adjustment of Figure 4.21.

The low- and high-pass filter will be applied to a fluctuating velocity field using $n = 7$ as the filtering mode. In order to link this with the coherent structures defined in previous sections two particular phases have been chosen with structures present in the phase averaged flow: i) the fluctuating velocity field of a snapshot where a vortex was present in the mean flow, $\omega t = 80º$ in Test no.6, and ii) a snapshot with a shear layer, $\omega t = 0º$ in Test no.10. The first case is shown in Figure 4.24 whereas the second in shown in Figure 4.25. Firstly it is worthwhile to recall that the velocity fields used in this analysis are the fluctuating velocities and so the structures defined in Section 4.3 are not going to be represented in any of the resulting filtered fields. In fact, the

analysis is directed towards the fluctuations present around the structures. In this regard, fluctuations are more represented in smaller scales whereas larger scales are more related to the motion of the structure. For instance, in Figure 4.24 (b), the vortex of the mean flow may be centered in the coordinates $X \cong 28\,mm,\ y/\delta \cong 0.5$, where larger scales –low-pass filtered image- indicate a positive vertical motion. Besides, in the case of the shear layer, Figure 4.25 (a) draws two fluctuating vortices centered at $X \cong 7\,mm,\ y/\delta \cong 0.3$ the first one and at $X \cong 14\,mm,\ y/\delta \cong 0.2$ the second one. Lower mode snapshots show how the first vortex is directed towards the wall whereas the second feature is at a positive vertical velocity. This is in agreement with the definition of the shear layer done in Section 4.3.2(iii), where this feature is described as a consequence of a first vortex being shed from a grain, impacting on the following grain (in the direction of the free stream velocity) and being rebounded from this second grain.

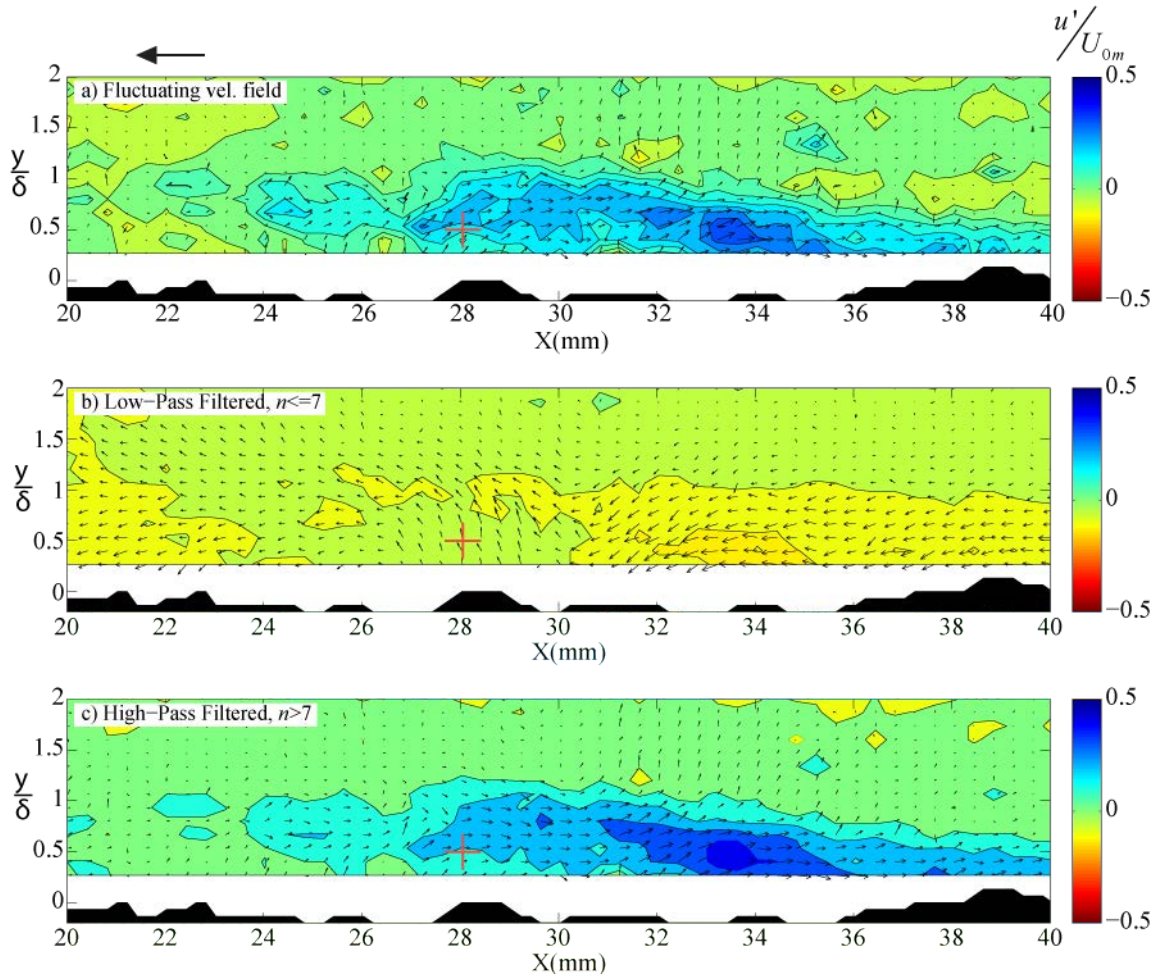

Figure 4.24. (a) Fluctuating velocity field of the close view of Figure 4.10 (a) at $\omega t = 80º$; Test no. 6; roughness: $D_{50} = 1.5\,mm$; $Re_w = 1.27 \times 10^4$. (b) Low-pass filter –large scales- of the representation shown in (a). (c)High-pass filtered (a) fluctuating velocity field, related to smaller scales. Background variable: non dimensional streamwise velocity fluctuations.

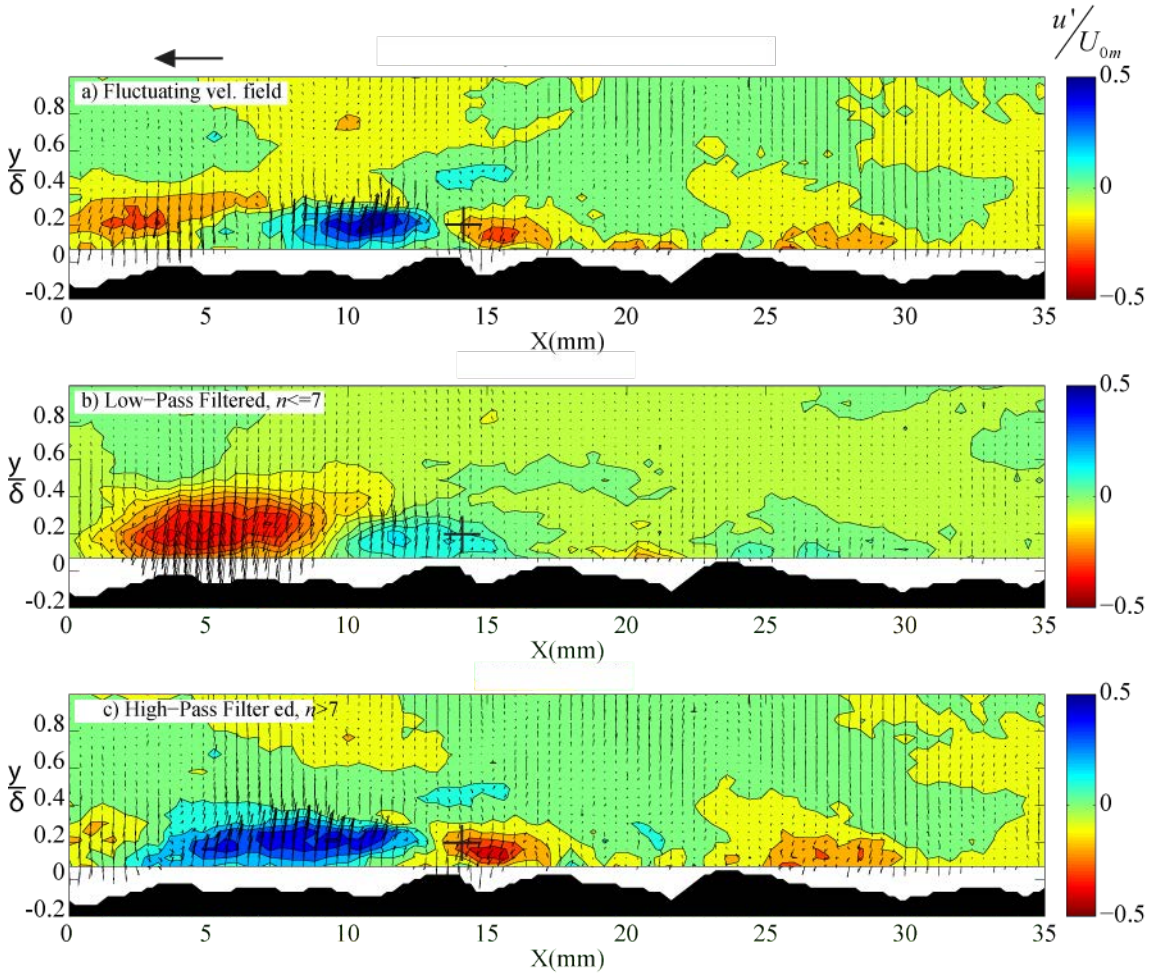

Figure 4.25. (a) Fluctuating velocity field of the close view of Figure 4.16 at $\omega t = 0^{o}$; Test no. 6; roughness: $D_{50} = 1.5\ mm$; $Re_w = 1.27 \times 10^4$. (b) Low-pass filter –large scales- of the representation shown in (a). (c)High-pass filtered (a) fluctuating velocity field, related to smaller scales. Background variable: non dimensional streamwise velocity fluctuations.

4.4.2 Instantaneous Velocity Fields

The use of instantaneous velocity fields is intended to introduce the structures described in section 4.3 to the POD analysis. Therefore, in this case, the eigenvalues of the 2D spatial autocorrelation matrix will not be the TKE of each particular mode. However, the low and high pass filters can be used by means of defining the role of larger and smaller scales. The use of fluctuating velocity fields disallows the analysis of the structures present in the mean flow.

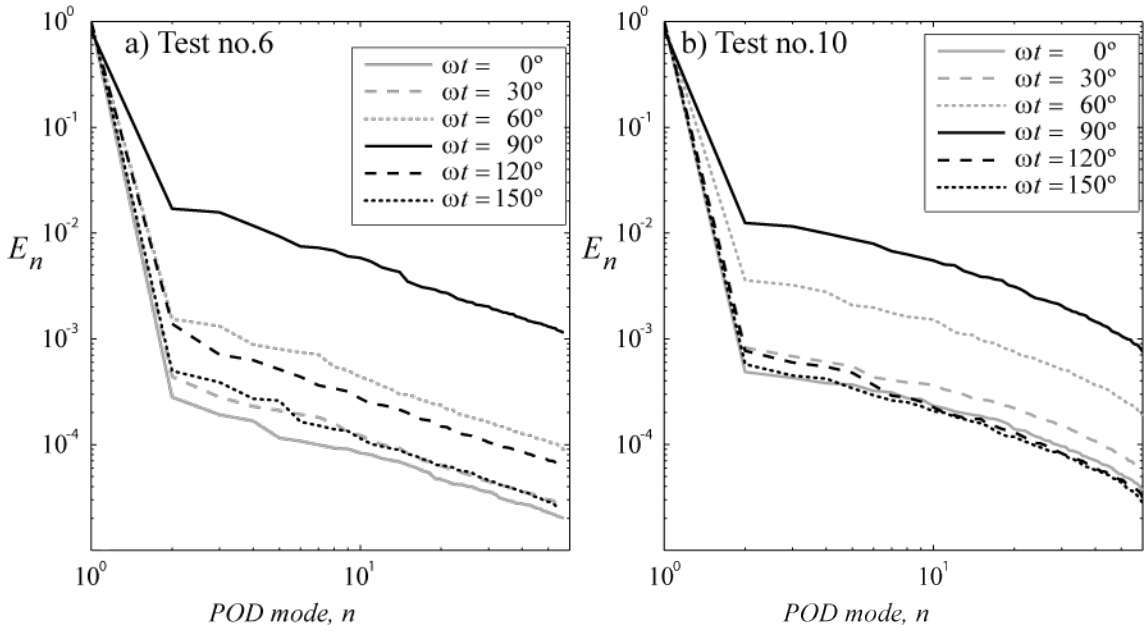

Figure 4.26. Proper Orthogonal Decomposition (POD) fields in different phases obtained using instantaneous velocity. (a) Test no. 6; roughness: $D_{50} = 1.5\ mm$; $Re_w = 1.27 \times 10^4$. (b) Test no. 10; roughness: $D_{50} = 7.0\ mm$; $Re_w = 1.27 \times 10^4$

The eigenvalues obtained from the same scenarios used in previous section are shown in Figure 4.26. In contrast to Figure 4.19 the first mode is clearly very different from higher modes having an eigenvalue more than two orders of magnitude greater than the second mode. Another main difference is seen in modes $n > 2$ where the eigenvalues obtained from the POD analysis using instantaneous velocity fields are also two orders of magnitude lower than the TKE contained in each mode in Figure 4.19. However, in this case the organization of the phases follows a trend similar to the evolution of the free stream velocity: eigenvalues are inversely proportional to the free stream velocity; they increase when free stream velocity is low and vice versa. This behavior in Figure 4.26 is due to the inclusion of part of the mean velocity field in the first mode. However, as higher modes have lower eigenvalues for instantaneous velocity fields, the first mode in this case also gets part of the energy contained in lower scales of the fluctuating field.

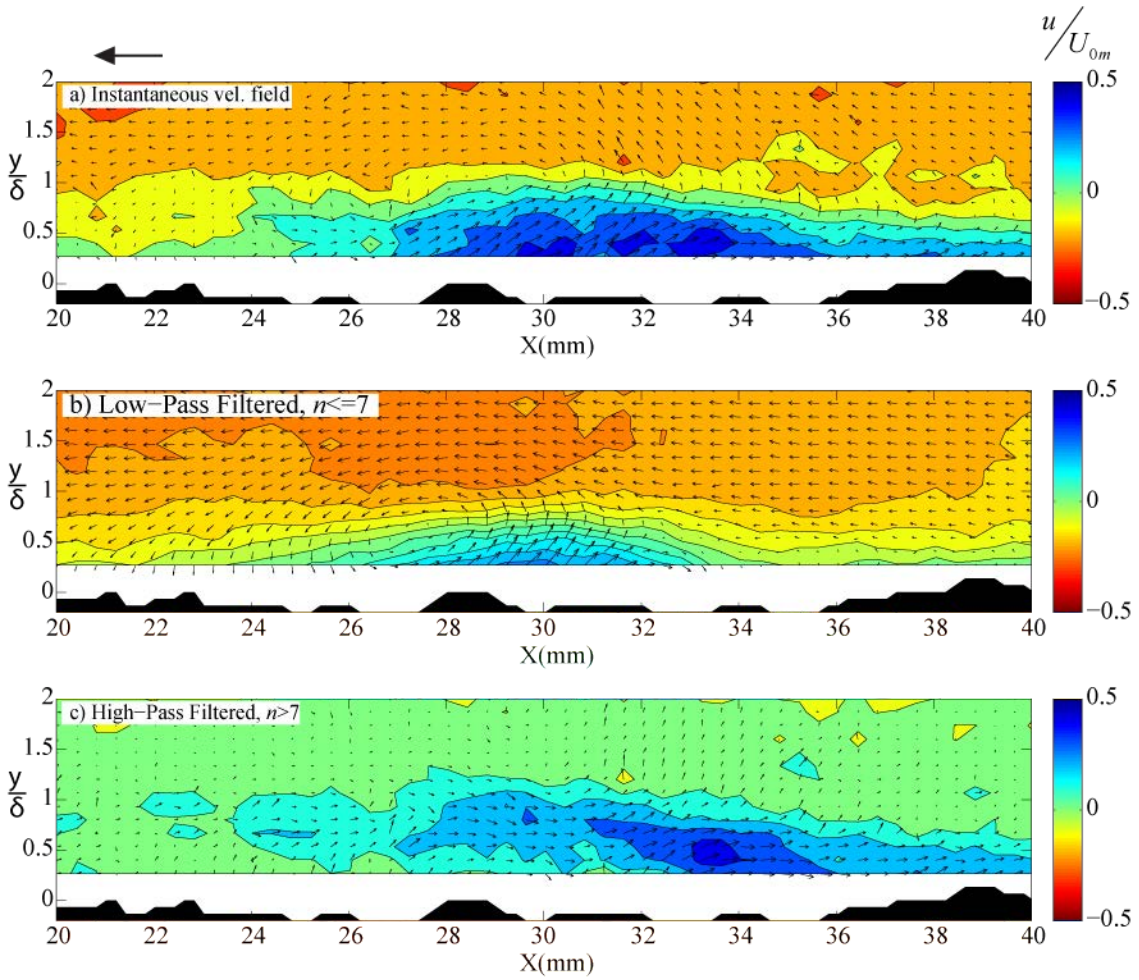

Figure 4.27. (a) Instantaneous velocity field of the close view of Figure 4.10 (a) at $\omega t = 80^{o}$; Test no. 6; roughness: $D_{50} = 1.5\ mm$; $Re_w = 1.27 \times 10^4$. (b) Low-pass filter –large scales- of the representation shown in (a). (c)High-pass filtered (a) fluctuating velocity field, related to smaller scales. Background variable: non dimensional streamwise instantaneous velocity.

Figure 4.27 plots the low- and high-pass filtered instantaneous velocity field which can be compared to Figure 4.24. As expected, lower modes -larger scales- contain the vortex detected in the mean flow. The residual velocity field (Figure 4.27 c) is not very different from the high-pass filtered image shown in Figure 4.24 (c). This is also the case of the shear layer shown in Figure 4.16 and Figure 4.25 when computing the POD using instantaneous velocity fields (Figure 4.28). In Figure 4.28 it is important to point out the differences in the background variable scale. This was done in order to see the behavior of the instantaneous flow in Figure 4.28 (a) and the mean flow in Figure 4.28 (b), but also to compare Figure 4.28 (c) with Figure 4.25 (c). In the case of the POD analysis with instantaneous velocity fields, the low-pass filtered image is representative of the mean flow because the first mode contains part of the structure defined in the phase averaged snapshots. However, it is interesting to see how, in both cases,

high-pass filtered snapshots do not differ one from the other regardless of the energy/eigenvalue distribution. Figure 4.29 (a) shows the first mode of the POD decomposition of the instantaneous velocity field from Test no.6 ($\omega t = 80º$), where the vortex detected in the phase averaged flow field can be identified as well. The second mode, plotted in Figure 4.29 (b) can be compared to the first mode obtained from the POD analysis of the fluctuating velocity field of the same snapshot, shown in Figure 4.30. Few differences are seen from one figure to the other meaning that the instantaneous analysis captures the second mode as the first mode of the fluctuating analysis.

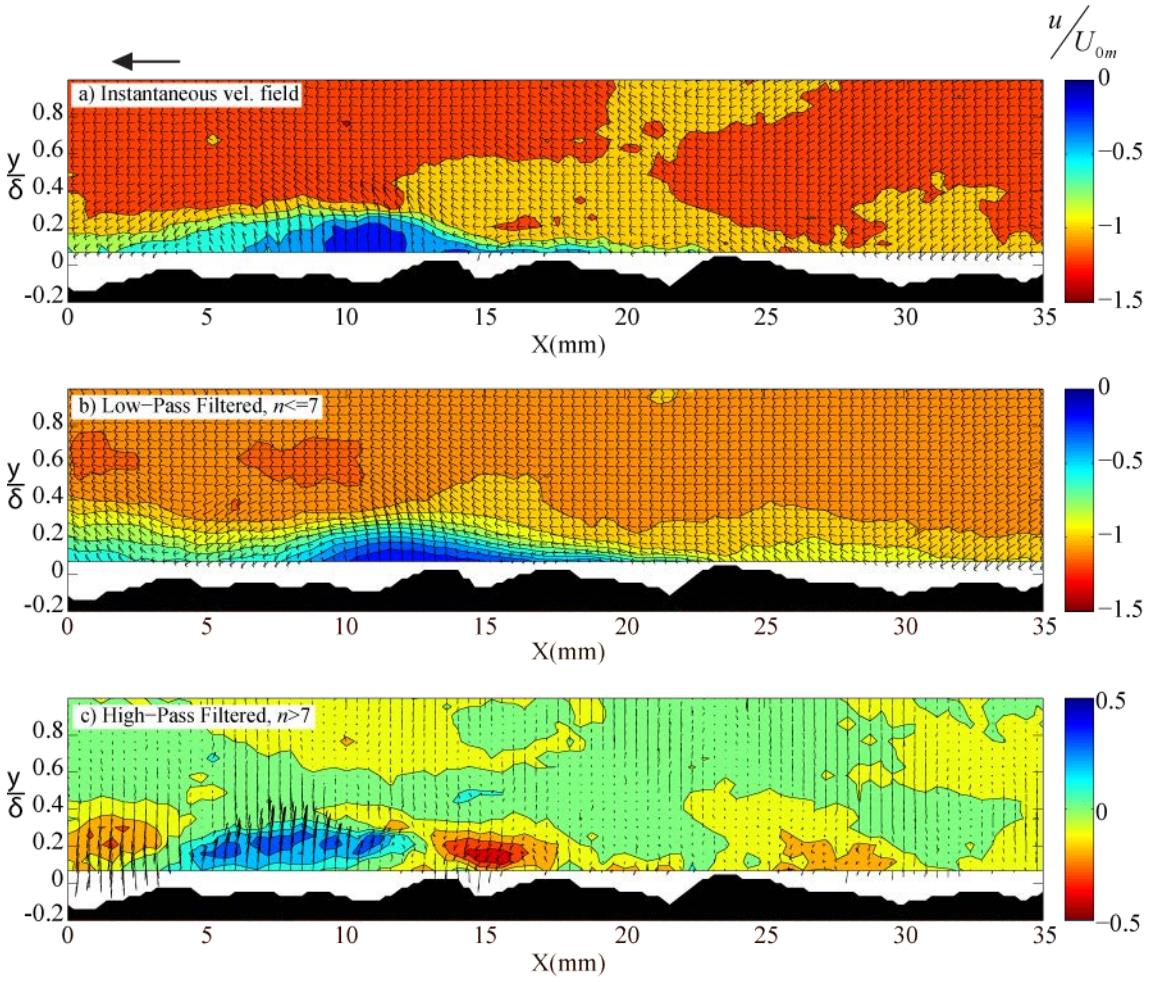

Figure 4.28. (a) Instantaneous velocity field of the close view of Figure 4.16 at $\omega t = 0º$; Test no. 6; roughness: $D_{50} = 1.5\ mm$; $Re_w = 1.27 \times 10^4$. (b) Low-pass filter –large scales- of the representation shown in (a). (c)High-pass filtered (a) fluctuating velocity field, related to smaller scales. Background variable: non dimensional streamwise instantaneous velocity.

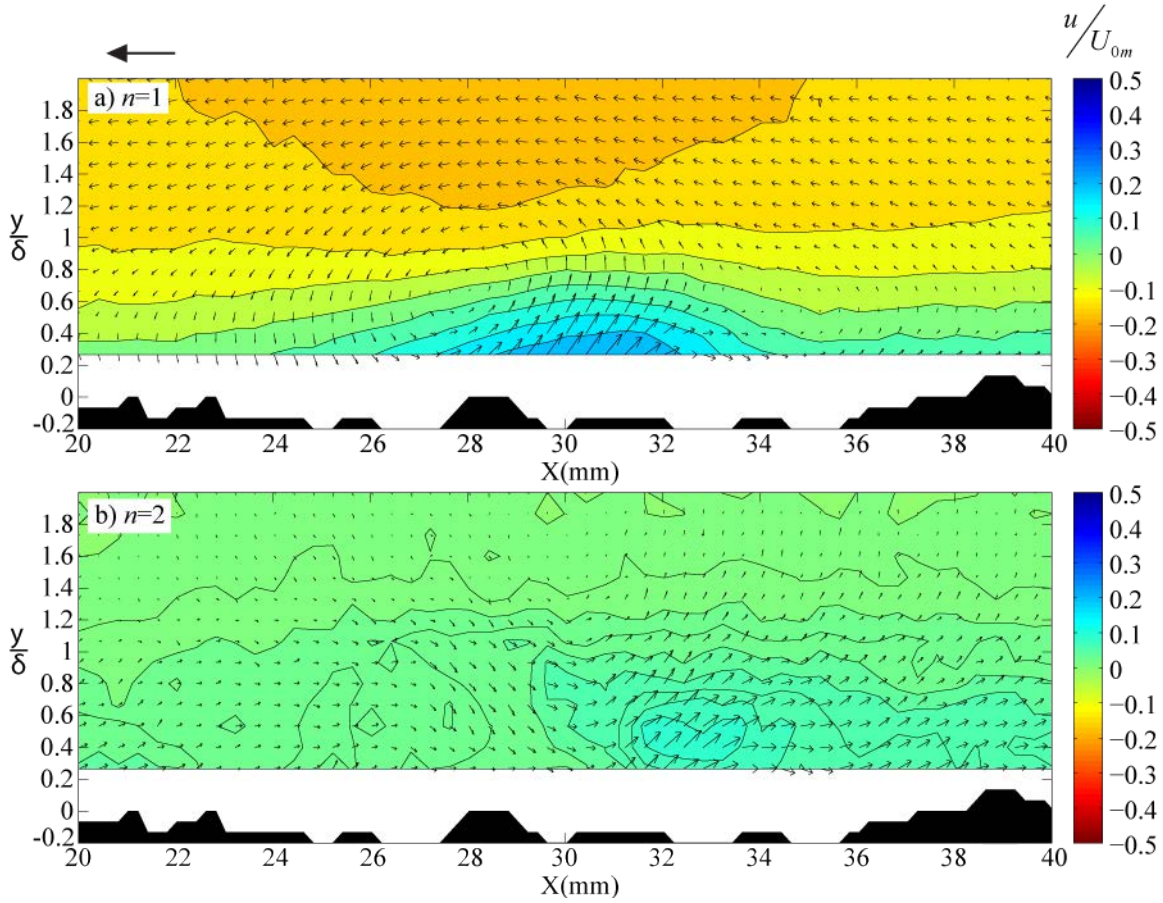

Figure 4.29. Snapshots of the (a) first mode and (b) the second mode obtained when applying the POD technique to the instantaneous velocity field from Figure 4.10 (a) at $\omega t = 80^{o}$. The instantaneous velocity field is shown in Figure 4.27 (a). Test no. 6; roughness: $D_{50} = 1.5\ mm$; $Re_w = 1.27 \times 10^4$. Background variable: non dimensional streamwise instantaneous velocity.

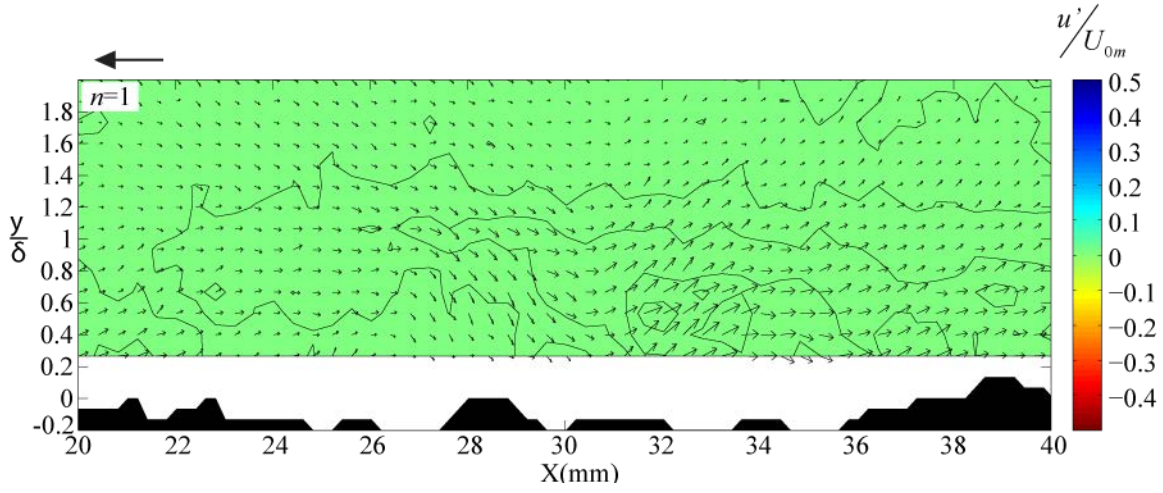

Figure 4.30. Snapshot of the first mode obtained when POD is computed using fluctuating velocity fields from Figure 4.10 (a) at $\omega t = 80^{o}$. The fluctuating velocity field is shown in Figure 4.24 (a). Test no. 6; roughness: $D_{50} = 1.5\ mm$; $Re_w = 1.27 \times 10^4$. Background variable: non dimensional streamwise velocity fluctuations.

4.5 Summary

This chapter extended the knowledge on oscillatory boundary layers in the laminar-to-turbulent regime presented in Chapter 3. The spatial analysis carried out with the PIV results turned out to define different coherent structures present in the oscillatory flow experiments.

In smooth wall scenarios, structures present were compared to vortex tubes described previously by Carstensen et al. (2010). The Kelvin-Helmholtz instability was found to be the best explanation for the inception of these structures.

Tests performed over rough-walls showed the existence of two different structures: i) isolated vortices and ii) turbulent bursts both formed during the wall flow reversal close to the wall. The former shed from the wall and lost the vortex-shape after reaching a certain height. The latter were initially formed as smaller vortices but lost their shape before detaching. They reached lower heights before disappearing. Bursts were considered local small vortices that appeared as a signature without shape in the mean flow. However vortices were formed in all cycles and thus arose with the clear form on the phase averaged snapshots.

POD decomposition was used to analyze the structures already described. A comparison between POD performed over fluctuating velocity fields and instantaneous velocity field yielded to the conclusion that only the latter option was describing better the structures whereas the POD on fluctuating velocity fields gave the energy contained in each mode.

Chapter 5: Conclusions

Conclusions from the vortex ring experiments, Chapter 2, and oscillatory boundary layers in flows in the laminar-to-turbulent transition regime, Chapter 3 and Chapter 4, are included in this chapter. Final remarks and outlines of the future work close the chapter

5.1 Vortex Ring Impinging Permable Boundaries

The experiments reported in Chapter 2 analyzed the interaction of vortex rings with different permeable boundaries. Vortex rings impinging a solid boundary were also studied in order to compare the main characteristics of their motion towards the boundary with the permeable cases.

The foams used had a finite thickness of 2.5mm except the coarsest case, K79, 5mm thick, but no influence on *h* was found in the experiments, showing that the results presented herein can be extended to thicker permeable boundaries.

Results obtained using PIV showed how permeability affects the characteristics already found for vortex rings moving towards a solid boundary. Permeable boundaries changed:

a) The diameter stretching: as permeability increases, the diameter of the primary ring presents smaller increments.

b) The primary ring deceleration: vortex ring notices the existence of the boundary when permeability of the boundary decreases.

c) The secondary vortex ring formation: higher permeable boundaries presented a less coherent secondary ring with shorter life. This affected the negative stretching and the rebound of the primary ring.

The first and second point (a and b) are linked by the stretching effect: vortex decelerates while the diameter increases. The moment at which this effect starts depends on the permeability of the boundary. In a solid boundary, the stretching starts when ring is located at a height equivalent to the initial diameter of the ring, showing that the fluid area influenced by the flow of ring is similar to that of the Hill's spherical vortex.

The analysis of velocities close to the boundary revealed a high influence on the height chosen to assume velocities were representing the interface flux. The closest approach to the interface was 1mm due to the characteristics of the foam and was sufficient to analyse the vertical velocities but clearly influenced the viscous effects. Therefore the analysis of the no-slip/slip boundary condition at the interface became more complicated. Moreover when secondary vorticity was computed other errors regarding the choice of the interface level ($\tilde{Y} = 0$) revealed to be important as well.

However, regardless of these two factors, an evolution from a no-slip boundary condition when the vortex ring is impinging a solid boundary and a slip boundary condition for permeable boundaries was detected by the analysis of the primary vorticity.

In general, four of the five cases showed vortex ring evolution over the permeable/solid boundary, except for the coarsest foam, K79, where the ring penetrated the foam. However the motion of the entire ring across the interface did not maintain the structure of the ring.

The analysis of the foam inside the ring was carried out using Darcy's equation to model the flux inside the foam. Although the coarsest case was not applicable the whole time of the interaction it helped on studying the influence of the thickness of the foams used.

Finally the research presented in Chapter 2 has shown that further investigation is needed for the interactions of vortex rings with permeable boundaries. For instance, azimuthal variations of the vortex ring characteristics were omitted from the analysis presented so far. Moreover, additional experiments are needed using different Reynolds numbers to see its influence on permeable boundaries.

5.2 PIV Experiments in Oscillatory Boundary Layers

The experimental analysis of the oscillatory boundary layers using PIV implied a main advantage over other measuring techniques: the obtained velocity field of a 2D area which yielded to the possibility of measuring a large number of profiles along the streamwise direction at the same time.

In order to define the flow regime, the Kamphuis (1975) diagram as shown in Figure 3.7, was found to be the best approach to characterize different flow regimes. Regardless of the flow regime, boundary-layer thickness reached its maximum value at a phase prior to the flow reversal. Smooth-wall experiments show a boundary-layer thickness as a function of the period of oscillation, although some of the experiments were in the laminar to turbulent transition regime. However, in the rough-wall experiments, considered in the laminar to turbulent regime, the boundary-layer thickness depends firstly on the ratio A/k_s and, for the same value, secondly on the wave Reynolds number.

Friction factor in the smooth-wall results was properly defined using the theoretical equation proposed by Batchelor (1967). The Pedocchi & Garcia (2009) empirical friction coefficient predictor was found to be appropriate for experiments in the laminar-to-turbulent transition regime, though some of the experiments were outside the initial range proposed by

these authors. Finally, the Kamphuis (1975) diagram, Figure 3.5, was used to obtain a friction factor for experiments in the rough turbulent regime, which did not differ substantially from the friction factor obtained using Pedocchi & Garcia (2009) formula for flows in transition. This is likely due to some experiments residing in-between the rough turbulent and laminar-to-turbulent transition regimes. Thus, when no experimental values are available, the friction factor can be either obtained from Kamphuis (1975), in Figure 3.5, or from the Pedocchi & Garcia (2009) empirical formula.

Log laws proposed for the turbulent regime did not fit for flows in the laminar to turbulent transition regime, and more research is needed in this direction. Thus, the friction velocity was obtained indirectly from the computation of bottom shear stress.

Bottom shear stress was defined using two different equations: the addition of Reynolds stresses and viscous stresses–Eq.(3.11)–and the integral of momentum equation in the y direction–Eq.(3.12). Results show how the phase lead between friction velocity and the free-stream velocity (Sleath, 1987; Jensen et al., 1989) is better defined when the integral of momentum equation is used. The observed differences in maximum friction velocity and phase lag between the friction and free-stream velocities is highly sensitive to the zero level definition. In terms of absolute value, both in rough and smooth-wall experiments, friction velocities obtained using the two equations gave higher results when bottom shear stresses were computed using the integral of momentum equation, mainly due to the underestimation of turbulence values close to the wall.

From Figure 3.13, smooth-wall experiments (although considered in the laminar regime) exhibit local turbulence close to the wall that is damped for $y > 0.75\delta$. The turbulence is more constantly distributed when roughness is present and no damping phenomenon is observed with increasing wall-normal position.

In general terms, the existing and well-established formulations for predicting the boundary layer thickness, the friction factor and the friction velocity for flows in transition work well based on the results presented herein. Important discrepancies were detected for the phase shift, and experimental values are more reliable when the integral of momentum equation is used.

5.3 Coherent Structures in Oscillatory Boundary Layers

The main goal of the research presented in Chapter 4 was to study the formation and evolution of coherent structures present in oscillatory flows over smooth and rough walls. For the first time, PIV has been used as the experimental technique towards the definition of present signatures. Experimental studies focusing on structures present in oscillatory flows have used point-wise measurement techniques, such as hot wire anemometry -Sleath (1987), Jensen et al. (1989), Akhavan et al. (1991a), Carstensen et al. (2010), Carstensen et al. (2012)-, toghether with dye flow visualizations -Carstensen et al. (2010), Carstensen et al. (2012)- and Particle Tracking Velocimetry -Krstic & Fernando (2001)-. Other studies used numerical simulations in attempts to reproduce some of the experimental results in the rough wall case, and to see the triggering effect of coherent structures in smooth wall oscillatory flows –i.e. Akhavan et al. (1991a), Blondeaux & Vittori (1994), Vittori & Verzicco (1998), Costamagna et al. (2003), Pedocchi et al. (2011)-.

Features present in oscillatory flows over smooth wall were confirmed to be vortex tubes –defined within the limitations of 2D PIV. Similar to the experimental work of Carstensen et al. (2010), features detected in the experiments within the laminar to turbulent transition regime were formed by the Kelvin-Helmholtz instability during the wall flow reversal. As outlined in Chapter 3, the flow reversal close to the wall takes place in previous stages compared to the free stream velocity. Therefore, there exists a gradient in vertical velocity profiles, shown in the shear stresses profiles in which very low values of turbulent stresses were detected to trigger the Kelvin-Helmholtz instability. Vortex tubes appear during the wall flow reversal and increase in size through the cycle while decelerating due to two effects: the kinetic energy dissipation and the stretching effect. During the second half cycle, where another wall flow reversal occurs, vortices present from the previous half cycle merge and migrate upwards while new structures are formed near the wall. The vertical separation point between both signatures is at the maximum streamwise velocity height –where shear stresses have a singular point-. Vortex tubes are the signatures introducing turbulence to the system as shown in the vertical TKE profiles.

In rough wall oscillatory flows, the definition of coherent structures became more complicated mainly due to the singular points added by the roughness itself. Analysis was done by using phase averaging thus structures detected in the mean flow were also present in most of the instantaneous velocity fields. Although the roughness was designed to be uniform, structures were commonly shed from the same points. This is likely due to the transitional flow regime studied herein (laminar to turbulent) in which particular ‘features’ become important. Discrete

shedding points may also have resulted from structures forming during phases of very low free stream velocity. Recalling that the definition of the flow regime (laminar/turbulent) in oscillatory flows assumes that most of the phases are within one regime, features formed in rough wall flows shed during the laminar stages of the cycle . It is in this situation where anomalies in the roughness turn out to trigger signatures in the same position.

Three different coherent structures were identified in the rough wall scenarios. The first one, was named vortex because in its early stages of formation, it had the shape of a vortex. Vortices appeared during the wall flow reversal and where shed from the wall. Beyond this point their shape as a vortex disappeared and turned into a burst. Bursts coming from vortices created at the wall maintained a certain height particularly in the smaller rough scenarios. There was a coincidence on the trajectory of vortices according to the roughness diameter (k_s) and the amplitude of oscillation (A), indicating that these two variables are controlling the motion of the vortices. Therefore, vortices were created at the latter stages of the deceleration phases and ejected from the wall during early acceleration stages. Vortices disappeared before the next decelerating cycle began lasting at most a quarter of a cycle including the stages in which they lost their vortex appearance and became bursts.

The second feature defined was linked to vortices, but was named turbulent spots. This feature consisted of smaller vortices created close together in different instantaneous fields that appeared as a burst in the phase averaged snapshots. Bursts were also shed from the wall but did not extend into the flow as far as the vortices did before dissipating. However, their life cycle was equivalent to that of the shed vortices.

Finally a third coherent structure was observed. It was considered a shear layer for his shape during the maximum free stream velocity stages. Shear layers were only detected in scenarios with $A/k_s < 15$ and where linked to vortices described as the first structure. Thus, shear layers were formed right at the time when vortices detached from the wall. Initially they were considered laminar structures covering a single grain. However as free and wall streamwise velocity increased, this boundary layer detached from the grain At this point small vortices were formed, and the shear layer became a chain of a vortices formed at a grain, colliding in the next crest and being detached right after. This was clearer at maximum free stream velocity phases. During decelerating stages, small vortices did not rebound on the following crests and shear layer finally became a large vortex during the wall flow reversal.

In order to study the influence of the spatial scales on the structures, the snapshot POD technique was used. Typically the POD decomposition is performed using the fluctuating fields such that the eigenvalues of the 2D spatial autocorrelation function represent the contribution of each mode to the total TKE energy. However, if this POD results are used to low- and high-pass filter the fluctuating velocity fields, no information is extracted from the resulting velocity fields because structures present in the mean flow are not included in the analysis. If the POD is computed back again using the instantaneous velocity fields, mean flow appears as the first and most energetic mode (more than 2 orders of magnitude greater). Thus, the velocity field from the first mode represents the mean flow structure. If a band-pass filter is applied from the second mode to a chosen mode –e.g. $n = 7$- the fields obtained with the instantaneous POD decomposition are very similar to the fields obtained by low-pass filtering the fluctuating POD decomposition -$n \leq 7$-. High-pass filtered velocity fields in both cases resulted in similar snapshots as well.

Vortices and shear layers are explained with the largest scale present in the flow (the lower mode $n = 1$). Both POD fluctuating analysis and POD instantaneous analysis show how the largest scales of the fluctuations define the motion of each structure. Finally smaller scales –higher modes- were responsible of bursts formation since they were triggering the smaller vortices located at similar places; they were also the scales were fluctuations were kept.

5.4 Final remarks and future work

The work presented in this thesis has helped the author to learn mainly about fluid mechanics but especially about the PIV technique. It has also given some new inputs to particular problems in fluid mechanics such as vortex rings and oscillatory boundary layers.

The experience gathered through all the years of this research allows the author to have a special view about the PIV technique, used in many other experimental fields.

The advantages of the method have been clearly highlighted along this entire document. However, PIV carries with it several variables that can affect the final results shown in any study. For example, the setup and the optimization of the lenses used to transform the laser light into a light sheet (which does not have a constant thickness) or the particularities of the software used to process the photos. Another peculiarity is that the method is an ensemble average of the motion of the particles present inside the interrogation area. Thus the precision of the final results is a function of this interrogation size and not the magnification factor. Moreover, when a 2D PIV is used, mass continuity is not satisfied unless the phenomenon is clearly 2D (i.e. in the

smooth wall oscillatory flow, no wall effects should be present). However a small error should always be assumed due to the 3D motions of the particles inside the light sheet, the variable thickness of this light sheet and the accumulation of small errors when the post process of the image is carried out (i.e. substitution of bad peaks during the interrogation process, smoothing of the final results or interpolations performed to have a vector every pixel). This latter was found particularly interesting either for the author and the tutor of the thesis to be considered in further analysis.

The first work to perform is to implement a PIV system at the Laboratori de Morfodinàmica Fluvial of the GITS group at the UPC to study sediment resuspension dynamics in estuaries combined with a PTV system to follow the motion of the sediment grains.

At following, several issues related to specific future work are presented in correlation with former sections:

5.4.1 Vortex Rings Impinging Permeable Boundaries

To study the influence of the pore diameter on the vortex ring evolution, it would be interesting to use boundaries with the same permeability but different pore diameter, and vice versa. Therefore the effects of both variables could be decoupled.

Azimuthal instabilities were detected in previous experiments using planar recording systems parallel to 2D recording of vertical-radial planes. The effect of permeability on these instabilities should also help to understand how far the influence of the bed is. Therefore some zenithal recordings using tin-chloride precipitation should be carried out to study qualitatively such effect of permeability.

In another direction, in order to see how the permeability is affecting resuspension, it would be interesting to modify the experimental setup adding a small layer of sediment above the permeable boundary. This would also be helpful to further investigate the slip boundary condition. In this direction, a larger amount of experiments carried out with higher resolution would be useful to compute the radial velocity profiles close to the wall and their changes with permeability.

5.4.2 Oscillatory Boundary Layers

There are several issues to target as future work in this topic. Firstly the definition of the shear stresses should also take into account that 2D PIV results may not satisfy mass continuity close to the wall and therefore other terms in the Navier-Stokes equation should not be neglected.

Secondly, experiments described in Chapter 3 and Chapter 4 were defined as flows in the laminar-to-turbulent transition regime were no log-law is defined. Therefore a wider range of experiments with Reynolds numbers in the same region would allow to define a log-law similar to the one already described for turbulent flows. Also PIV experiments in turbulent oscillatory boundary layers should also help on defining some other coherent structures that may form in turbulent flows.

Thirdly, with the results already presented in this thesis, observations on the coherent structures evolution may be further detailed by studying its dynamics.

Finally 3D PIV experiments should be performed to further study the characteristics of coherent structures present close to the wall.

Obviously other sediment bed layer grain sizes should also be included to future work on oscillatory boundary layers over rough walls. In the research presented herein, only two ratios of A/k_s were studied and more experiments widening this range may be helpful to describe flows in transition and coherent structures present in them.

References

Adhikari, D. & Lim, T. (2009), 'The impact of a vortex ring on a porous screen', *Fluid Dynamics Research* **41**(5), 051404.

Adrian, R. (1991), 'Particle-imaging techniques for experimental fluid mechanics', *Annual review of fluid mechanics* **23**(1), 261–304.

Adrian, R. (1999), 'Dynamic ranges of velocity and spatial resolution of particle image velocimetry', *Measurement Science and Technology* **8**(12), 1393.

Adrian, R. (2005), 'Twenty years of particle image velocimetry', *Experiments in Fluids* **39**(2), 159–169.

Adrian, R., Christensen, K. & Liu, Z. (2000), 'Analysis and interpretation of instantaneous turbulent velocity fields', *Experiments in Fluids* **29**(3), 275–290.

Akhavan, R., Kamm, R. & Shapiro, A. (1991*a*), 'An investigation of transition to turbulence in bounded oscillatory stokes flows. Part 1: Experiments', *Journal of Fluid Mechanics* **225**(1), 395–422.

Akhavan, R., Kamm, R. & Shapiro, A. (1991*b*), 'An investigation of transition to turbulence in bounded oscillatory stokes flows. Part 2: Numerical simulations', *J. Fluid Mech* **225**, 423–444.

Batchelor, G. (1967), *An introduction to fluid dynamics*, Cambridge Univ Pr.

Beavers, G. & Joseph, D. (1967), 'Boundary conditions at a naturally permeable wall', *J. Fluid Mech* **30**(1), 197–207.

Bethke, N. (2008), Vortex Ring Interaction with a Particle Layer: Implications for Sediment Transport, PhD thesis, University of Cambridge.

Bethke, N. & Dalziel, S. (2012), 'Resuspension onset and crater erosion by a vortex ring interacting with a particle layer', *Physics of Fluids* **24**, 063301.

Blondeaux, P., Scandura, P. & Vittori, G. (2004), 'Coherent structures in an oscillatory separated flow: numerical experiments', *Journal of Fluid Mechanics* **518**, 215–229.

Blondeaux, P. & Vittori, G. (1994), 'Wall imperfections as a triggering mechanism for stokes-layer transition', *Journal of Fluid Mechanics* **264**, 107–136.

Bonn, D., Rodts, S., Groenink, M., Rafa, S., Shahidzadeh-Bonn, N. & Coussot, P. (2008), 'Some applications of magnetic resonance imaging in fluid mechanics: complex flows and complex fluids', *Ännu. Rev. Fluid Mech.* **40**, 209–233.

Carstensen, S., Sumer, B. & Fredsøe, J. (2010), 'Coherent structures in wave boundary layers. Part 1. oscillatory motion', *Journal of Fluid Mechanics* **646**(1), 169–206.

Carstensen, S., Sumer, B. & Fredsøe, J. (2012), 'A note on turbulent spots over a rough bed in wave boundary layers', *Physics of Fluids* **24**(11), 115104–115104.

Cerra, A. W., J. & Smith, C. (1983), 'Experimental observations of vortex ring interaction with the fluid adjacent to a surface', *Interim Report Lehigh Univ., Bethlehem, PA. Dept. of Mechanical Engineering and Mechanics.* **1**.

Chilton, T. & Colburn, A. (1931), 'Pressure drop in packed tubes', *Industrial & Engineering Chemistry* **23**(8), 913–919.

Costamagna, P., Vittori, G. & Blondeaux, P. (2003), 'Coherent structures in oscillatory boundary layers', *Journal of Fluid Mechanics* **474**, 1–33.

Dalziel, S. B. (2006), *DigiFlow User Manual*. http://www.damtp.cam.ac.uk/lab/digiflow/.

De Rooij, F., Dalziel, S. & Linden, P. (1999), 'Electrical measurement of sediment layer thickness under suspension flows', *Experiments in fluids* **26**(5), 470–474.

Fornarelli, F. & Vittori, G. (2009), 'Oscillatory boundary layer close to a rough wall', *European Journal of Mechanics-B/Fluids* **28**(2), 283–295.

Garcia, M., Musalem, R. & Admiraal, D. (2004), Exploratory study of oscillatory flow over a movable sediment bed with particle-image-velocimetry (piv), ASCE.

Hill, M. (1894), 'On a spherical vortex.', *Proceedings of the Royal Society of London* **55**(331-335), 219–224.

Hino, M., Nakayama, A., Kashiwayanagi, M. & Hara, T. (1983), 'Experiments on the turbulence statistics and the structure of a reciprocating oscillatory flow', *Journal of Fluid Mechanics* **131**, 363–400.

Hrynuk, J., Van Luipen, J. & Bohl, D. (2012), 'Flow visualization of a vortex ring interaction with porous surfaces', *Physics of Fluids* **24**, 037103.

Jensen, B., Sumer, B. & Fredsoe, J. (1989), 'Turbulent oscillatory boundary layers at high reynolds numbers', *Journal of Fluid Mechanics* **206**(1), 265–297.

Jonsson, I. (1980), 'A new approach to oscillatory rough turbulent boundary layers', *Ocean Engineering* **7**(1), 109–152.

Kamphuis, J. (1975), 'Friction factor under oscillatory waves', *Journal of the Waterways Harbors and Coastal Engineering Division* **101**(2), 135–144.

Keiller, D. & Sleath, J. (1976), 'Velocity measurements close to a rough plate oscillating in its own plane', *Journal of Fluid Mechanics* **73**(04), 673–691.

Kelvin, L. (1867), 'The translatory velocity of a circular vortex ring', *Phil. Mag.* **33**, 511–512.

Kostas, J., Soria, J. & Chong, M. (2005), 'A comparison between snapshot pod analysis of piv velocity and vorticity data', *Experiments in fluids* **38**(2), 146–160.

Krstic, R. & Fernando, H. (2001), 'The nature of rough-wall oscillatory boundary layers', *Journal of Hydraulic Research* **39**(6), 655–666.

Lamb, H. (1993), 'Hydrodynamics', *Hydrodynamics, by Horace Lamb and Foreword by Russ Caflisch, pp. 764. ISBN 0521458684. Cambridge, UK: Cambridge University Press, November 1993.* **1**.

Li, H. (1954), Stability of oscillatory laminar flow along a wall, Technical report, Beach Erosion Board. Corps of Engineers.

Lim, T., Nickels, T. & Chong, M. (1991), 'A note on the cause of rebound in the head-on collision of a vortex ring with a wall', *Experiments in fluids* **12**(1), 41–48.

Masuda, N., Yoshida, J., Ito, B., Furuya, T. & Sano, O. (2012), 'Collision of a vortex ring on granular material. Part 1. Interaction of the vortex ring with the granular layer', *Fluid Dynamics Research* **44**(1), 015501.

Maxworthy, T. (1977), 'Some experimental studies of vortex rings', *Journal of Fluid Mechanics* **81**(03), 465–495.

Mazzuoli, M., Vittori, G. & Blondeaux, P. (2011), 'Turbulent spots in oscillatory boundary layers', *Journal of Fluid Mechanics* **685**, 365.

Munro, R., Bethke, N. & Dalziel, S. (2009), 'Sediment resuspension and erosion by vortex rings', *Physics of Fluids* **21**, 046601.

Munro, R. & Dalziel, S. (2005), 'Attenuation technique for measuring sediment displacement levels', *Experiments in fluids* **39**(3), 602–613.

Munro, R., Dalziel, S. & Jehan, H. (2004), 'A pattern matching technique for measuring sediment displacement levels', *Experiments in fluids* **37**(3), 399–408.

Naaktgeboren, C., Krueger, P. & Lage, J. (2012), 'Interaction of a laminar vortex ring with a thin permeable screen', *Journal of Fluid Mechanics* **1**(1), 1–27.

Newman, S., Brown, R., Perry, J., Lewis, S., Orchard, M. & Modha, A. (2001), 'Comparative numerical and experimental investigations of the vortex ring phenomenon in rotorcraft', *American Helicopter Society International* .

Norbury, J. (1973), 'A family of steady vortex rings', *Journal of Fluid Mechanics* **57**(03), 417–431.

Orlandi, P. & Verzicco, R. (1993), 'Vortex rings impinging on walls: axisymmetric and three-dimensional simulations', *Journal of Fluid Mechanics* **256**, 615–615.

Pedocchi, F., Cantero, M. & Garcia, M. (2011), 'Turbulent kinetic energy balance of an oscillatory boundary layer in the transition to the fully turbulent regime', *Journal of Turbulence* (12).

Pedocchi, F. & Garcia, M. (2009), 'Friction coefficient for oscillatory flow: the rough–smooth turbulent transition', *Journal of Hydraulic Research* **47**(4), 438–444.

Pope, S. (2000), *Turbulent flows*, Cambridge Univ Pr.

Prasad, A. (2000), 'Particle image velocimetry', *Current science* **79**(1), 51–60.

Richardson, S. (1971), 'A model for the boundary condition of a porous material. Part 2', *J. Fluid Mech* **49**(2), 327–336.

Saffman, P. (1979), 'The approach of a vortex pair to a plane surface in inviscid fluid', *Journal of Fluid Mechanics* **92**(3), 497–503.

Sirovich, L. (1987), 'Turbulence and the dynamics of coherent structures. Part1. coherent structures', *Quarterly of Applied Mathematics* **45**, 561.

Sleath, J. (1987), 'Turbulent oscillatory flow over rough beds', *Journal of Fluid Mechanics* **182**(369-409).

Staymates, M. & Settles, G. (2005), 'Vortex ring impingement and particle suspension', *Bulletin of the American Physical Society* .

Stewart, W. (1951), 'Helicopter behaviour in the vortex-ring conditions', *Aeronautical Research Committee, R&M* (3117).

Sumer, B.M., J. B. F. J. (1987), 'Turbulence in oscillatory boundary layers', *Advances in Turbulence (e. Gt. Comte-Bellot & J. Mathieu)* pp. 556–567.

Swearingen, J., Crouch, J. & Handler, R. (1995), 'Dynamics and stability of a vortex ring impacting a solid boundary', *Journal of Fluid Mechanics* **297**, 1–28.

Tanaka, H. & Samad, M. (2006), 'Prediction of instantaneous bottom shear stress for smooth turbulent bottom boundary layers under irregular waves', *Journal of Hydraulic Research* **44**(1), 94–106.

Tavoularis, S. (2005), *Measurement in fluid mechanics*, Cambridge Univ Pr.

Taylor, G. (1971), 'A model for the boundary condition of a porous material. Part 1', *Journal of Fluid Mechanics* **49**(02), 319–326.

Vittori, G. & Verzicco, R. (1998), 'Direct simulation of transition in an oscillatory boundary layer', *Journal of Fluid Mechanics* **371**, 207–232.

Walker, J., Smith, C., Cerra, A. & Doligalski, T. (1987), 'The impact of a vortex ring on a wall', *Journal of Fluid Mechanics* **181**(1), 99–140.

Westerweel, J. (1993), 'Digital particle image velocimetry: theory and application'.

Widnall, S., Bliss, D. & Tsai, C. (1974), 'The instability of short waves on a vortex ring', *Journal of Fluid Mechanics* **66**(1), 35–47.

Wu, Y. & Christensen, K. (2010), 'Spatial structure of a turbulent boundary layer with irregular surface roughness', *Journal of Fluid Mechanics* **655**, 380–418.

Zeng, Z. & Grigg, R. (2006), 'A criterion for non-darcy flow in porous media', *Transport in Porous Media* **63**(1), 57–69.

Zhou, J., Adrian, R., Balachandar, S. & Kendall, T. (1999), 'Mechanisms for generating coherent packets of hairpin vortices in channel flow', *Journal of Fluid Mechanics* **387**(1), 353–396.